January 2022

Application-Dependent Wavelength Selection For Hyperspectral Imaging Technologies

John Chauvin

Recommended Citation

Chauvin, John, "Application-Dependent Wavelength Selection For Hyperspectral Imaging Technologies" (2022). *Theses and Dissertations*. 4331.
https://commons.und.edu/theses/4331

APPLICATION-DEPENDENT WAVELENGTH SELECTION FOR HYPERSPECTRAL IMAGING TECHNOLOGIES

by

John Carville Chauvin
Bachelor of Science, Physics, Rhodes College, 1996
Master of Science, Physics, Naval Postgraduate School, 2003
Master of Engineering Management, Old Dominion University, 2009
Master of Science in Engineering, Electrical Engineering, Arizona State University, 2014

A Dissertation
Submitted to the Graduate Faculty

of the

University of North Dakota

in partial fulfillment of the requirements

for the degree of

Doctor of Philosophy

Grand Forks, North Dakota

August
2022

This dissertation, submitted by John Chauvin in partial fulfillment of the requirements for the degree of Doctor of Philosophy from the University of North Dakota, has been read by the Faculty Advisory Committee under whom the work has been done and is hereby approved.

Kouhyar Tavakolian, Chairperson

Fartash Vasefi, Committee Member

Bo Liang, Committee Member

Hossein Salehfar, Committee Member

Joseph Vacek, Member at Large

This dissertation is being submitted by the appointed advisory committee as having met all of the requirements of the School of Graduate Studies at the University of North Dakota and is hereby approved.

Chris Nelson
Dean of the School of Graduate Studies

26 July 2022
Date

PERMISSION

Title	Application-Dependent Wavelength Selection for Hyperspectral Imaging Technologies
Department	Electrical Engineering
Degree	Doctor of Philosophy

In presenting this dissertation in partial fulfillment of the requirements for a graduate degree from the University of North Dakota, I agree that the library of this University shall make it freely available for inspection. I further agree that permission for extensive copying for scholarly purposes may be granted by the professor who supervised my dissertation work or, in his absence, by the Chairperson of the department or the dean of the School of Graduate Studies. It is understood that any copying or publication or other use of this dissertation or part thereof for financial gain shall not be allowed without my written permission. It is also understood that due recognition shall be given to me and to the University of North Dakota in any scholarly use which may be made of any material in my dissertation.

John Chauvin
5 August 2002

ACKNOWLEDGEMENTS

I wish to express my sincere appreciation to my advisor, Kouhyar Tavakolian, and my committee members Fartash Vasefi, Bo Liang, Hossein Salehfar, and Joseph Vacek. I would also like to thank Alireza Akhbardeh and Greg Bearman who have been instrumental in shaping the methodology and content of this dissertation research.

This achievement would not have been possible without the love and support of my wife, Amy Komatsuzaki, and my parents, Jane and Elmore Chauvin.

ABSTRACT

Hyperspectral imaging has proven to provide benefits in numerous application domains, including agriculture, biomedicine, remote sensing, and food quality management. Unlike standard color imagery composed of these broad wavelength bands, hyperspectral images are collected over numerous (possibly hundreds) of narrow wavelength bands, thereby offering vastly more information content than standard imagery. It is this higher information content which enables improved performance in complex classification and regression tasks. However, this successful technology is not without its disadvantages which include high cost, slow data capture, high data storage requirements, and computational complexity. This research seeks to overcome these disadvantages through the development of algorithms and methods to enable the benefits of hyperspectral imaging in inexpensive portable devices that collect spectral data at only a handful (i.e., 5-7) of wavelengths specifically selected for the application of interest.

This dissertation focuses on two applications of practical interest: fish fillet species classification for the prevention of food fraud and tissue oxygenation estimation for wound monitoring. Genetic algorithm, self-organizing map, and simulated annealing approaches for wavelength selection are investigated for the first application, combined with common machine learning classifiers for species classification. The simulated annealing approach for wavelength selection is carried over to the wound monitoring application and is combined with the Extended Modified Lambert-Beer law, a tissue oxygenation method that has proven to be robust to differences in melanin concentrations. Analyses for this second application included spectral convolutions to represent data collection with the envisioned inexpensive portable devices.

Results of this research showed that high species classification accuracy (> 90%) and low tissue oxygenation error (< 1%) is achievable with just 5-7 selected wavelengths. Furthermore, the proposed wavelength selection and estimation algorithms for the wound monitoring application were found to be robust to variations in the peak wavelength and relatively wide bandwidths of the types of LEDs that may be featured in the designs of such devices.

TABLE OF CONTENTS

TABLE OF FIGURES

LIST OF ACRONYMS

AOTF	Acousto-Optic Tunable Filter
BMU	Best Matching Unit
CDC	Center for Disease Control
COHb	Carboxyhemoglobin
CV	Cross Validation
EMLB	Extended Modified Lambert-Beer Law
FWHM	Full Width Half Maximum
GNB	Gaussian Naïve Bayes
GPS	Generalized Pattern Search
GPU	Graphics Processor Unit
Hb	Deoxyhemoglobin
HbO2	Oxyhemoglobin
HSI	Hyperspectral Imaging
KNN	K-Nearest Neighbors
LCTF	Liquid Crystal Tunable Filter
LD	Linear Discriminator
MCML	Monte Carlo for Multilayered Tissues
MLP	Multilayer Perceptron
MSE	Mean Squared Error
NIR	Near Infrared
NMRSE	Normalized Root Mean Squared Error
PCA	Principle Component Analysis
ReLU	Rectified Linear Unit
SO_2	Tissue Oxygenation
SOM	Self-Organizing Map
SVM	Support Vector Machine
SWIR	Short-Wave Infrared
UV	Ultraviolet
VNIR	Visible Near-Infrared
WKNN	Weighted K-Nearest Neighbors
WPD	Weight Plane Difference

CHAPTER I: INTRODUCTION

1.1 BACKGROUND

1.1.1 Food Safety and Quality Control

Hyperspectral imaging has in recent years become an invaluable tool for food safety and quality applications. Spoilage and contamination of food and food products are concerns that have been addressed by researchers over the past few years. Studies include detection of spoilage due to *E. coli* bacteria in grass carp fish [1], fecal contamination in apples [2], and bacterial contamination in chicken fillets [3]. Food fraud, the intentional mislabeling of food types or misrepresentation of production methods, is another major food safety issue that has been addressed with hyperspectral imaging. For example, this technology has been used to identify less expensive species of fish fillets that have been marketed and sold as more expensive red snapper fillets [4], [5].

Likewise, hyperspectral imaging has been a staple of agriculture monitoring for many years. Early applications include large-scale remote monitoring of land and agriculture from the Landsat-I satellite [6], monitoring of crop yield, and detection of plant disease and invasive species [7]. While agriculture applications have remained constant since these early examples, the methods have changed with unmanned aerial vehicle (UAVs) becoming an attractive survey platform for local, detailed monitoring efforts [8].

1.1.2 Diabetic Wound Monitoring

The global prevalence of diabetes among adults was estimated to be 9.5% (537 million people) in 2021 and is expected to rise to 10.2% (578 million people) by 2030 and up to 10.9% (700 million people) by 2045 [9], [10]. Of the people diagnosed with diabetes, around 15-25% will develop foot ulcers during their lifetime [11]. These foot ulcers are produced from neuropathy which leads to the formation of a callus which, as a result of frequent trauma, causes subcutaneous hemorrhage and eventual erosion to an ulcer [12]. In the United States, cost estimates for the management of diabetic foot ulcers are \$9–\$13 billion [10], [13]. In Nigeria and India, the cost of managing diabetic foot ulcers approaches 4% of the health budget for these countries [14].

Underrepresented communities are particularly at risk. Diabetic diagnosis and its subsequent complications are more prevalent in these underserved populations. African American adults are 60% more likely than non-Hispanic white adults to have been diagnosed with diabetes by a physician and twice as likely as non-Hispanic whites to die from diabetes [15]. According to the Center for Disease Control (CDC), the prevalence of diagnosed diabetes is highest among Native Americans and Alaskan Natives than among any other US racial group [16]. Compounding this, these communities also experience the healthcare difficulties of rural and low-access settings. More than 46 million Americans (15% of the US population) live in rural areas (CDC), and this cohort experiences a 17% higher rate of Type 2 Diabetes than urban residents while simultaneously suffering workforce shortages of primary and specialty care providers [17], [18].

The state of wound progression or healing is in large part influenced by the transport of oxygen to the affected area [19]. Tissue oxygenation (SO_2), the percentage of oxygenated hemoglobin in the blood, is thus a key indicator of tissue health and a vital metric for monitoring diabetic foot wounds. Hyperspectral imaging (HSI) offers a non-contact, non-invasive method for estimating SO_2 in tissue near the affected area, making it an ideal tool for diabetic foot wound monitoring [20]. Algorithms based on the Lambert-Beer law [21], Kubelka-Munk theory [22], and approximations to the Radiative Transfer Equation (RTE) [23] have been developed to estimate SO_2 from hyperspectral information, and many of these algorithms have found their way into clinical devices such as the OxyVu system (Hypermed, MA), the Kent Camera (Kent Imaging, Canada), and the TIVITA system (Diaspective, Germany) [24]. However, some researchers have noted disparities in SO_2 estimation accuracies for different skin types, with higher errors seen for patients with higher melanin concentration (i.e., darker skin) [25]–[27]. This presents a significant problem for monitoring wound progression in the most affected populations.

1.2 HYPERSPECTRAL IMAGING DISADVANTAGES

Most hyperspectral imagers are complicated. They fall into one of two major categories, based on the method by which the full spatial-spectral data cube is assembled. Data cubes can be reconstructed by either spatial scanning or spectral scanning or combination of these methods.

With spatial scanning imagers, light is collected at a point or along a line and dispersed into its spectral components by a dispersive optic such as prism or diffraction grating. This point or line is then scanned, either through physical motion of the sensor, reflection from a scanning mirror, or moving an object along a path.

With spectral scanning imagers, the full spatial content is collected by the image sensor. Collection of the wavelength bands is typically accomplished by switching wavelengths through filter wheels, electronically controlled liquid crystal tunable filters (LCTF) or acousto-optic tunable filters (AOTF) [28].

Despite successes in a range of food safety, agriculture, and biomedical applications, hyperspectral imaging does have its share of disadvantages, mostly due to the data cube being constructed from individual components collected in a time sequential manner. This can be an error-prone process, especially for high-speed imaging applications. Another category of hyperspectral imager, the snapshot imager, overcomes these issues by combining an array of optics to collect both the spatial and the spectral information simultaneously. Usually this means some compromise in either the spectral or spatial domain. All these solutions tend to be both complex and costly [29]. The reason they are costly is they are not designed for targeted applications. In research and discovery, you don’t know what wavelengths will be significant and what wavelength ranges in the spectral data are redundant. In many cases, once you understand the spectral characteristics for a particular targeted application, the complexity of the spectral imaging system can be significantly reduced.

An issue common to all hyperspectral imager types is the significant computing power required and the large file sizes of the data cubes, especially in applications involving larger fields of view. Attempts to address these issues have included the application of compressive sensing [30]–[32], deep neural networks [33], and methods centered around principal component analysis (PCA) [34]. Each of these solutions has its own limitations in terms of heavy computational requirements and large file sizes for data cube analysis.

1.3 WAVELENGTH SELECTION

One way to address these disadvantages is through implementation of a wavelength selection approach where only a specific subset of the narrowband wavelength bands is used for the desired application. The goal of this approach is to select only those wavelengths which provide the most information for solving the problem of interest, thus enabling a reduction in the wavelengths that need to be collected. This in turn allows for less complex collection devices and reduces the file sizes of the collected data cubes.

Wavelength selection for hyperspectral technologies is a well-studied problem. Ayala et al. [35] provides a thorough review of the state-of-the-art in wavelength selection algorithms for biomedical imaging applications and offers its own selection algorithm based on a domain adaptation technique. Marois et al. [36] proposes a wavelength selection for general chromophore concentration estimation based on a novel nonlinear least squares algorithm which performs selection by maximizing the singular values of a scattering-modulated absorption matrix. While these techniques have shown high accuracy in tissue oxygenation estimation in general, none of these have focused in particular on the ability to achieve this accuracy across all skin types.

1.3 RESEARCH OBJECTIVES

The objective of this research was to develop algorithms and methods for wavelength selection, classification, and regression for specific applications related to food safety and biomedical analysis. A guiding principle in these efforts was the desire for the resulting algorithms to enable development of a family of inexpensive, portable devices each designed for an individual application. As such, the algorithms needed to (1) achieve a significant reduction in the number of wavelengths required for collection, and (2) be compatible with hardware designs featuring inexpensive LEDs and/or filters with relatively wide bandwidths and unstable peak wavelengths.

1.4 APPROACH

We focused our efforts on two applications: (1) fish classification by species to combat food fraud and (2) estimation of tissue oxygenation for diabetic foot wound monitoring. The first application, though worthwhile in its own right, served as a proving ground for the initial algorithm development. The absorption spectra of fish flesh tend to be spatially homogeneous which greatly simplifies the per-pixel classification problem. We considered this study as a “phantom” study for the wound monitoring problem which is more complicated due to the great variability in skin types and physiological aspects between people, as well as the spatial variability in the skin of an individual.

1.5 DISSERTATION OUTLINE

This dissertation is organized into six chapters. The first chapter provides an introduction to hyperspectral imaging applications and algorithms and discusses the goals of this research.

The next four chapters detail individual studies that we performed in pursuit of these research goals. Chapter 2 describes our first investigation of wavelength selection for fish fillet species classification. The approach taken for this study featured a genetic algorithm-based selection method with and without spectrum reconstruction. Classification on a dataset of 14 fillets representing 6 different species, with both visible near-infrared (VNIR) and fluorescence spectra, was conducted using several common machine learning classifiers, and the results for compared.

Chapter 3 continues with the fish fillet species classification application, but discusses a new approach based on feature selection using a self-organizing map (SOM). For this study, wavelengths were treated as features to be fed as input to machine learning classifiers, and the SOM was employed as a feature selection technique to identify wavelengths offering non-redundant information. Classification results using the SOM method on the same dataset of 14 fillets are compared with those using the genetic algorithm method from Chapter 1.

The culmination of the fish fillet species classification effort is discussed in Chapter 4 where the genetic algorithm of the first study is replaced by simulated annealing. A simple multilayer perceptron (MLP) classifier was added to the assortment of machine learning classifiers, and results are provided for an expanded dataset of 133 fillets representing 25 species. Spectra for this dataset were taken in VNIR, fluorescence, and short-wave infrared (SWIR) modes. Classification results are provided for individually for the modes and for the fusion of the modes.

Chapter 5 turns to the wound monitoring application and the problem of tissue oxygenation (SO_2) estimation. The simulated annealing approach from Chapter 4 is employed here with the Extended Modified Lambert-Beer law (EMLB) performing the estimation function. Performance is validated using both Monte Carlo simulation data and *in vivo* data collected from 13 volunteers during an arterial occlusion study. In keeping with our research goals, we measure performance for the Monte Carlo dataset as a whole and broken out by melanin fraction to illustrate our algorithms' potential for enabling reliable wound monitoring for all skin types. Additionally, we measure performance with the original validation data and with a version of the data convolved with a 15 nm full width half maximum (FWHM) Gaussian filter to simulate data collection by the type of LED that might be found in an inexpensive portable wound monitoring device.

Finally, Chapter 6 summarizes the findings of this dissertation research and gives recommendations for expanding upon this research in future work.

CHAPTER 2. CLASSIFICATION OF FISH SPECIES USING GENETIC ALGORITHM WAVELENGTH SELECTION AND SPECTRAL RECONSTRUCTION

2.1 INTRODUCTION

The goal of this initial effort was to show proof of concept for a new method for rapid collection of spectral image data while minimizing file size and computational resource requirements. Our proposed rapid spectral imaging system consisted of two main components. The first is a focal plane array covered with a mosaic color filter array or selected wavelength LEDs that collects full spatial resolution images at small number (i.e., 3-5) of narrow wavelength bands. These wavelength bands are selected for the application using genetic algorithm-based optimization. The second component is a low-cost point spectrometer that collects a full resolution spectrum representing an average over all or part of the scene. This average spectrum was used as an input to a simple reconstruction algorithm to estimate the full data cube with minimal processing. This proposed method could be applied in a hand-held, mobile device for rapid scanning of food products in non-industrial commercial marketplaces or configured into a drone-deployable payload for low-altitude aerial scanning of crops and vegetation.

We showed proof of concept for this proposed method in a study based on a food fraud application involving the identification of the correct species of fish fillets [5]. Visible/near-infrared (VNIR) reflectance and fluorescence data for a total of 14 fish fillets representing six different species were used. We selected sets of 3 to 25 wavelength bands using a genetic algorithm and calculated the normalized root mean squared error (NRMSE) for each to determine the value at which the error curve flattens. Confidence intervals (95%) are calculated for all sets of wavelength bands to determine the variability of the optimization method results. Finally, we conducted a classification study to evaluate the utility of our wavelength band selection and spectral reconstruction method. Our results indicate that this method does indeed yield classification accuracies close to those using the original full spectral resolution data, even for the stress-testing cases where only 3-5 wavelength bands are selected.

2.2 MATERIALS AND METHODS

2.2.1 Hyperspectral Imaging System

Full-resolution reflectance and fluorescence images were collected using an in-house developed visible and near-infrared (VNIR) hyperspectral imaging system [37]. The light source for VNIR reflectance was a 150 W quartz tungsten lamp (Dolan Jenner, Boxborough, MA, USA). For fluorescence imaging, two UV line light sources were used, each with four 10 W, 365 nm, light-emitting diodes (LEDs) (Led Engin, San Jose, CA, USA). Reflectance images in 125 bands within the 419-1007 nm spectral range (4.4 nm at FWHM) and fluorescence images in 60 bands within the 438-718 nm range (4.4 nm at FWHM) were acquired using a 23 mm focal length lens, an imaging spectrograph (Hyperspec-VNIR, Headwall Photonics, Fitchburg, MA, USA), and a 14-bit electron-multiplying charge-coupled device (EMCCD) camera (Luca DL 604M, Andor Technology, South Windsor, CT, USA).

2.2.2 Spectral Reconstruction Algorithm

We developed a simple spectral reconstruction algorithm based on samples taken at a small number of wavelength bands, *k*, within the relevant spectral range and a full-resolution spectral average taken over the entire scene. The scene is a homogenous region of the sample being analyzed (no background regions). We refer to this spectral average as the “reference spectrum.” Our reconstruction algorithm uses the reference spectrum to estimate the reflectance/fluorescence values at the missing *N* - *k* wavelengths. This interpolation is conducted in a piecewise-linear manner by fixing the values at the sampled wavelength band centers and using the point-to-point slopes from the corresponding region of the reference spectrum to estimate values at wavelengths in between in both the forward (i.e., increasing wavelengths) and backward directions. A weighted average of the corresponding points from these spectrum estimates yields the resulting reconstruction. This process is repeated for every pair of successive sampled bands until the entire spectral range has been covered. Figure 1 provides an illustration of this method.

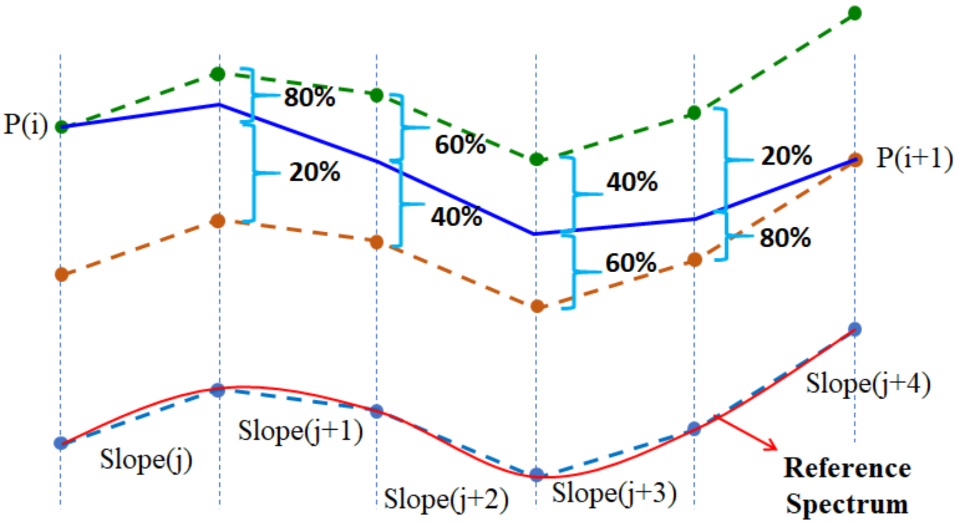

Figure 1. Illustration of the spectral reconstruction algorithm. Spectrum values have been sampled at bands indicated by points P(i) and P(i+1). Point-to-point slopes at full resolution are calculated from the reference spectrum (in red) and used to calculate a forward estimation (dashed green line) anchored at P(i) and a backward estimation (dashed orange line) anchored at P(i+1). The final full resolution estimate (solid blue line) is determined by taking weighted averages of the forward and backward estimates.

2.2.3 Sample Augmentation

If the first and last wavelengths of the relevant spectrum are not included in the set of sampled bands, we conduct an augmentation step to estimate these values and the values for the wavelengths between these and the lowest and highest sampled wavelengths. Given a set of spectral samples $P(i), i \in 1, 2, \cdots, k$ and a reference spectrum, $S(j), j \in 1, 2, \cdots, N$, with a full resolution of N wavelengths $\lambda_1, \cdots, \lambda_N$, we first augment these samples by estimating values for the first and last wavelengths in the range. Let the wavelength of the first sample point, $P(1)$, be $\lambda_{P(1)}$and of the last sample point, $P(k)$, be $\lambda_{P(k)}$. For a reference spectrum $S(\lambda_j), j \in 1, 2, \cdots, N$, these augmented estimates are determined as follows.

$$P(0) = P(1) - \left[S\left(\lambda_{P(1)}\right) - S(\lambda_1)\right] \tag{2.1}$$

$$P(k+1) = P(k) - \left[S(\lambda_N) - S\left(\lambda_{P(k)}\right)\right] \tag{2.2}$$

2.2.4 Forward and Backward Estimates

As described above, interpolation between sample points $P(i)$ and $P(i+1)$ is accomplished by taking weighted averages of estimates brought forward from $P(i)$ and backward from $P(i+1)$. Let us assume that $\lambda_p = 1, 2, \cdots, M$ are the wavelengths for the points at full resolution between $P(i)$ and $P(i+1)$. The forward estimates are calculated in the following recursive manner:

For p = 1 to M:

$$P_{forward}(p) = P_{forward}(p-1) + \left[S\left(\lambda_{p+1}\right) - S\left(\lambda_p\right)\right] \tag{2.3}$$

where $P_{forward}(0) = i$. The backward estimates are calculated in a similar recursive manner:

For p = M to 1:

$$P_{backward}(p) = P_{backward}(p+1) - \left[S(\lambda_{p+1}) - S(\lambda_p)\right] \tag{2.4}$$

where $P_{backward}(M+1) = i+1$.

2.2.4 Weighted Averages

Having determined the forward and backward estimates, we now calculate a weighted average that yields the final interpolated values. For the backward estimates, the weights are calculated as:

$$w_{p,backward} = \frac{p}{M+1} \tag{2.5}$$

The values for the forward weights are the same, but in the reversed order:

$$w_{p,forward} = \frac{M-p+1}{M+1} \tag{2.6}$$

The final interpolated values are given by:

$$P_{interp}(p) = w_{p,forward} \cdot P_{forward}(p) + w_{p,backard} \cdot P_{backward}(p) \tag{2.7}$$

The complete spectral reconstruction algorithm is summarized in Table 1.

Table 1. Spectral reconstruction algorithm

Step	Description
1.	Calculate spectral average over all valid pixels.
2.	Record values at selected wavelengths.
3.	Augment samples by estimating values at the first and last wavelengths of the full-resolution spectrum.
4.	For each successive pair of sampled wavelengths, *j* and *j* + 1: a. Determine the number of wavelengths, *m*. b. Use the reference spectrum to determine the slopes between the measured values at the selected wavelengths and those at the wavelengths in between. c. Use the slopes to project the spectral estimates forward from the spectral value at sampled wavelength *j* and backward from sampled wavelength *j* + 1. d. Create a set of weights based on the number of in-between wavelengths. e. Estimate the spectral value at each of the in-between wavelengths by taking a weighted average of the forward and backward projections at that wavelength.

2.3 GENETIC ALGORITHM

We use a genetic algorithm to solve the following optimization problem:

$$\begin{gathered} \mathit{Minimize}\ f(\boldsymbol{x}_k) = \textstyle\sum_{j=1}^{N} \omega_j \left(S(j) - P_{interp}(j)\right)^2 : \\ \mathit{Subject\ to:}\ \|\boldsymbol{x}_k\|_0 = k \\ 1 \le x_k(l) \le N \quad \forall\, l \in 1, 2, \cdots, k \\ x_k(l) \in \mathbb{Z} \\ \textstyle\sum_{j=1}^{N} \omega_j = 1.0 \end{gathered} \tag{2.8}$$

In this way we minimize a weighted sum of squared errors over the full-resolution spectral range. The first constraint simply restricts the number of wavelength samples to no more than *k*. The second constraint restricts the indices of the sampled wavelengths (which form the vector $\boldsymbol{x}$) to fall within the bounds of the indices of the full-resolution spectrum (i.e., 1 and *N*). The third constraint ensures that this vector is integer valued. Finally, the last constraint ensures that weights are properly normalized.

The genetic algorithm is implemented using Matlab's Global Optimization Toolkit [38]. This heuristic optimization method works by creating a "population" of trial solutions (i.e., "chromosomes") and calculating the "fitness" of each. In our case, each chromosome consists of *k* wavelengths and the fitness is determined by the spectral reconstruction error. The chromosomes in the population are then sorted and a selected number of the most fit chromosomes (i.e., the "elite count") are passed on to fill most of the population for the next generation. The remainder of the population is filled via a tournament selection process whereby a small number (four in our case) of chromosomes from the preceding generation are selected at random and the one with the highest fitness is selected as a “parent.” Two parents are selected in this process and are combined to generate two “children” for the new population. This occurs by combining a portion (i.e., the “crossover fraction”) of the first parent and the remainder from the second parent to form the first child. The second child is formed similarly by combining the opposite portions of both parents. We set the number of chromosomes per generation to 300, the elite count to 30, and the crossover fraction to 0.9. After each generation, the minimum error and corresponding chromosome were recorded. The genetic algorithm was allowed to continue until 75 consecutive generations passed with no change in minimum error.

The genetic algorithm is a heuristic method with no guarantee of identifying the global minimum. We enhanced this optimization method in two ways. First, we used the winning chromosome resulting from the k = m – 1 iteration to inform the starting point for the k = m iteration (with the mth wavelength selected at random). Second, we followed the genetic algorithm with a Generalized Pattern Search (GPS) using the result of the genetic algorithm as the starting point [39]. The GPS algorithm creates a mesh, centered on the starting point, that is defined by a set of direction vectors and a scalar mesh size. At each iteration, the objective function is evaluated at each of the new points until one is found that produces a value less than the current minimum value. This new point is selected as the new starting point and the search continues with the same (or larger) mesh size. If none of the points produces a lower objective function value, then the mesh size is reduced and the process continues until the mesh size reaches a minimum threshold [40]. In this manner, the GPS algorithm can help to push the genetic algorithm solution out of a local optimum and move it to the global optimum (assuming these points are in the same vicinity).

2.4 DATA

2.4.1 Fish Fillet Data Collection

Our database for this study consisted of VNIR reflectance and fluorescence spectra collected from 14 fish fillets of six different species (six red snapper, four Malabar snapper, one vermillion snapper, one summer flounder, one blue tilapia, and one white bass). Each fillet was placed in a 150 × 100 × 25 mm^3 sample holder created with a 3D printer (Fortus 250 mc, Stratasys, Eden Prairie, MN, USA) using production-grade black thermoplastic. Image acquisition used the pushbroom method whereby a linear motorized translation stage was used to move the sample holder incrementally across the scanning line of the imaging spectrograph. The length of the instantaneous field of view (IFOV) was made slightly longer than the length of the sample holder (150 mm) by adjusting the lens-to-sample distance. The resulting spatial resolution along this dimension was determined as 0.4 mm/pixel. Each fillet was sampled along the width direction (100 mm) of the holder with a step size of 0.4 mm to match the spatial resolution of the length direction [5].

Flat-field corrections were applied to the VNIR reflectance images and the fluorescence images to convert original absolute intensities in CCD counts to relative reflectance and fluorescence intensities [20]. An initial spatial mask was then created for each imaging mode to separate the fish fillets from the background. Outliers were handled by first calculating the mean (μ) and standard deviation (σ) of the fish pixel intensities over the entire fillet. We considered 10 × 10 pixel region “blocks” to mimic independent fish fillet spectral point measurements using the field of view of a fiber optic spectrometer. We also have an exclusion criteria where if $\geq$10% of the constituent pixels in a block exceeded $\mu \pm 2\,\sigma$ to eliminate outliers. This approach produced a final set of spatial masks, one each for the reflectance and fluorescence images, that determined the blocks to be used for analysis. Table 2 lists the number of valid blocks for each fillet and each collection mode.

Table 2. Fish fillet database summary.

Fillet	Collection Mode	Number of Fillets	Number of Valid Blocks
Red Snapper	VNIR	6	2,401
Malabar Snapper	VNIR	4	1,599
Vermillion Snapper	VNIR	1	283
Summer Flounder	VNIR	1	316
Blue Tilapia	VNIR	1	250
White Bass	VNIR	1	280
Red Snapper	Fluorescence	6	2,423
Malabar Snapper	Fluorescence	4	1,517
Vermillion Snapper	Fluorescence	1	504
Summer Flounder	Fluorescence	1	516
Blue Tilapia	Fluorescence	1	345
White Bass	Fluorescence	1	387

The average reflectance and fluorescence spectra for each of the six fish species is shown in Figure 2. The spectra for all six species (including the red snapper and the Malabar snapper) were calculated from the pixels of a single fillet. VNIR reflectance and fluorescence spectra for individual blocks from one red snapper image are shown in Figure 3 along with the average spectrum. The significant differences in the shapes and positions of the spectral averages for the various species and homogeneous nature of the spectra for pixels of a single fillet suggest that high classification accuracies can be achieved with this spectral information. Note, however, that the point of this study is not to demonstrate high classification accuracy, but to demonstrate how the proposed wavelength band selection and spectral reconstruction methodology can yield classification accuracies on par with those resulting from the original full spectral resolution data.

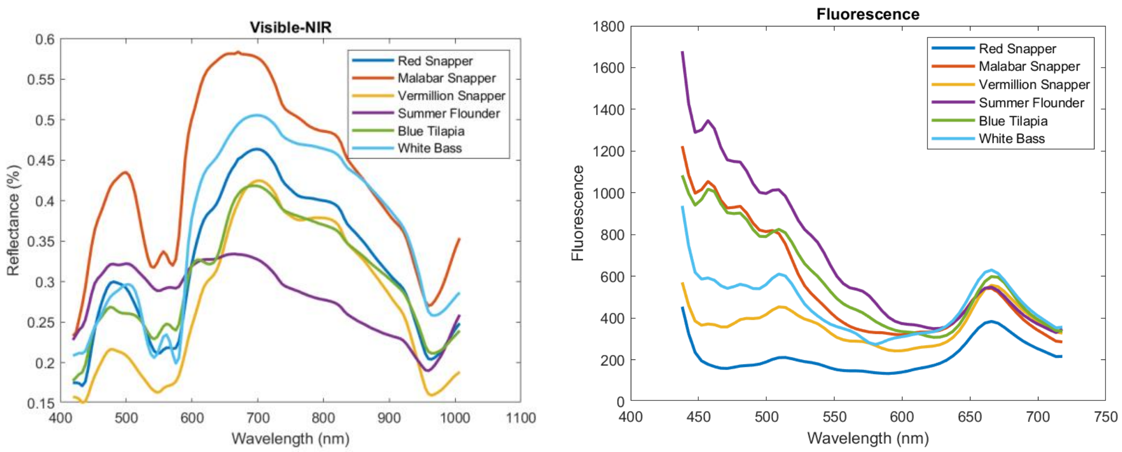

Figure 2. Average reflectance (left) and fluorescence (right) spectra for each of the six fish species.

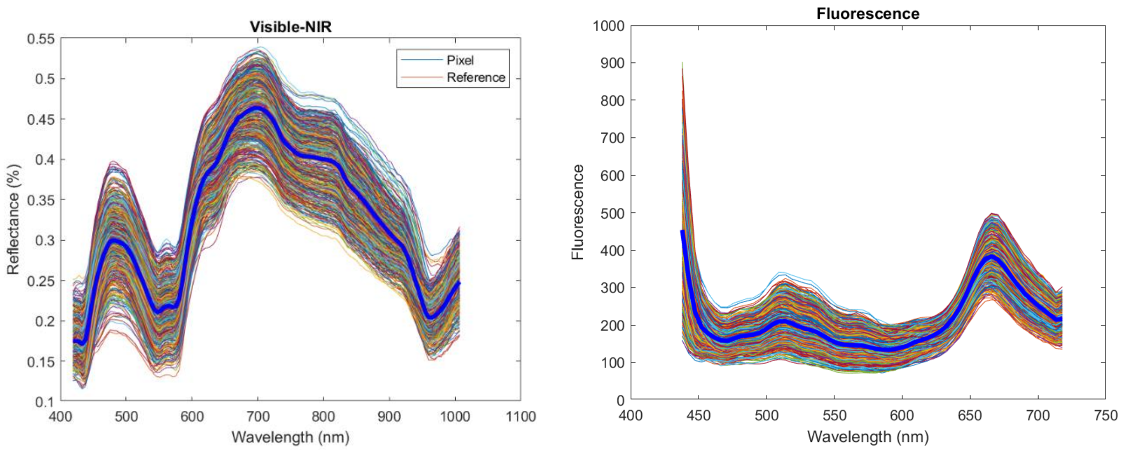

Figure 3. VNIR reflectance (left) and fluorescence (right) spectra for each pixel of one of the red snapper fillets. The solid blue curves denote the average spectrum over all pixels.

2.5 RESULTS

2.5.1 Validation of selected wavelength Sets

Plots of the average NMRSE and the associated 95% confidence intervals resulting from the optimization process described above, for k = 3 to 25, are shown in Figure 4. Results for the VNIR reflectance dataset are on the left and for the fluorescence dataset on the right. Confidence intervals were calculated from the results of 10 separate iterations of this optimization process for each *k* value and dataset type. For both the VNIR and the fluorescence datasets, the confidence intervals are widest in the *k* = 5 to 12 range but significantly narrower for *k* = 3 and for *k* > 12. This suggests that the selection of wavelengths is most critical in the *k* = 5 to *k* =12 range where minor differences in winning chromosomes between iterations can lead to larger differences in error. For large *k* values, very similar error values can be attained with a more varied selection of wavelengths.

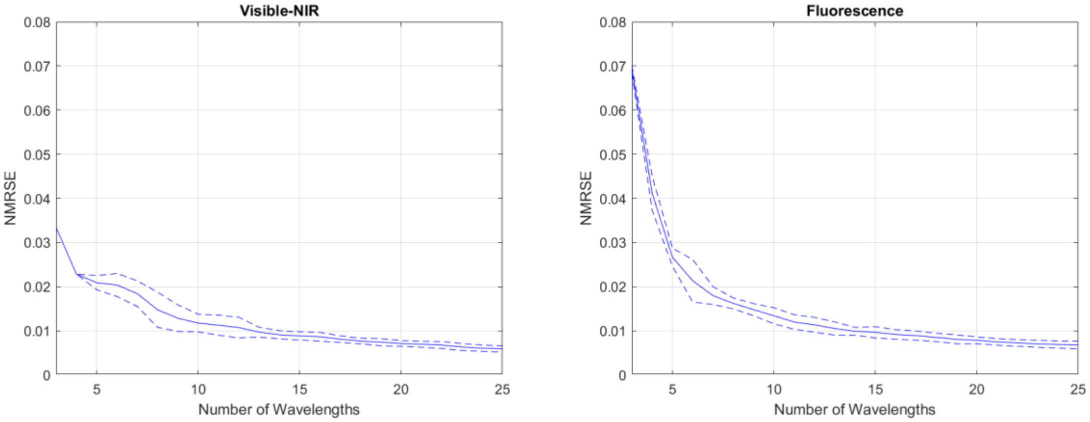

Figure 4. Average NRMSE (solid curves) and 95% confidence intervals (dashed curves) for the VNIR reflectance (left) and fluorescence (right) datasets following optimal wavelength band selection using the proposed genetic algorithm-based optimization method and a cost function based on the proposed spectral reconstruction algorithm.

2.5.2 Classification

Classification accuracies for the VNIR reflectance data based on the spectral values at the *k* = 3, 4, 5 optimal wavelengths are given in Table 3. The accuracies determined using the original full-resolution spectral data are provided in the “Original” column as a reference. Features based on the spectral values at the k optimal wavelength only are listed under the “No Reconstruction” column and those based on the reconstructed spectral values at all full-resolution wavelengths are listed under the “Spectral Reconstruction” column. The rightmost three columns in Table 3 list the corresponding accuracies with spectral reconstruction applied. Results for the fluorescence case are provided in a similar manner in Table 4. Values in bold denote the highest accuracy for the given classification algorithm and are determined separately for the "No Reconstruction" and the "Spectral Reconstruction" cases.

Table 3. Classification accuracies for the VNIR reflectance data.

Classifier	Original	No Reconstruction			Spectral Reconstruction		
		k = 3	*k* = 4	*k* = 5	*k* = 3	*k* = 4	*k* = 5
Linear Discriminant	100%	75.04%	77.02%	79.45%	99.98%	99.85%	99.70%
Quadratic SVM	99.65%	80.05%	83.33%	85.64%	96.35%	97.44%	97.88%
Weighted KNN	97.54%	80.97%	83.59%	84.90%	95.46%	96.04%	96.31%
Subspace Discriminant	100%	72.49%	74.70%	77.14%	99.94%	99.93%	99.93%

Table 4. Classification accuracies for the fluorescence data.

Classifier	Original	No Reconstruction			Spectral Reconstruction		
		k = 3	*k* = 4	*k* = 5	*k* = 3	*k* = 4	*k* = 5
Linear Discriminant	99.02%	78.36%	79.94%	82.94%	89.72%	91.66%	91.53%
Quadratic SVM	99.91%	92.16%	91.29%	93.52%	92.29%	94.42%	95.03%
Weighted KNN	98.23%	92.22%	91.52%	93.32%	95.22%	95.01%	95.79%
Subspace Discriminant	99.02%	76.12%	77.35%	81.05%	89.63%	91.65%	91.58%

2.6 CONCLUSIONS

This study was designed to show proof of concept for a new conceptual design of an inexpensive hyperspectral imaging device. Images collected with this device possess full spatial resolution and contain a relatively small number (i.e., 3, 4, or 5) of narrowband channels selected by a genetic algorithm optimization method followed by generalized pattern search. An integrated non-imaging optical spectrometer collects a full-resolution spectrum representing an average over the entire scene. The full hyperspectral data cube is then generated using a simple hyperspectral reconstruction algorithm.

A dataset containing VNIR reflectance and fluorescence data collected from 14 fish fillets representing six different species was used for this study. Results of the optimization study showed low reconstruction errors (as measured in terms of NMRSE) overall with flattening of the error curves for $k \geq 10$. The relevance of the combined wavelength selection and hyperspectral reconstruction algorithm was evaluated with a separate classification study. As expected, the classification accuracies dropped significantly when going from using the original full spectral resolution data to using the data at the $k = 3, 4, 5$ selected wavelengths only. However, these accuracies rose significantly when the hyperspectral reconstruction algorithm was applied. Furthermore, while the accuracies increased with k in general, the accuracies for the $k = 3$ case differed by only 2-3% from the highest value. These results confirm proof of concept for the suggested design of inexpensive hyperspectral imaging devices, at least for this food fraud application featuring homogenous spectral data.

CHAPTER 3. HYPERSPECTRAL BAND SELECTION FOR FOOD FRAUD APPLICATION USING SELF-ORGANIZING MAPS (SOM)

3.1 INTRODUCTION

Hyperspectral band selection has received much attention in recent years with various methods proposed for identifying optimal spectral band subsets. Of these, unsupervised methods are particularly attractive since they do not require a labeled dataset, which can be difficult and expensive to develop. Principal component analysis (PCA) [41] and independent component analysis (ICA) [42] are among the most popular dimensionality reduction techniques, a problem closely related to band selection. However, for this study, we place such methods in a separate category since they require access to the full set of wavelength bands. With regard to unsupervised hyperspectral band selection, then, leading methods include those based on correlation analysis [43], constrained energy minimization [44], and mutual information [45]. Recent additional methods include graph-based methods [46], [47], clustering methods [48], self-representation [49], rank minimization [50], and wavelet models [51]. All of these methods attempt to identify optimal subsets of bands by minimizing redundancies.

The primary limitation shared by nearly all these methods is that they can only account for linear correlations between bands. To overcome this limitation and account for inherent nonlinearities, some researchers have turned to self-organizing maps (SOMs). Based on the concept of competitive learning, SOMs identify a nonlinear transformation from high to low dimensional space such that the separation between points in the lower dimension is representative of the relative dissimilarity between their higher dimensional counterparts. The Feature Competitive Algorithm (FCA) proposed by Ye and Liu [52] is a general feature selection method that works by identifying those features in the original high dimensional space that align best with the trained "reference vectors" of the SOM. The Subspace Clustering Based on SOM (SCBSOM) [53] method proposed by Tian and Gu applies a one-dimensional clustering in each dimension based on the weight connections in the learned SOM followed by a merging process. Benabdeslem's and Lebbah's Heuristic Input for SOM (HI-SOM) [54] similarly applies clustering in the trained SOM for feature selection. However, although SOMs have been used to enhance the classification of hyperspectral images [55], to our knowledge, no other researchers have investigated the use of SOM for hyperspectral band selection.

In this chapter, we introduce a new hyperspectral band selection method based on the exploitation of the relationships between weights in the trained SOM's reference vectors. We use the mean distance between pairs of "weight planes" (i.e., a high dimensional plane formed by the weights from all trained reference vectors corresponding to the same input band) as a measure of the nonlinear correlation between the bands. We refer to this measure as the Weight Plan Distance (WPD). Although visual inspection of weight planes to evaluate redundancy has been suggested by others [56], [57], to our knowledge, this is the first proposal of a completely automated method based on weight plane analysis. We apply this method to a food fraud application where hyperspectral imaging is used to determine the correct species of fish fillets. We compare the band selection and classification results of this method to those obtained by the authors where a genetic algorithm was used to select wavelength bands based on their ability to reconstruct the full resolution spectra with minimal error, and these same bands were in turn used as features for the species classification [58].

3.2 SELF-ORGANIZING MAP (SOM) METHOD

3.2.1 SOM and Weight Plane Distance (WPD)

Developed by Teuvo Kohonen in 1982 [59], the SOM is a type of two-layer artificial neural network that produces a low-dimensional (typically 2D) representation of vectors in a high-dimensional input feature space. It does this by applying unsupervised competitive learning to move the network's weights closer to the input vector. For each input vector, the Euclidian distance between this vector and the weight vectors (called "reference vectors") for all output neurons is calculated. The neuron with the smallest distance is declared the "best matching unit" (BMU), and the reference vectors for all neurons within a neighborhood of the BMU are updated. This "neighborhood" is defined with a neighborhood function, $h_{ci}(t)$, where the c subscript refers to the index of the BMU and the i subscript refers to the i^{th} neuron [60]. The updated weight for the i^{th} reference vector is then given by:

$$\boldsymbol{w}_i(t+1) = \boldsymbol{w}_i(t) + \alpha \cdot h_{ci}(t) \cdot [\boldsymbol{x}(t) - \boldsymbol{w}_{\boldsymbol{i}}(t)] \tag{3.1}$$

Figure 1 shows the results of training an 8 × 8 SOM on Fisher's iris dataset [61]. The output layer neurons are arranged in a hexagonal pattern. Figure 5(a) shows a plot of the number of input vectors that are mapped to each output layer neuron. Figure 5(b) shows plots of the reference vector weight values at each output neuron for each input weight, with darker colors representing larger values. The collection of weight values for each input is commonly referred to as a "component plane" or "weight plane" [62].

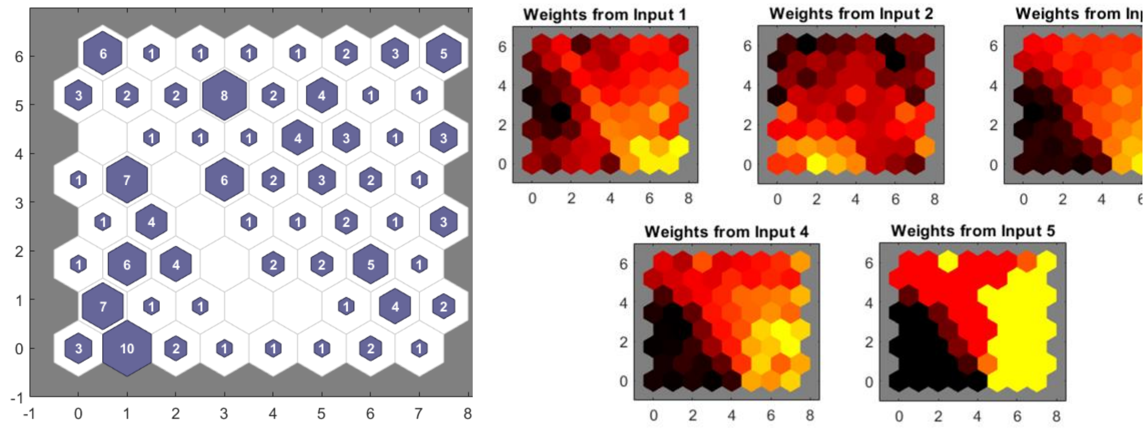

(a) (b)

Figure 5. Results of SOM trained on Fisher’s iris dataset. (a) Plot of the number of input vectors mapped to each neuron in the output layer; (b) Colored plots of the weight values for each input weight plane. Darker colors indicate larger weight values.

We compute the weight plane distances (WPD) by calculating the squared difference between the value of a node in one weight plane and the corresponding node in another weight plane. This calculation is repeated for all nodes, and the squared differences are then averaged to yield the WPD between these two weight planes. The complete set of WPDs is computed by calculating the WPD between each pair of weight planes. This WPD set would yield a symmetric N × N matrix, where N is the number of nodes in the SOM. For efficiency, we compute only one half of this matrix and set the entries in the other half to zero. As Figure 6 shows, this half matrix can be plotted to represent the 3D structure of the WPD. Finding the peaks in this structure thus equates to identifying those pairings of bands that have the least redundancy.

Figure 6 hints at the true benefit of this SOM WPD approach. This method provides a means of band selection based on minimization of redundancy, and it also provides a measure of importance for exact band selection. For example, a tall but broad peak in the WPD matrix suggests that we could select any pair of bands in the vicinity of the true local optimum and still achieve a near-maximum degree of non-redundancy. This could be particularly beneficial in designing a sparse hyperspectral imaging system where the collection of imagery at certain wavelengths may be easier to engineer than at others.

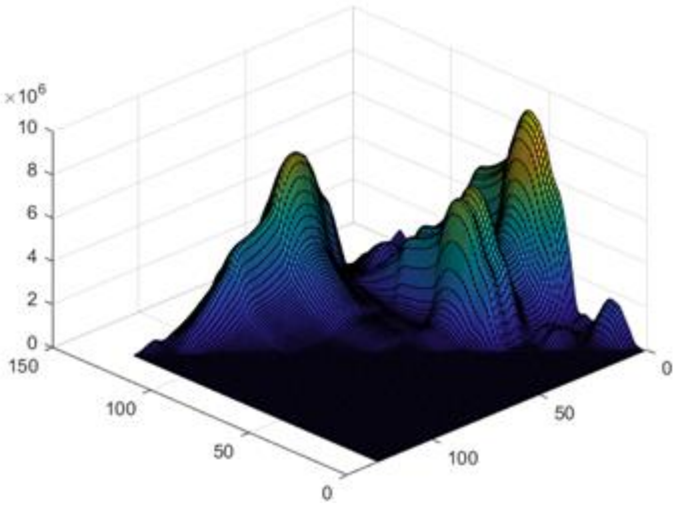

Figure 6. Surface plot of the WPD from for the VNIR data in our fish fillet species classification study. Each peak represents a local maximum non-redundancy between features. Note that we calculate values for only half of the otherwise symmetric WPD matrix.

3.2.2 Peak Finding and Feature Ranking

To select features using the WPD matrix, we first find local peaks along each row of the WPD matrix. The WPD values at these peak locations are saved in an intermediate matrix while the values at other locations are zeroed. We then apply the same process along each column of this intermediate matrix to identify the final WPD peaks. We apply this two-stage process to better eliminate the false peaks that can appear when using 2D peak finder algorithms.

Feature ranking is then conducted using the WPD values at the selected peaks. For example, the two features corresponding to the tallest peak in Figure 2 (i.e., the two features with the largest WPD) are assigned ranks one and two. The two features corresponding to the next tallest peaks are assigned ranks three and four, and so on.

3.3 CLASSIFICATION OF FISH SPECIES

We used the bands selected by our SOM-based method as features to train four conventional machine learning classifiers – linear discriminant, quadratic support vector machine (SVM), weighted k-nearest neighbors (WKNN), and subspace discriminant (an ensemble method which applies linear discriminants to random subsets of features). These classifiers were then used to classify the correct species of fish fillet based on information from one pixel's visible/near-infrared (VNIR) reflectance or fluorescence spectrum. This classification was repeated for numbers of selected wavelengths, k = 3, 4, and 5, and a 5-fold cross-validation was conducted as a robust estimation of classification accuracy. This SOM-based method's performance was evaluated via comparison with the results from the genetic algorithm method [58].

3.4 FISH FILLET DATA COLLECTION

The same dataset consisting of VNIR and fluorescence spectra of14 fish fillets representing 6 different species discussed in Chapter 2 was used for this study. Table 2 and Figure 3 provide details of this dataset and show example spectra.

3.5 RESULTS

3.5.1 Peak Finding and Feature Selection

Figure 7 shows the WPD plot for the VNIR data with the results of the peak finding algorithm added as red asterisks. The terrain of this WPD matrix is near-optimal for realizing the benefits of the SOM WPD band selection method. Prominent peaks rise above the floor of the surface plot to represent apparent differences between regions of high WPD values (and hence little redundancy between the associated bands) and low WPD values. Notice that the algorithm has successfully isolated the local maximum for each peak. Notice also that the algorithm has identified several peaks near the floor of the surface plot with very low WPD values. We consider this an acceptable outcome of the band selection process since a threshold based on the number of bands, or WPD values can easily be added based on user needs.

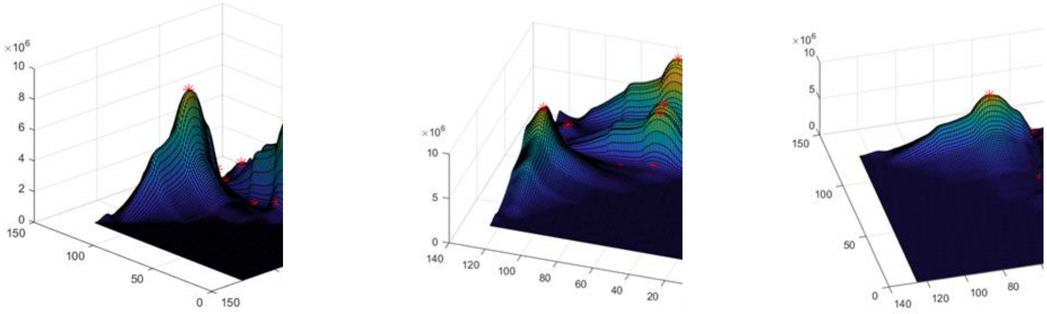

Figure 7. Results of the peak finding algorithm for the VNIR data displayed from three different angles. Identified peaks are denoted with the red asterisks.

Figure 8 shows the peak selections for the fluorescence data. The terrain in this case is not as favorable as that for the VNIR case. There are only two prominent peaks that can be seen by eye, both of which slope down slowly in each direction. Furthermore, the broader peak has a “double bump” that confuses the peak finder algorithm, causing it to make two selections when one is likely more appropriate. As these peaks slope downward toward the diagonal of the WPD matrix, there are ridges in the profile that cause the algorithm to find more questionable local peaks.

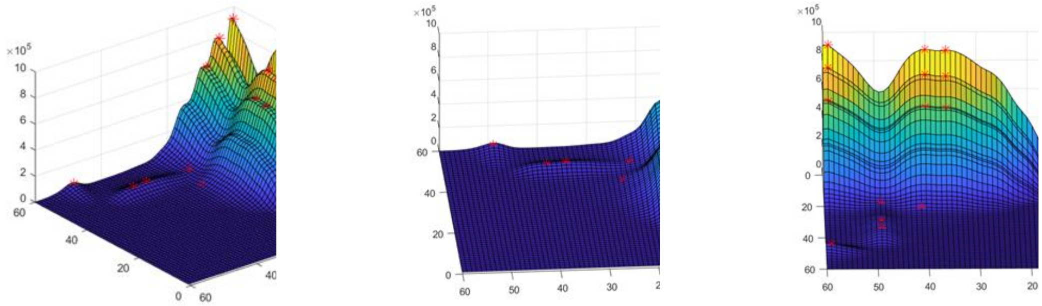

Figure 8. Results of the peak finding algorithm for the fluorescence data displayed from three different angles. Identified peaks are denoted with the red asterisks.

Table 5. Top five selected VNIR wavelength bands (and corresponding indices) ranked by WPD value.

Method	**Selected Wavelength Bands (nm, ordered by rank)**	
	VNIR	**Fluorescence**
SOM WPD	419.3 (1), 694.2 (59), 964.4 (116), 542.5 (27), 571.0 (33)	438.2 (1), 713.2 (59), 623.1 (40), 604.1 (36), 457.2 (5)
Genetic Algorithm	523.6 (23), 675.2 (55), 860.1(94), 898.0 (102), 959.7 (115)	447.7 (3), 499.9 (14), 566.2 (28), 642.1 (44), 694.2 (55)

Table 5 gives the wavelengths and corresponding indices for the top five selected bands for the VNIR and fluorescence data. For the SOM WPD method, the bands are listed in the WPD rank order. We immediately notice some significant discrepancies between the selections made by these two methods. For example, for both the VNIR and fluorescence data, the first wavelength band is the top-ranked band for the SOM WPD method but does not even appear in the list of selections by the genetic algorithm method. This discrepancy is likely a consequence of the spectral reconstruction process, which estimates values at the initial and final bands in the spectral range based on forward and backward projection from the lowest and highest selected bands, respectively. Other selections by the two methods appear to match within a few index values (e.g., bands 59 and 55 for the VNIR data and bands 40 and 44 for the fluorescence data). These discrepancies can be resolved by looking at the peaks in Figures 6 and 7 to determine if these selected bands have significantly different WPD values. We find that the WPD difference for bands 59 and 55 in the VNIR data is relatively small (3.4%) when we look along the same peak but is significantly larger (10.3%) for bands 40 and 44 in the fluorescence data.

3.6 CLASSIFICATION RESULTS

The classification results for the VNIR and fluorescence data are listed in Table 6 and Table 7. For each classification algorithm, the classification experiment was repeated for the top k = 3, 4, and 5 selected wavelength bands. The highest classification accuracy for each classification algorithm and band selection method (over all k values) are bolded. The SOM WPD method has yielded the higher classification accuracy for 2 of the 4 classifiers with the VNIR data and all 4 classifiers with the fluorescence data.

Table 6. Classification accuracies for the Genetic Algorithm and SOM WPD methods with the VNIR data.

Method	**Genetic Algorithm**			**SOM WPD**		
	k = 3	**k = 4**	**k = 5**	**k = 3**	**k = 4**	**k = 5**
Linear Discriminant	75.04%	77.02%	79.45%	74.40%	78.57%	78.40%
Quadratic SVM	80.05%	83.33%	85.64%	78.69%	84.93%	87.91%
Weighted KNN	80.97%	83.59%	84.90%	79.12%	85.98%	88.03%
Subspace Discriminant	72.49%	74.70%	77.14%	70.05%	71.83%	72.43%

Table 7. Classification accuracies for the Genetic Algorithm and SOM WPD methods with the fluorescence data.

Method	**Genetic Algorithm**			**SOM WPD**		
	k = 3	**k = 4**	**k = 5**	**k = 3**	**k = 4**	**k = 5**
Linear Discriminant	78.36%	79.94%	82.94%	79.55%	86.53%	87.30%
Quadratic SVM	92.16%	91.29%	93.52%	86.33%	94.52%	96.98%
Weighted KNN	92.22%	91.52%	93.32%	88.21%	93.24%	95.80%
Subspace Discriminant	76.12%	77.35%	81.05%	75.51%	74.72%	95.98%

3.7 CONCLUSIONS

This study was conducted with two primary goals. The first was to evaluate a new method for hyperspectral wavelength band selection based on the average distance between the weight planes formed by a trained SOM's reference vector values. The second was to compare the band selections and classification performance of this new method with a genetic algorithm-based method applied in the study described in Chapter 2 and published in [5]. As in the earlier study, we used hyperspectral imaging data collected in both VNIR and fluorescence ranges to perform this evaluation and comparison. The classification portion of this study consisted of 10 × 10-pixel block-wise classification of the species of a fish fillet using four conventional machine learning classifiers and the VNIR/fluorescence values from the selected bands as the input features. This classification serves as a means of preventing a common food fraud technique where fish fillets of one species (e.g., blue tilapia, white bass, summer flounder) are labeled and sold as a more expensive species (e.g., red snapper).

Surface plots of the WPD matrix values showed prominent peaks representing pairings of wavelength bands with large distances between their respective weight planes (and hence, low redundancy between the bands). This situation was more evident for the VNIR data than for the fluorescence data. Band selections differed significantly between the original genetic algorithm-based method and the new SOM WPD method. Using the WPD surface plots to determine the significance of these discrepancies in redundancy between bands, we found that the disparities were more significant for the fluorescence data than for the VNIR data.

Results of the classification analysis clearly favored the new SOM WPD method, with 2 of the 4 classifiers yielding higher accuracies for this method with the VNIR data and all 4 yielding higher accuracies for the fluorescence data. However, we note that the genetic algorithm-based method used in [5] was designed to optimize spectral reconstruction and not classification directly.

The results of this study indicated promise for the new SOM WPD method and highlight room for improvement. For example, the peak finding algorithm was shown to locate peaks in the fluorescence WPD values that appear somewhat redundant. Also, the method described in this chapter selects wavelength bands two at a time by finding peaks in the WPD matrix, but it does not include a follow-up step where all selected bands are paired and the corresponding WPD value is measured against an acceptance threshold to reduce redundancies further. Future studies should address these algorithm issues and evaluate the robustness of the SOM WPD method by testing it on other hyperspectral imaging datasets.

CHAPTER 4. SIMULATED ANNEALING-BASED HYPERSPECTRAL DATA OPTIMIZATION FOR FISH SPECIES CLASSIFICATION

4.1 INTRODUCTION

This chapter discusses the third and final study related to the fish fillet species classification application. In this study, we expanded our dataset both in terms of number of fillets and in number of represented species. In addition to the SWIR and fluorescence modes, we also added a short-wave infrared (SWIR) mode for data collection. The results of this study supported those of the previous two studies and showed improved classification accuracy through the inclusion of a multilayer perceptron (MLP) classifier. Classification results are provided for each spectral mode individually and for the fusion of modes which yielded the highest accuracy.

4.2 MATERIALS AND METHODS

2.1 Hyperspectral Imaging Systems

The same hyperspectral imaging system described in Section 2.2.1 was used to collect spectra in the VNIR and fluorescence modes. A separate hyperspectral imaging system was used to acquire reflectance images in the SWIR region. The illumination source for this system was a custom-designed two-unit lighting system, each with four 150 W gold-coated halogen lamps with MR16 reflectors. The detection unit included a 25 mm focal length lens and a hyperspectral camera, including a 16-bit mercury cadmium telluride array detector and an imaging spectrograph (Hyperspec-SWIR, Headwall Photonics, Fitchburg, MA, USA). The SWIR reflectance images were acquired in a wavelength range of 842-2532 nm (287 wavelengths).

4.3 SIMULATED ANNEALING

Rather than sensing the full resolution spectra in each of the three modes, the proposed method uses just a small number of narrow wavelength bands (referred to simply as “wavelengths” in this paper) that are specifically chosen to yield accurate species classifications. Simulated annealing, a heuristic optimization method modeled after the metallurgical annealing process in which the metal undergoes controlled cooling to remove defects and toughen it, was used to select the wavelengths. The simulated annealing algorithm consists of a discrete-time inhomogeneous Markov chain with current state $s(i)$ and a cooling schedule defined by a starting temperature, T_{max}, a final temperature, $T_{min} < T_{max}$, and a total number of steps, n [63]. The goal of the algorithm is to determine the minimum of a user-defined energy function, $E(i)$.

At each iteration $i \in 1, \cdots, n$, a new trial state is determined by randomly selecting a “neighbor” of the previous state and calculating its energy. If the resulting energy is less than the energy from the previous iteration, the trial state becomes the new state of the system. If the resulting energy exceeds the energy of the previous energy, the algorithm adopts the trial state with probability given by:

$$P\big(E(i), E(i-1)\big) = e^{-\frac{1}{T(i)}[E(i)-E(i-1)]} \tag{4.1}$$

where $T(i)$ is the temperature at iteration i. Note that this equation allows the algorithm to occasionally accept states that result in an increase in energy. This can benefit the optimization by preventing it from becoming stuck in local minima. The probability of accepting such states is high at the beginning of the process when the temperature is high but gradually decreases with decreasing temperature. The output of the algorithm is the state with the lowest energy encountered throughout the annealing schedule. Figure 9 provides a summary of this algorithm.

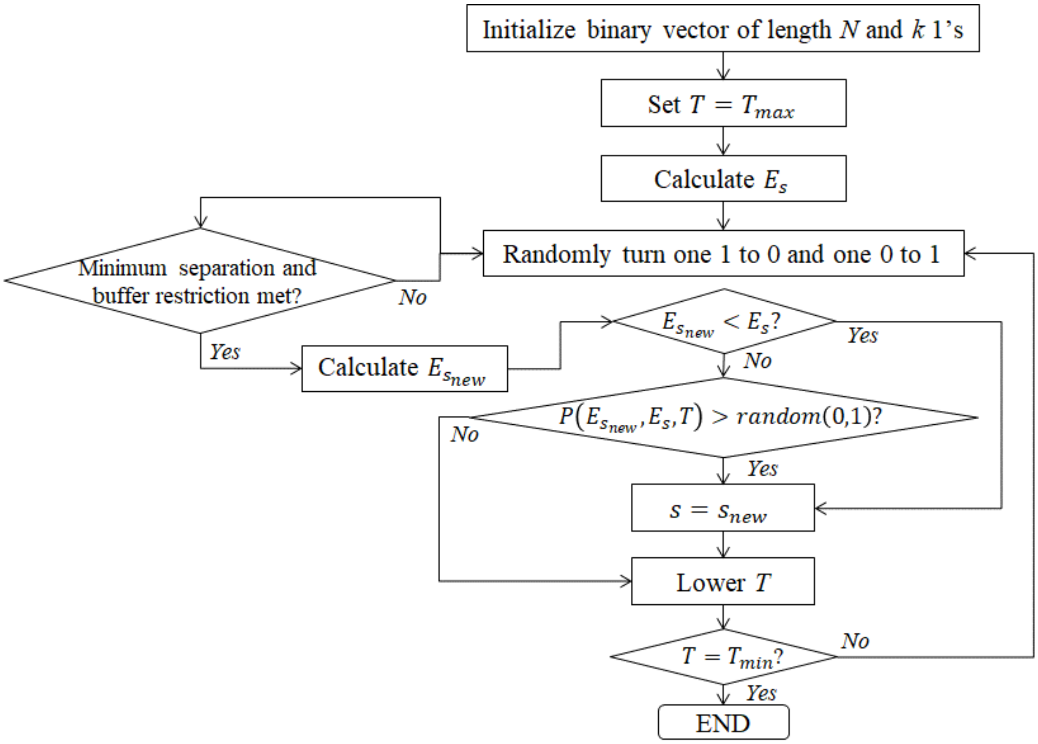

Figure 9. Flowchart for the simulated annealing algorithm used to select the best k wavelength for fish species classification.

For this wavelength selection problem, we define the state as an array of binary elements indicating the presence or absence of each wavelength in the full-resolution spectrum. Because the collected spectra may contain artifacts at the lowest and highest wavelengths, we institute a fixed buffer of size m at either end of the spectrum. Thus, the state at iteration i can be expressed as

$$s(i) = I(j)\ for\ j \in m + 1, \cdots, N - m - 1 \tag{4.2}$$

where $I(j)$ is 1 to indicate that the jth wavelength is selected and 0 to indicate it is not, and N is the total number of wavelengths in the spectrum. Furthermore, because consecutive wavelengths are highly correlated and thus offer little additional information if both are selected, we institute a minimum separation of q wavelength indices between selected wavelengths. Finally, we set a limit, k, on the number of wavelengths selected such that:

$$\sum_{j=m+1}^{N-m-1} I(j) = k \tag{4.3}$$

Under these three restrictions, we update the state for each iteration by generating a “neighbor” of the current system state. This is done by randomly de-selecting one wavelength index from the current state and selecting a new one. The energy of the trial state is then calculated as $1 - a(i)$ where $a(i)$ is the average 4-fold cross validation accuracy (see Section 2.5) as determined using the weighted k-nearest neighbors (WKNN) classifier. WKNN is a variation of the familiar k-nearest neighbors algorithm where the training data points are weighted based on the squared inverse of their distances from the query point. It was chosen as the basis for the energy calculation because of its relatively high classification performance and its rapid training time. Accuracy, in this sense, is calculated as the percentage of correct classifications, weighted by the number of samples per class in the test sets to ensure equal contribution from each class.

The simulated annealing algorithm was implemented in Python 3.7 using the *simanneal* 0.5.0 library [64]. The temperature parameters were set to $T_{max} = 25$ and $T_{min} = 0.05$ and the number of steps was set to $n = 5{,}000$. These temperature values were selected to ensure nearly 100% selection of new states in the initial steps, regardless of whether the energy decreased or increased, and nearly 0% selection of states that increased the energy during the final steps. The number of steps was chosen to balance the desire for rapid processing with the need for algorithm convergence.

4.4 CLASSIFICATION OF FISH SPECIES

To evaluate the success of the optimal wavelength selection algorithm, a pair of classification studies were conducted with the goal to determine the correct species of a fillet based on spectral information from a single sample point on the fillet represented by one 10 × 10 pixel block (i.e., voxel). For both studies, a multi-layer perceptron (MLP) neural network served as the primary classifier. In the first study, each spectral mode (i.e., VNIR, fluorescence, and SWIR) was investigated separately and the results of the MLP classifier were compared with results from a collection of common machine learning classifiers. The classifiers were trained on the spectral values from the selected wavelengths and evaluated using 4-fold cross-validation. In the second study, the selected wavelengths from the three spectral modes were combined in the input layer of the MLP classifier, and this spectral fusion method was again evaluated with 4-fold cross-validation. Both studies were repeated for numbers of selected wavelengths k = 3, 4, 5, 6, and 7. Results using all available wavelengths were included as a benchmark for comparison.

4.4.1 Multi-Layer Perceptron (MLP) Classifier

An MLP neural network is a common feed-forward artificial neural network that determines its weight values through supervised learning to yield a nonlinear decision boundary designed to minimize a cost function. In this case, the cost function was defined as the complement of the multiclass classification accuracy (weighted by the number of samples per class). The MLP classifier used for both the single-band and fusion studies consists of two hidden layers with 512 and 128 nodes, respectively. The input and hidden layers use the rectified linear unit (ReLU) activation function, and the output layer uses the softmax activation function to yield the classification decision. To protect against overfitting, dropout with a probability of 50% was applied to both hidden layers [65]. Additionally, L2 kernel regularization (with factor $\lambda = 0.0001$) was applied to both hidden layers to protect against overfitting by adding a term to the loss function that increases with the magnitude of the network's weight vector. Figure 10 shows the architecture for this MLP classifier.

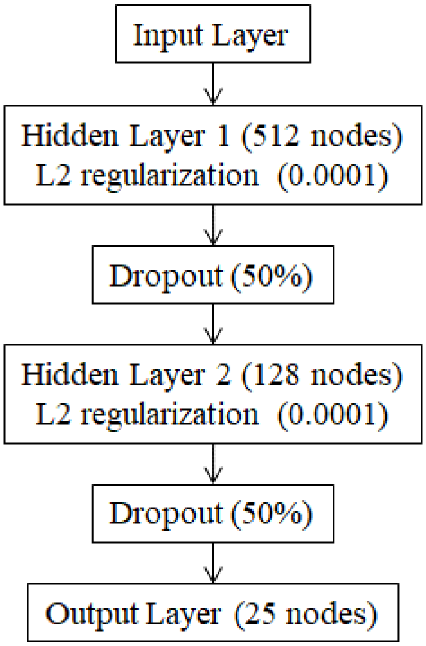

Figure 10. Architecture for the MLP classifier used for the single-band and spectral fusion studies.

4.4.2 Single-Mode Classification Study

In addition to the MLP classifier, four common machine learning classifiers – including support vector machine with a linear kernel (SVM), WKNN, linear discriminant (LD), and Gaussian Naïve Bayes (GNB) - were used to perform classification separately for each of the VNIR, fluorescence, and SWIR data. As with the first study, feature sets consisted of the k spectral samples with no further attempt at feature selection. A 4-fold cross-validation was conducted for each study as a robust estimation of multiclass classification accuracy (weighted by the number of samples per class).

SVM determines the set of maximum-margin hyperplanes to separate the classes in the feature space. WKNN, as explained above, is a variation on the k-nearest neighbors algorithm that weights the training points by the inverse square of their distances from the query point. LD classification makes simplifying assumptions about the data (i.e., Gaussian distributed with the same covariance matrix for all classes) to determine the separating hyperplanes. Finally, GNB combines the probabilities of obtaining the measured value for each input given each specific class and selects the class with the highest resulting probability. GNB assumes statistical independence between the inputs [66]. SVM was included due to its reputation as a high-performance classifier. WKNN, another robust classifier, was included for its performance and because of its use in the simulated annealing algorithm. LD was included for comparison to evaluate any performance degradation that might result from the expected violation of the Gaussian or identical covariance assumptions. GNB was included for comparison to evaluate performance degradation due to the expected violation of independence among the inputs (i.e., the selected wavelengths).

Each classifier was trained with the k = 3, 4, 5, 6, and 7 wavelengths selected by the simulated annealing algorithm for each of the three spectral modes. To place the resulting classification accuracy values in context, the results of this study were compared with benchmark classification accuracies determined using all wavelengths in the full-resolution spectra.

4.4.3 Spectral Fusion Classification Study

For this study, the wavelengths were selected for each of the three spectral modes independently, as discussed in the previous section, and then concatenated into a single vector which formed a new input layer for the MLP classifier. This classifier was then trained and evaluated (using 4-fold cross-validation) for k = 3, 4, 5, 6, and 7 wavelengths and the results were compared with a benchmark determined by including all wavelengths from the full-resolution spectra. Due to concerns about the usefulness of the SWIR data for species classification, we also evaluated fusion with just the VNIR and fluorescence modes.

4.5 FISH FILLET DATA COLLECTION

Figure 11 shows an overview of the data acquisition and processing steps for the studies represented in this paper. The database for this study consisted of VNIR and SWIR reflectance and fluorescence spectra collected from 133 fish fillets representing a total of 25 different species groups (Table 1). The species for each fillet was verified using DNA barcoding [5]. Each fillet was placed in a 150 × 100 × 25 mm sample holder created with a 3D printer (Fortus 250mc, Stratasys, Eden Prairie, MN, USA) using production-grade black thermoplastic. Image acquisition was conducted by the pushbroom method, where a linear motorized translation stage was used to move the sample holder incrementally across the scanning line of the imaging spectrograph. The length of the instantaneous field of view (IFOV) was made slightly longer than the length of the sample holder (150 mm) by adjusting the lens-to-sample distance. The resulting spatial resolution along this dimension was determined as 0.4 mm/pixel. Each fillet was sampled along the width direction (100 mm) of the holder with a step size of 0.4 mm to match the spatial resolution of the length direction [5].

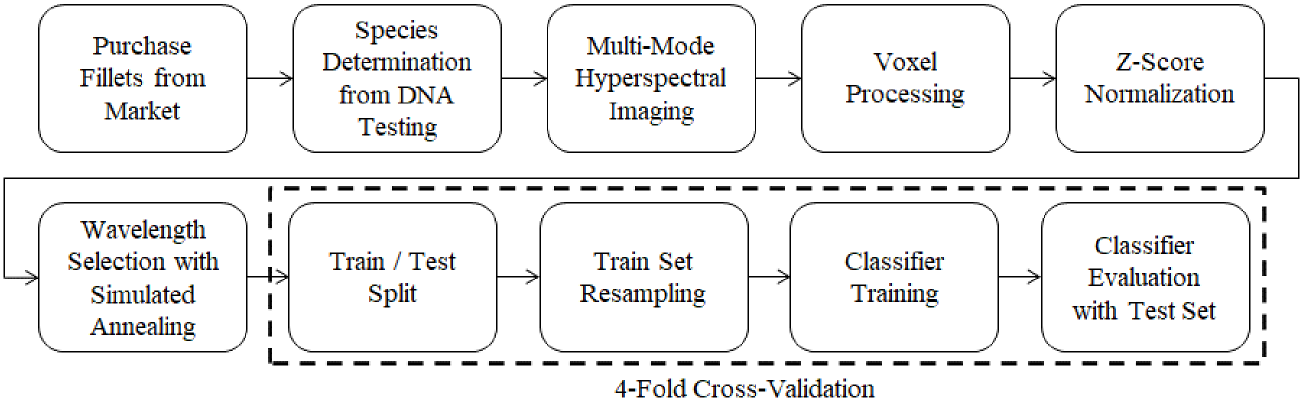

Figure 11. Overview of the data acquisition and processing flow.

Flat-field corrections were applied to the VNIR and SWIR reflectance images and the fluorescence images to convert the original absolute intensities in CCD counts to relative reflectance and fluorescence intensities [67]. An initial spatial mask was then created for each imaging mode to separate the fish fillets from the background. Outliers were handled by first calculating the mean (μ) and standard deviation (σ) of the fish pixel intensities over the entire fillet. Voxels of 10 × 10 pixels were considered to mimic independent fish fillet spectral point measurements using the field of view of a fiber optic spectrometer. Exclusion occurred if ≥10% of the constituent pixels in a voxel exceeded μ ± 2 σ to eliminate outliers. Figure 12 shows an example result of voxel processing. This approach produced a final set of spatial masks, one each for the VNIR and SWIR reflectance and fluorescence images, which determined the blocks to be used for analysis. Finally, the fluorescence spectra were scaled by a constant factor of 6,000, the approximate maximum of fluorescence spectral values in the database. This was done to set the range of fluorescence values to between zero and one. Alternative normalization methods such as z-score and area under the curve (AUC) normalization were tried as well and produced similar results. However, this simple scaling was chosen because, unlike these alternatives, it requires no knowledge of the entire spectrum and is thus consistent with the concept of collecting only a small number of wavelengths for analysis. Table 8 provides a summary of this database with the numbers of fillets per species and the number of valid voxels for each fillet and each collection mode.

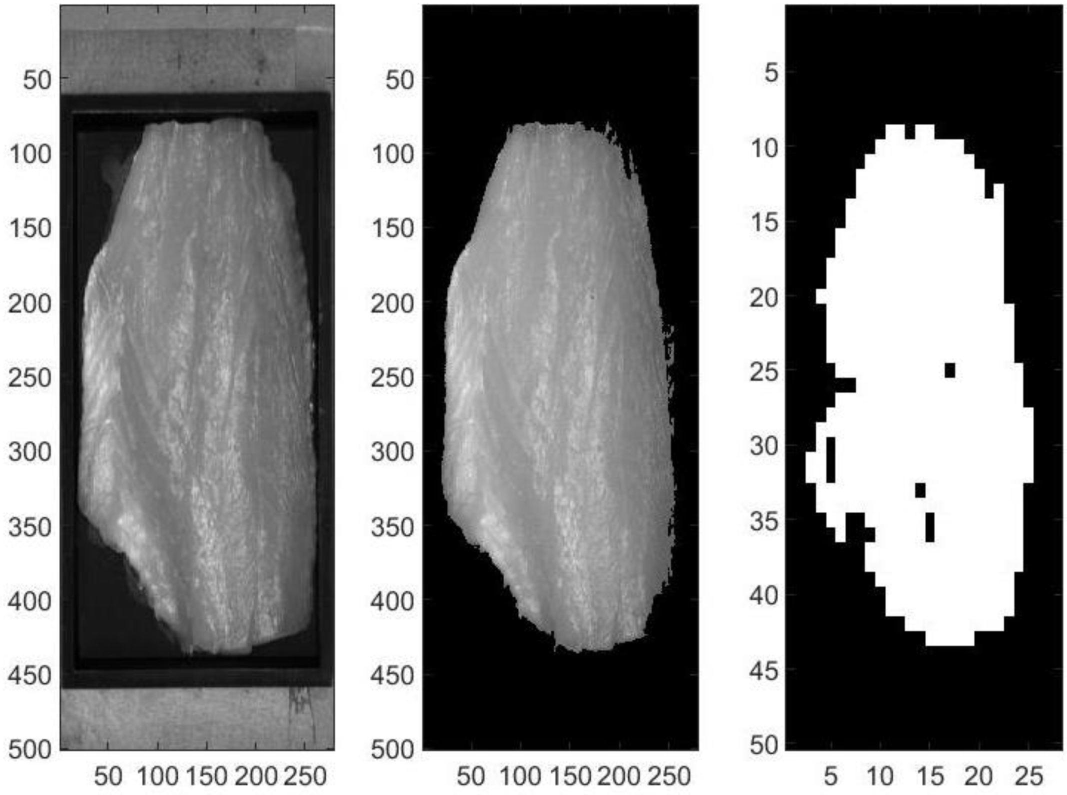

Figure 12. Example of data collection and voxel processing for a red snapper fillet. From the original VNIR image (left), a mask is applied (center) to remove the background and voxels of 10 x 10 pixels are generated (right). Valid voxels are shown in white.

Table 8. Fish fillet database summary.

Species	Number of Fillets	Number of Valid Voxels		
		VNIR	Fluorescence	SWIR
Almaco Jack (*Seriola rivoliana*)	4	1157	1169	1992
Atlantic Cod (*Gadus morhua*)	4	1322	1391	1508
Bigeye Tuna (*Thunnus obesus*)	4	831	572	2416

California Flounder (*Paralichthys californicus*)	4	1016	1113	2416
Char (*Salvelinus* sp.)	4	1165	1156	1508
Chinook Salmon (*Oncorhynchus tshawytscha*)	4	1630	1570	2416
Cobia (*Rachycentron canadum*)	4	1235	1170	1508
Coho Salmon (*Oncorhynchus kisutch*)	4	894	887	2416
Gilthead Bream (*Sparus aurata*)	4	1314	1275	1362
Goosefish (*Lophiidae* sp.)	4	1304	1356	1508
Haddock (*Melanogrammus aeglefinus*)	4	1193	1375	1508
Malabar Blood Snapper (*Lutjanus malabaricus*)	12	5530	4750	7248
Opah (*Lampris* sp.)	4	913	875	2416
Pacific Halibut (*Hippoglossus stenolepis*)	4	1943	2120	2416
Pacific Cod (*Gadus macrocephalus*)	4	1619	1723	2416
Petrale Sole (*Eopsetta jordani*)	6	2253	2427	3624
Rainbow Trout (*Oncorhynchus mykiss*)	11	4263	3606	4806
Red Snapper (*Lutjanus campechanus*)	18	9482	7351	10872
Rockfish (*Sebastes* sp.)	4	1230	1310	2416
Sablefish (*Anoplopoma fimbria*)	4	954	963	2416
Sockeye Salmon (*Oncorhynchus nerka*)	4	1033	909	2416
Swordfish (*Xiphias gladius*)	4	789	786	2416
Tuna (*Thunnus* sp.)	6	1473	1314	3170
Winter Skate (*Leucoraja ocellata*)	4	1839	1815	1860
Yelloweye Rockfish (*Sebastes ruberrimus*)	4	1197	1216	2416

The reflectance and scaled fluorescence spectra for each of the 25 fish species are shown in Figure 13. The significant differences in the shapes and positions of the spectral averages for the various species and the homogeneous nature of the spectra (as indicated by the relatively short error bars) suggest that high classification accuracies can be achieved with this spectral information.

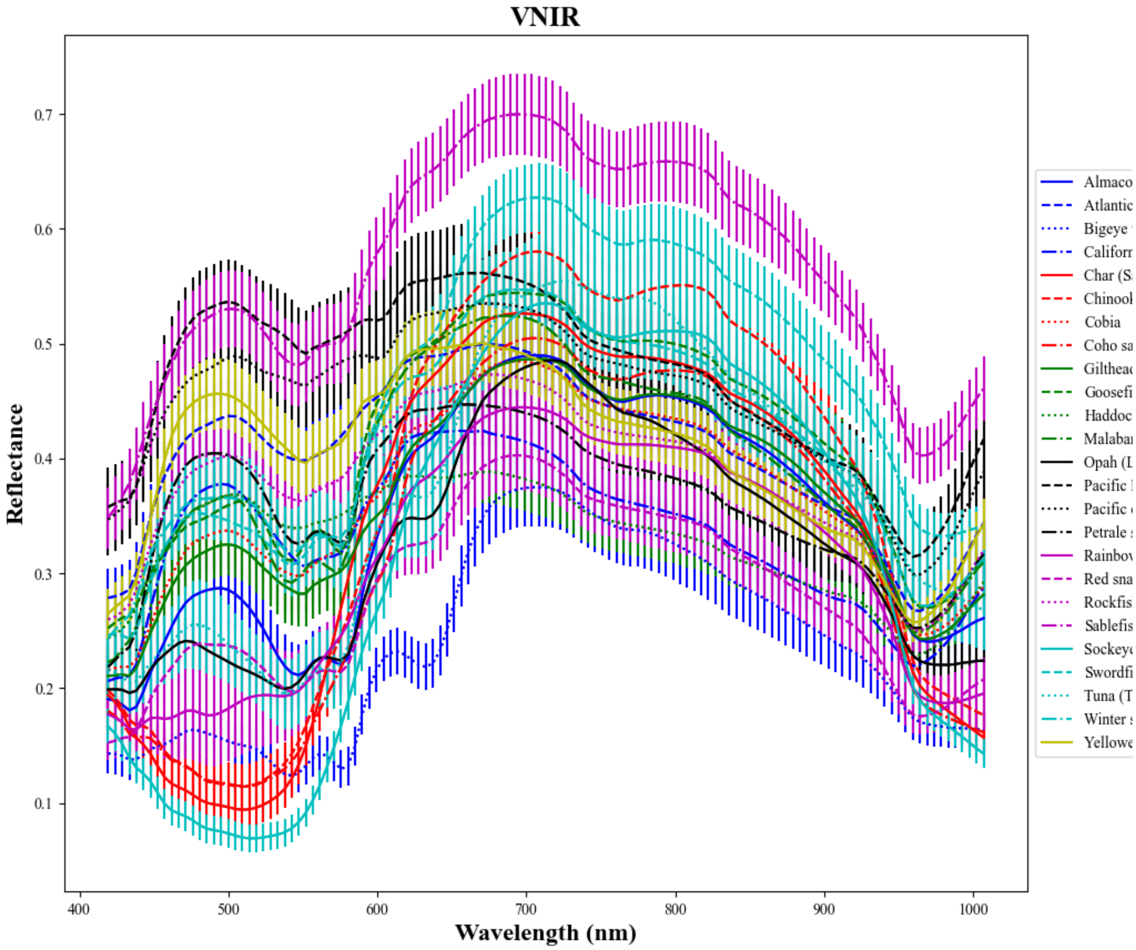
VNIR
Reflectance
0.1
0.2
0.3
0.4
0.5
0.6
0.7
Wavelength (nm)
400
500
600
700
800
900
1000
Almaco
Atlantic
Bigeye
Califorr
Char (S
Chinool
Cobia
Coho sa
Gilthea
Goosefi
Haddoc
Malabar
Opah (I
Pacific
Pacific
Petrale
Rainbov
Red sna
Rockfis
Sablefis
Sockeye
Swordfi
Tuna (T
Winter
Yellowe

(a)

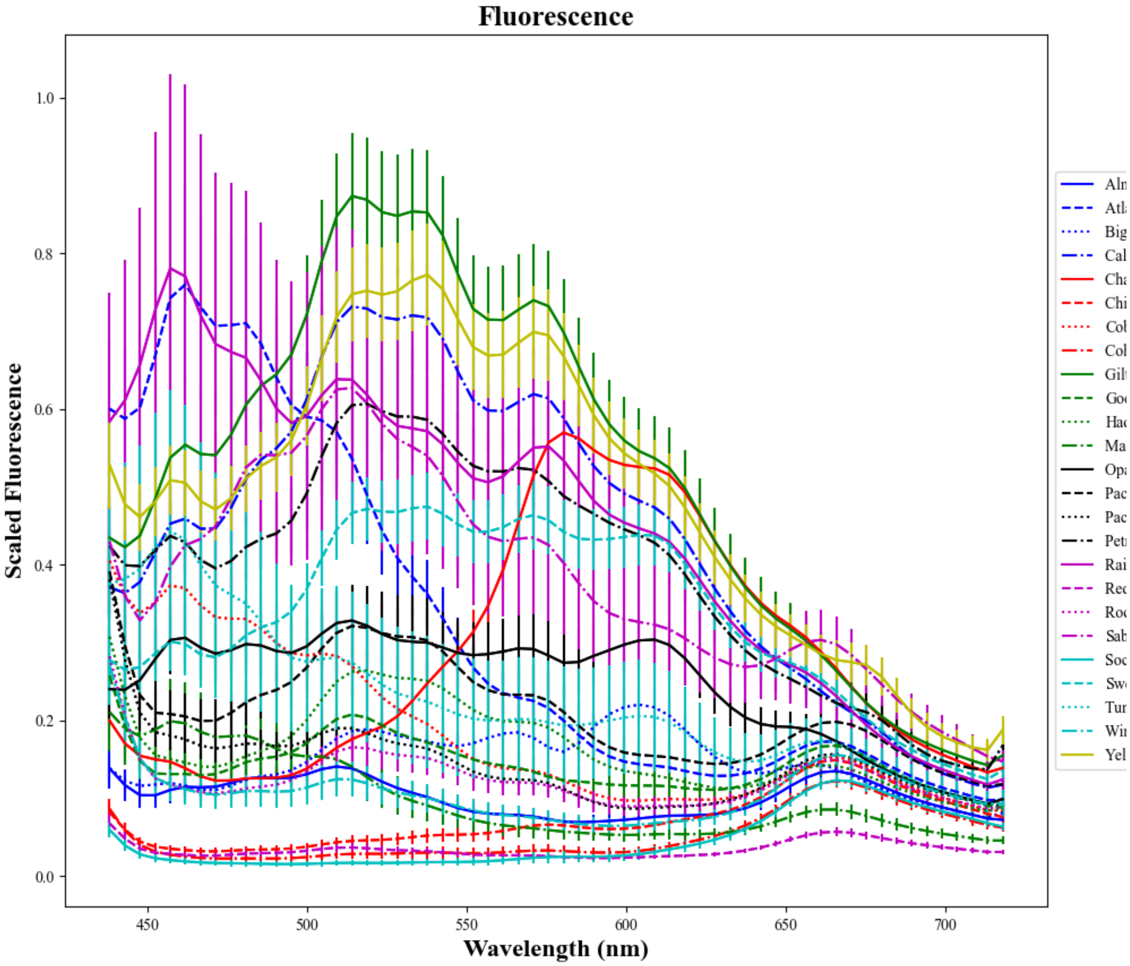
Fluorescence
Scaled Fluorescence
Wavelength (nm)
0.0
0.2
0.4
0.6
0.8
1.0
450
500
550
600
650
700
Alı
Atl
Big
Cal
Cha
Chi
Col
Col
Gilt
Goo
Had
Ma
Opa
Pac
Pac
Pet
Rai
Rec
Roc
Sab
Soc
Swe
Tur
Win
Yel

(b)

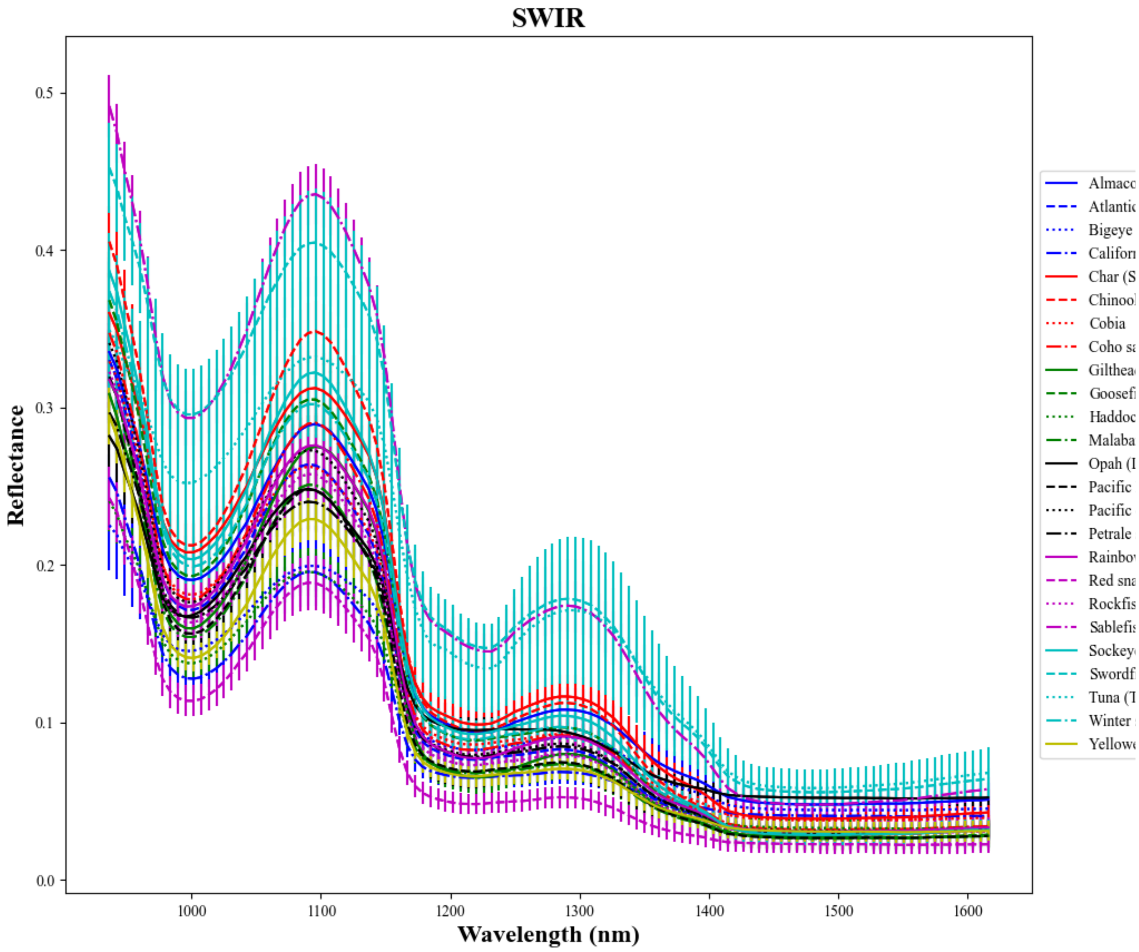

(c)

Figure 13. Average spectra for each of the 25 fish species. (a) VNIR reflectance; (b) scaled fluorescence; (c) SWIR reflectance. Error bars correspond to half of a standard deviation over all voxels for each species.

4.5.1 Cross-Validation Train and Test Datasets

For both the single-mode and the spectral fusion studies, 4-fold cross-validation was conducted by dividing the complete dataset (as described in Table 8) into four disjoint test sets, each of which contained voxels from at least one fillet of each of the 25 species. The corresponding training set for each test set was then composed of all data not in the test set. Four-fold cross-validation (as opposed to the more common 5- or 10-fold versions) was chosen because there was greater variability between fillets of the same species than between voxels of the same fillet. Thus, we wanted to ensure that each test set contained entire fillets that were not included in the corresponding training set. For those species with more than four fillets in the complete dataset (e.g., Malabar blood snapper), the fillets were divided into the four test sets with the goal of having the total number of fillets in each test set as equal as possible.

4.5.2 Data Imbalance Correction

To prevent classification biases due to data imbalances between the various species, we applied sampling with replacement to each training set to produce 8,000 voxel samples per species for a total of 200,000 samples in each training set. No resampling was applied to the test sets, but the measured multiclass classification accuracies were weighted by the number of voxel samples per class to ensure an equal contribution from each species.

4.6 RESULTS AND DISCUSSION

4.6.1 Wavelength Selection

The robustness of the proposed simulated annealing approach was evaluated by running 10 iterations of the algorithm with the VNIR data for the $k = 7$ cases and examining the variation in the resulting selected wavelengths and the associated WKNN classification accuracies. Figure 14(a) shows the wavelengths selected for each of the 10 iterations, with each row of similarly colored dots representing a single iteration. Although some variability in the selected wavelengths is noticeable, the plot of multiclass classification accuracies for these iterations in Figure 14(b) shows little variability in the resulting accuracy. The standard deviation over these 10 accuracy values was 0.13%.

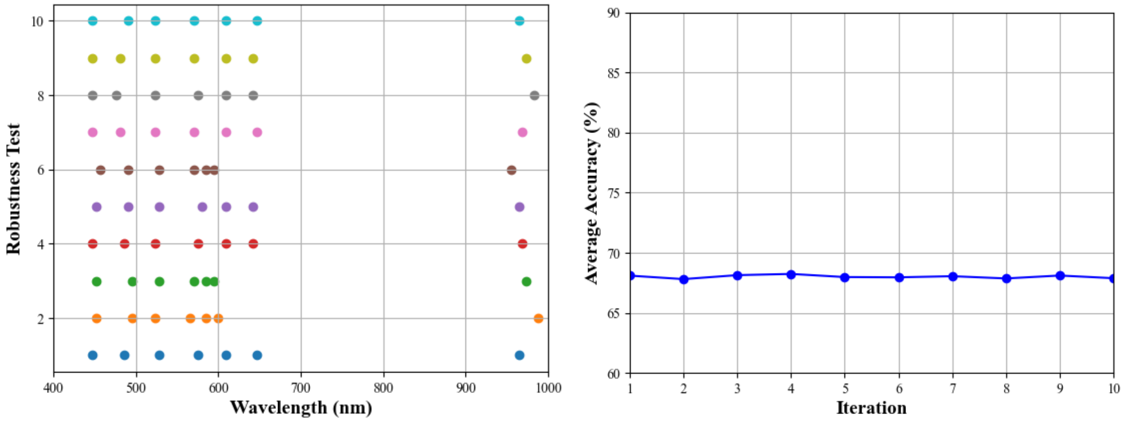

(a) (b)

Figure 14. Results of the wavelength selection robustness study. (a) Scatter plot showing selected wavelengths for 10 iterations of the k = 7 VNIR study. (b) Plot of final accuracies for each of the 10 iterations.

Figure 15 shows the average VNIR reflectance spectrum for a red snapper fillet with the *k* = 3, 4, 5, 6, and 7 optimal wavelengths selected by the simulated annealing algorithm. For all *k* values, the selected wavelengths correspond to interesting peaks, valleys, and inflection points of the spectrum. Clearly, the region of wavelengths < 600 nm is favored along with the trough near 950 nm.

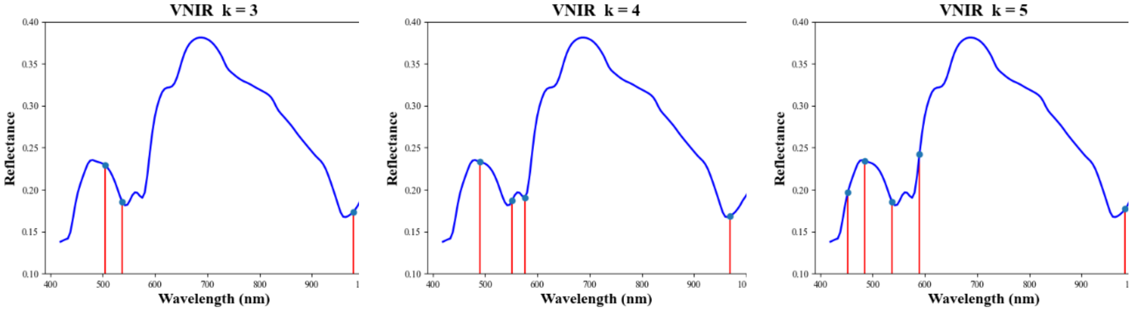

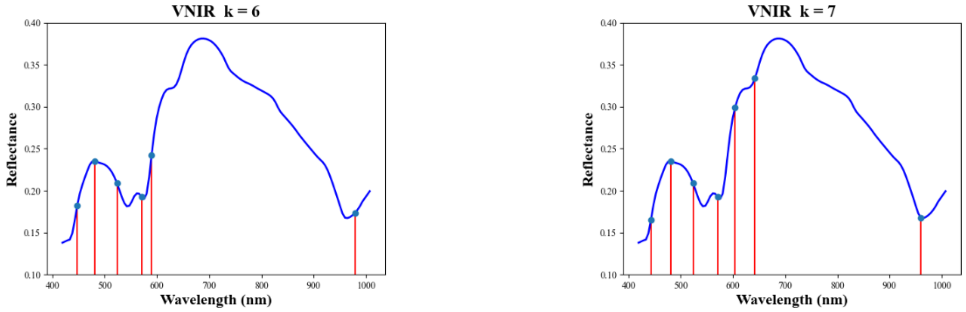

Figure 15. Average VNIR reflectance spectrum for one of the red snapper fillets with the optimal k = 3, 4, 5, 6, 7 wavelength selections.

The wavelength selections for the fluorescence data in relation to the average spectrum for one of the red snapper fillets are shown in Figure 16. For this mode, the initial wavelength selections are concentrated at the minima of the spectrum with no wavelengths near the large peak around 670 nm selected until the *k* = 6 case.

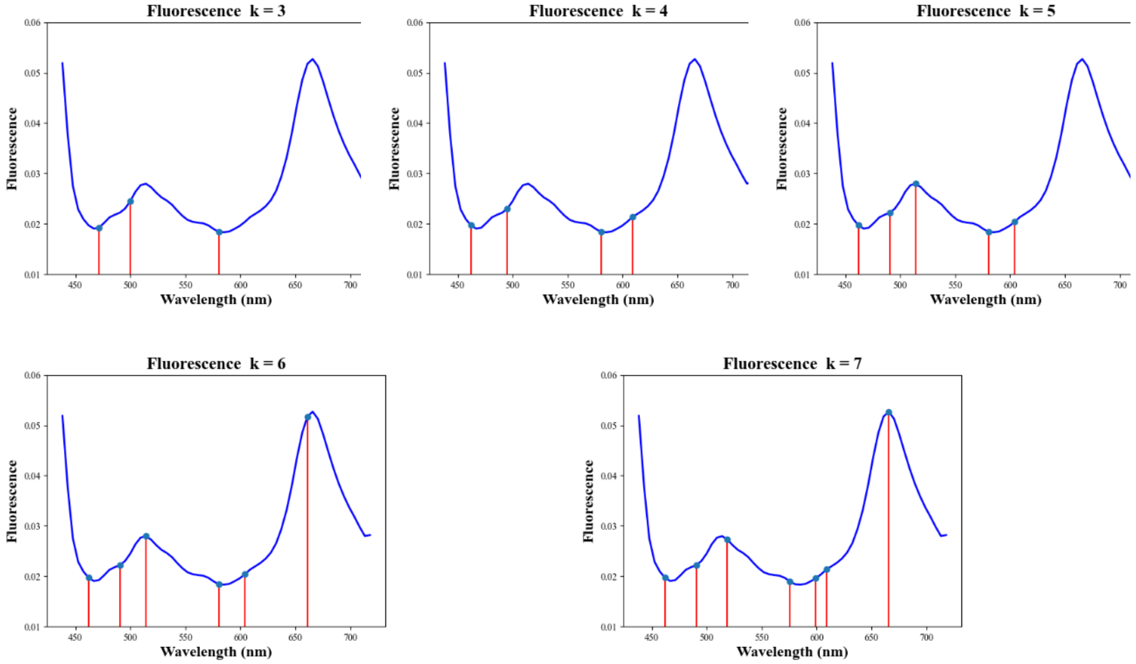

Figure 16. Average fluorescence spectrum for one of the red snapper fillets with the optimal k = 3, 4, 5, 6, 7 wavelength selections.

Figure 17 shows the wavelength selections for the SWIR reflectance data. The selections for each of the *k* values are concentrated near the trough around 1000 nm and the inflection point near 1160 nm. No wavelengths above 1200 nm are selected.

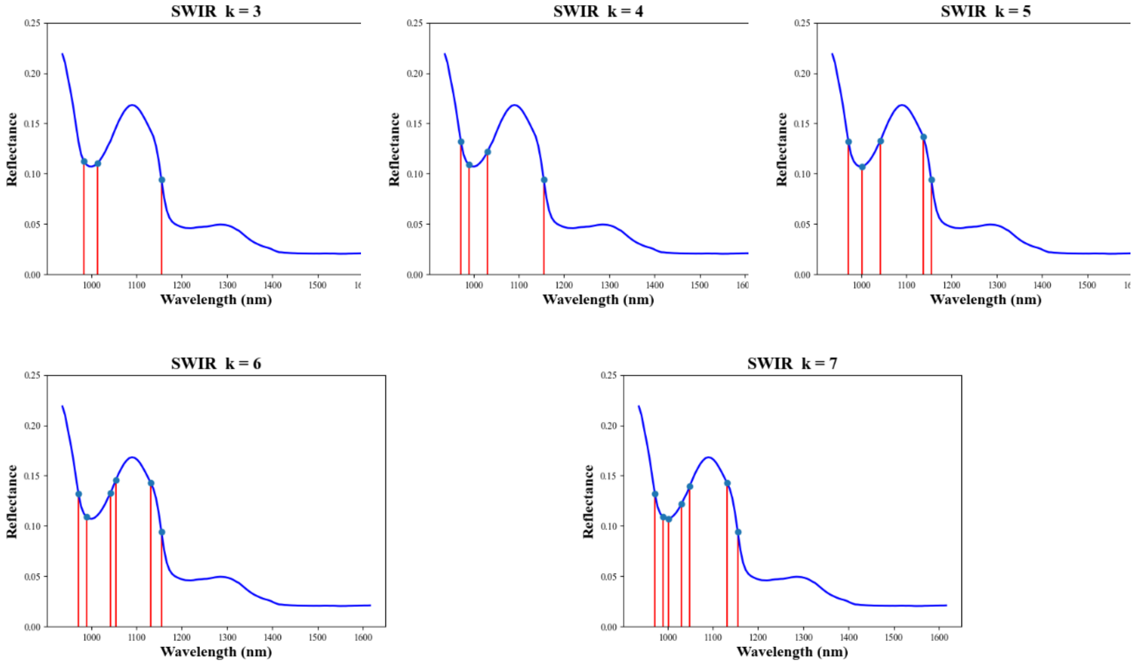

Figure 17. Average SWIR reflectance spectrum for one of the red snapper fillets with the optimal k = 3, 4, 5, 6, 7 wavelength selections.

4.6.2 Classification

4.6.2.1 Results of the Single-Mode Study

Average cross-validated (4-fold) classification accuracies for the VNIR reflectance data are given in Table 9. The column labeled “Benchmark” gives the results for the case where all wavelengths are included. The set of columns under “Selected Wavelengths” list the resulting accuracies based on the spectral values at the *k* = 3, 4, 5, 6, 7 optimal wavelengths. Results for the fluorescence data are provided in a similar manner in Table 10 and for the SWIR reflectance data in

Table **11**. Values in bold denote the highest accuracy for each number of selected wavelengths.

Table 9. Single-mode classification accuracies (4-fold cross-validation) for the VNIR reflectance data.

	Benchmark	**Selected Wavelengths**				
	All Wavelengths	***k = 3***	***k = 4***	***k = 5***	***k = 6***	***k = 7***
MLP	87.7%	50.4%	**60.1%**	**72.7%**	**79.7%**	**82.7%**
SVM	89.8%	**50.6%**	59.9%	68.7%	74.5%	77.6%

WKNN	69.8%	45.6%	56.0%	61.7%	65.1%	67.4%
LD	**91.7%**	45.0%	51.2%	54.6%	58.4%	61.3%
GNB	33.1%	26.8%	31.2%	27.3%	28.6%	31.7%

Table 10. Single-mode classification accuracies (4-fold cross-validation) for the fluorescence data.

	Benchmark	**Selected Wavelengths**				
	All Wavelengths	***k* = 3**	***k* = 4**	***k* = 5**	***k* = 6**	***k* = 7**
MLP	**92.9%**	**78.9%**	**84.3%**	**86.2%**	**89.4%**	**89.9%**
SVM	82.5%	66.7%	71.7%	70.8%	79.5%	79.5%
WKNN	79.2%	71.1%	75.2%	77.3%	77.1%	77.3%
LD	84.1%	59.0%	62.2%	65.4%	65.5%	68.5%
GNB	51.0%	40.2%	45.2%	44.0%	49.0%	49.0%

Table 11. Single-mode classification accuracies (4-fold cross-validation) for the SWIR data.

	Benchmark	**Selected Wavelengths**				
	All Wavelengths	***k* = 3**	***k* = 4**	***k* = 5**	***k* = 6**	***k* = 7**
MLP	75.8%	**46.1%**	**56.1%**	**66.4%**	**67.7%**	**67.6%**
SVM	63.2%	44.5%	53.0%	62.1%	64.2%	64.1%
WKNN	41.0%	38.7%	46.3%	50.9%	52.1%	52.6%
LD	**80.7%**	38.2%	45.2%	51.1%	53.3%	54.5%
GNB	20.3%	14.4%	14.5%	14.8%	14.7%	14.6%

Looking first at the accuracies for the benchmark cases, MLP yields the highest accuracy for the fluorescence data but comes in second for the SWIR data and third for the VNIR data. The superior performance of LD, a relatively simple classifier, for the VNIR and SWIR benchmark cases suggests that overfitting is a significant problem for these cases. Accuracies for the SWIR data are far lower, with LD yielding the highest accuracy at just 80.65%. GNB yields the lowest accuracies for all three modes, reinforcing the notion that classification performance is not dependent upon the values from the selected wavelengths themselves but upon their values in relation to one another. The independence assumption of GNB results in low performance.

Looking next at the “Selected Wavelengths” cases, MLP outperforms the other classifiers for all *k* values and spectral modes (except for the *k* = 3 case with the VNIR data). Accuracies >85% are possible given spectral values at just seven or fewer wavelengths for the fluorescence data and >80% for the VNIR reflectance data. Most importantly, with MLP trained on only seven spectral values, the resulting accuracies are within 10 percentage points of the benchmark case for all three spectral modes. The highest performance (89.91%) is seen for the fluorescence data.

Figure 18, Figure 19, and Figure 20 show confusion matrices for the $k = 7$ MLP results from the single-mode VNIR, fluorescence, and SWIR data, respectively. The classification performance is clearly best with the fluorescence data with accuracies > 95% for many species. However, the accuracies for some other species are much lower. For example, goosefish has the lowest accuracy at 62.5%, being misclassified as rockfish 28.2% of the time. This is an indication that nearly an entire goosefish fillet was misclassified as rockfish in one of the folds. The overall classification performance is a little lower with the VNIR data. Winter skate shows the lowest classification accuracy at 39.4% in this case, being misclassified as goosefish 26.0% of the time and as almaco jack 13.0% of the time. Much worse performance is seen with the SWIR data where we find a larger variety of misclassifications. Rockfish has the lowest classification accuracy at just 15.7% with high percentages of misclassification (> 14%) as Atlantic cod, haddock, Pacific halibut, and Pacific cod.

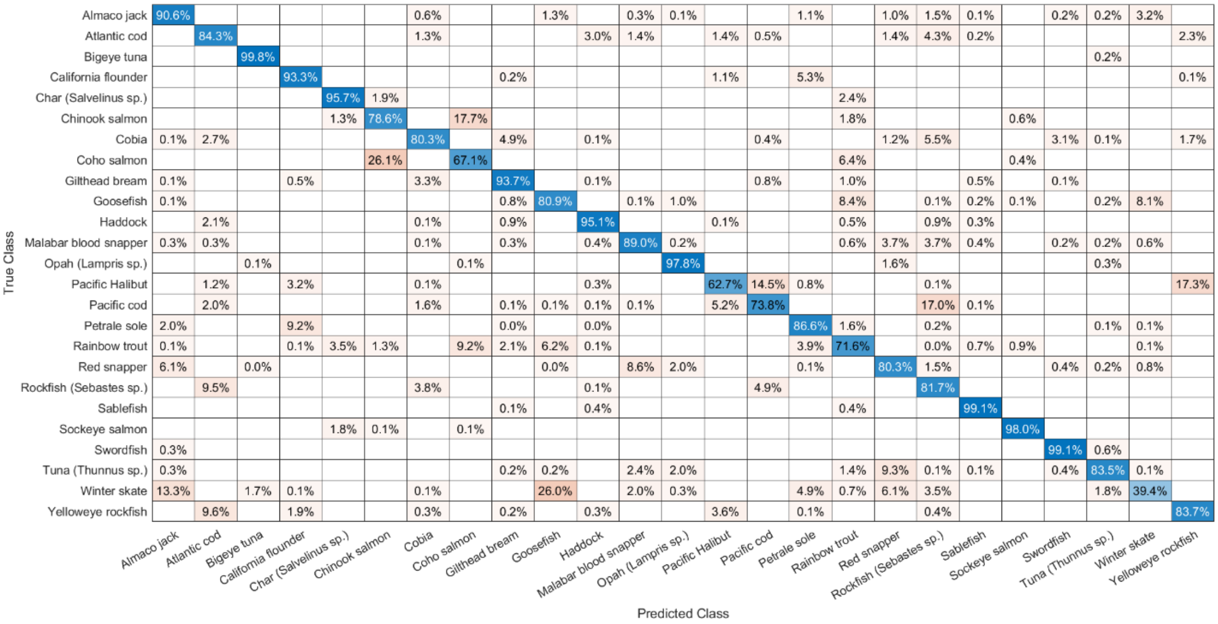

Figure 18. Confusion matrix for the single-mode VNIR results with the k = 7 MLP (overall classification accuracy = 82.7%).

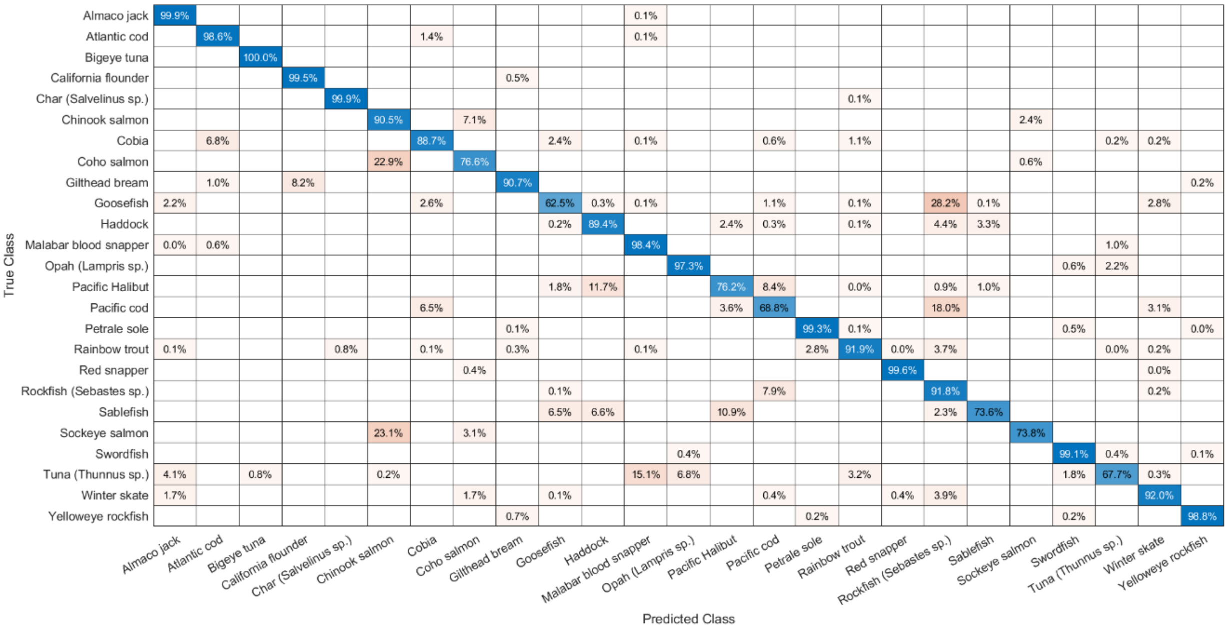

Figure 19. Confusion matrix for the single-mode fluorescence results with the k = 7 MLP (overall classification accuracy = 89.9%).

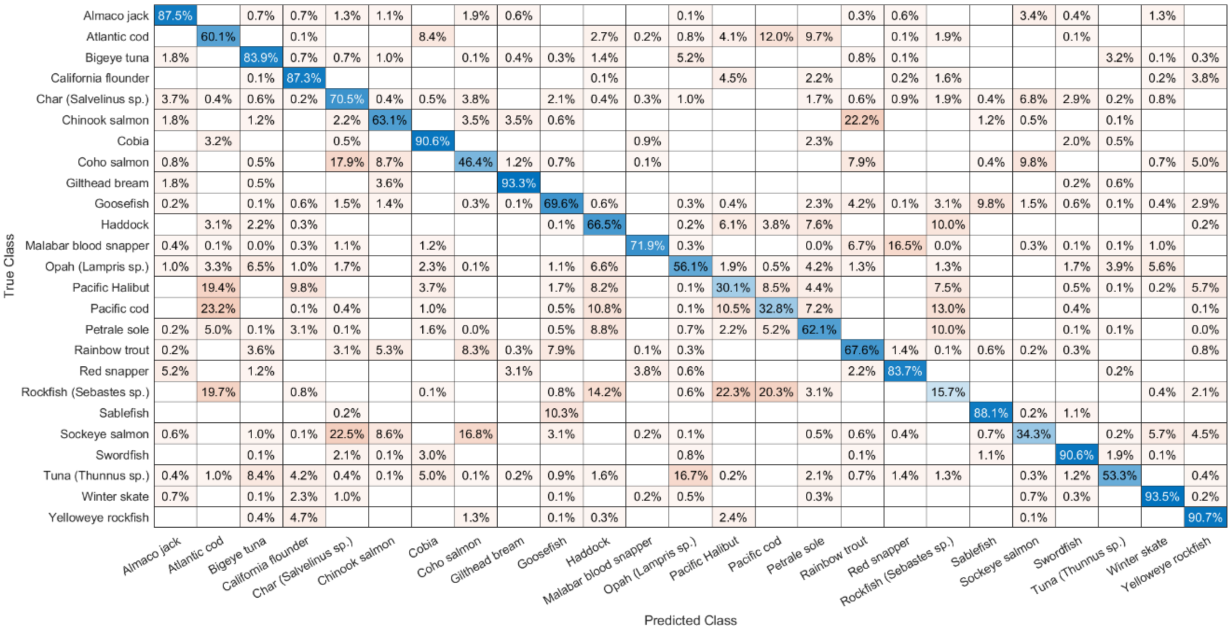

	Almaco jack	Atlantic cod	Bigeye tuna	California flounder	Char (Salvelinus sp.)	Chinook salmon	Cobia	Coho salmon	Gilthead bream	Goosefish	Haddock	Malabar blood snapper	Opah (Lampris sp.)	Pacific Halibut	Pacific cod	Petrale sole	Rainbow trout	Red snapper	Rockfish (Sebastes sp.)	Sablefish	Sockeye salmon	Swordfish	Tuna (Thunnus sp.)	Winter skate	Yelloweye rockfish
Almaco jack	87.5%		0.7%	0.7%	1.3%	1.1%		1.9%	0.6%				0.1%				0.3%	0.6%			3.4%	0.4%		1.3%	
Atlantic cod		60.1%		0.1%			8.4%				2.7%	0.2%	0.8%	4.1%	12.0%	9.7%		0.1%	1.9%			0.1%			
Bigeye tuna	1.8%		83.9%	0.7%	0.7%	1.0%		0.1%	0.4%	0.3%	1.4%		5.2%				0.8%	0.1%					3.2%	0.1%	0.3%
California flounder			0.1%	87.3%							0.1%			4.5%		2.2%		0.2%	1.6%					0.2%	3.8%
Char (Salvelinus sp.)	3.7%	0.4%	0.6%	0.2%	70.5%	0.4%	0.5%	3.8%		2.1%	0.4%	0.3%	1.0%			1.7%	0.6%	0.9%	1.9%	0.4%	6.8%	2.9%	0.2%	0.8%	
Chinook salmon	1.8%		1.2%		2.2%	63.1%		3.5%	3.5%	0.6%							22.2%			1.2%	0.5%		0.1%		
Cobia		3.2%			0.5%		90.6%					0.9%				2.3%						2.0%	0.5%		
Coho salmon	0.8%		0.5%		17.9%	8.7%		46.4%	1.2%	0.7%		0.1%					7.9%			0.4%	9.8%			0.7%	5.0%
Gilthead bream	1.8%		0.5%			3.6%			93.3%													0.2%	0.6%		
Goosefish	0.2%		0.1%	0.6%	1.5%	1.4%		0.3%	0.1%	69.6%	0.6%		0.3%	0.4%		2.3%	4.2%	0.1%	3.1%	9.8%	1.5%	0.6%	0.1%	0.4%	2.9%
Haddock		3.1%	2.2%	0.3%						0.1%	66.5%		0.2%	6.1%	3.8%	7.6%			10.0%						0.2%
Malabar blood snapper	0.4%	0.1%	0.0%	0.3%	1.1%		1.2%					71.9%	0.3%			0.0%	6.7%	16.5%	0.0%		0.3%	0.1%	0.1%	1.0%	
Opah (Lampris sp.)	1.0%	3.3%	6.5%	1.0%	1.7%		2.3%	0.1%		1.1%	6.6%		56.1%	1.9%	0.5%	4.2%	1.3%		1.3%			1.7%	3.9%	5.6%	
Pacific Halibut		19.4%		9.8%			3.7%			1.7%	8.2%		0.1%	30.1%	8.5%	4.4%			7.5%			0.5%	0.1%	0.2%	5.7%
Pacific cod		23.2%		0.1%	0.4%		1.0%			0.5%	10.8%		0.1%	10.5%	32.8%	7.2%			13.0%			0.4%			0.1%
Petrale sole	0.2%	5.0%	0.1%	3.1%	0.1%		1.6%	0.0%		0.5%	8.8%		0.7%	2.2%	5.2%	62.1%			10.0%			0.1%	0.1%		0.0%
Rainbow trout	0.2%		3.6%		3.1%	5.3%		8.3%	0.3%	7.9%		0.1%	0.3%				67.6%	1.4%	0.1%	0.6%	0.2%	0.3%			0.8%
Red snapper	5.2%		1.2%						3.1%			3.8%	0.6%				2.2%	83.7%					0.2%		
Rockfish (Sebastes sp.)		19.7%		0.8%			0.1%			0.8%	14.2%		0.6%	22.3%	20.3%	3.1%			15.7%					0.4%	2.1%
Sablefish					0.2%					10.3%										88.1%	0.2%	1.1%			
Sockeye salmon	0.6%		1.0%	0.1%	22.5%	8.6%		16.8%		3.1%		0.2%	0.1%			0.5%	0.6%	0.4%		0.7%	34.3%		0.2%	5.7%	4.5%
Swordfish			0.1%		2.1%	0.1%	3.0%						0.8%				0.1%			1.1%		90.6%	1.9%	0.1%	
Tuna (Thunnus sp.)	0.4%	1.0%	8.4%	4.2%	0.4%	0.1%	5.0%	0.1%	0.2%	0.9%	1.6%		16.7%	0.2%		2.1%	0.7%	1.4%	1.3%		0.3%	1.2%	53.3%		0.4%
Winter skate	0.7%		0.1%	2.3%	1.0%					0.1%		0.2%	0.5%			0.3%					0.7%	0.3%		93.5%	0.2%
Yelloweye rockfish			0.4%	4.7%				1.3%		0.1%	0.3%			2.4%							0.1%				90.7%

Figure 20. Confusion matrix for the single-mode SWIR results with the k = 7 MLP (overall classification accuracy = 67.6%).

The variability of these single-mode classification results with each of the four cross-validation folds can be seen in Figure 21. The lower and upper limits of the error bars in each plot represent the minimum and maximum accuracies, respectively, for the four-folds. The red dashed line in each plot represents the benchmark accuracy obtained by MLP using all wavelengths in the spectrum.

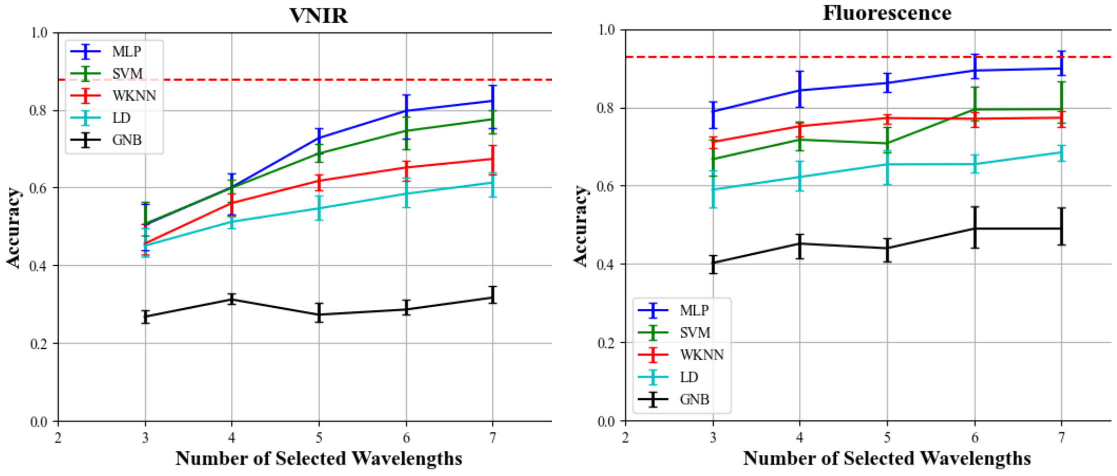

(a) (b)

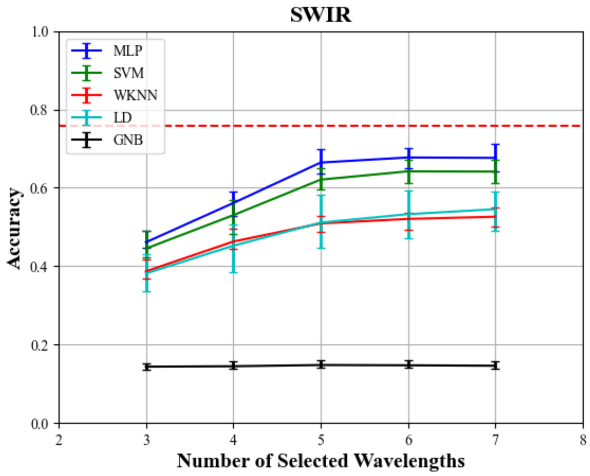

(c)

Figure 21. Plot of 4-fold cross-validation accuracies for each of the five classifiers as a function of the number of selected wavelengths in the single-mode classification study for (a) VNIR, (b) fluorescence, and (c) SWIR data. The red dashed line in each plot marks the benchmark accuracy obtained by MLP using all wavelength in the spectrum. Error bars mark the range of accuracies for the four folds.

The results of the single-mode classification study prove that high accuracies can be obtained (especially with the MLP classifier) with just seven or fewer wavelengths. The best benchmark performance (92.9%) using all wavelengths was seen with the fluorescence mode with MLP followed by VNIR reflectance (91.7%) and then SWIR reflectance (80.7%), both with LD. The superior performance of LD in these cases suggests the inclusion of all wavelengths significantly increases the potential for overfitting. With seven wavelengths in the fluorescence case, the MLP accuracy came within ~3% of the benchmark accuracy. Review of the confusion matrices from this study reveal that although high overall accuracies can result from these single-mode classifications, each spectroscopic mode has its own unique set of strengths and weaknesses. Furthermore, highly concentrated misclassification results were seen in a few cases, suggesting that entire fillets in the test sets were sometimes misclassified. This is likely a consequence of the somewhat small size of our current dataset. We believe these misclassifications can be alleviated in future studies as we increase the number of fillets per species to better represent the within-species variability of the spectra.

4.6.2.2 Results of the Fusion Classification Study

Table 12 gives the resulting average 4-fold cross-validation accuracies for the MLP classifier with the spectral modes fused at the input layer. As with the single-mode study, the value in the “Benchmark” column is the accuracy obtained by fusing all wavelengths from the various modes. We present results from the fusion of all three modes as well as results of fusion without the SWIR mode. This latter iteration was included due to the poor performance with the SWIR data in the single-mode study. By fusing the modes, MLP is able to produce classification accuracies that exceed the highest accuracies from the single-mode study by > 10% for $k = 3$ and by > 4% at $k = 7$. An accuracy of > 90% is obtained even with only three wavelengths. The fusion accuracies with all three spectral modes exceed the accuracies without the SWIR data only by 1-2 percentage points for the $k = 3, 4, 5, 6, 7$ cases (and is lower for the benchmark case), indicating that SWIR, in fact, does not contribute independent information for species classification. Figure 22 shows the confusion matrix for the fusion of all three modes with $k = 7$. Note that although the rates of correct classification are > 99% for many species and > 90% for 20 species, the large, concentrated misclassification errors seen in the single-mode study were found here as well. Tuna has the lowest classification accuracy at 61.80%, with 27.8% of the misclassifications as Malabar blood snapper. In this case, less than 8% of the voxels from the two tuna fillets in one of the test sets were classified correctly.

Table 12. Resulting average 4-fold cross-validation accuracies for the fusion of spectral modes in the input layer of the MLP classifier. The values in the "Benchmark" column refer to accuracies obtained using all wavelengths in each spectral mode.

Fusion	Benchmark	$k = 3$	$k = 4$	$k = 5$	$k = 6$	$k = 7$
VNIR-Fluor-SWIR	94.9%	90.4%	92.3%	93.8%	94.8%	94.5%
VNIR-Fluor	95.5%	88.9%	90.2%	92.4%	94.7%	94.0%

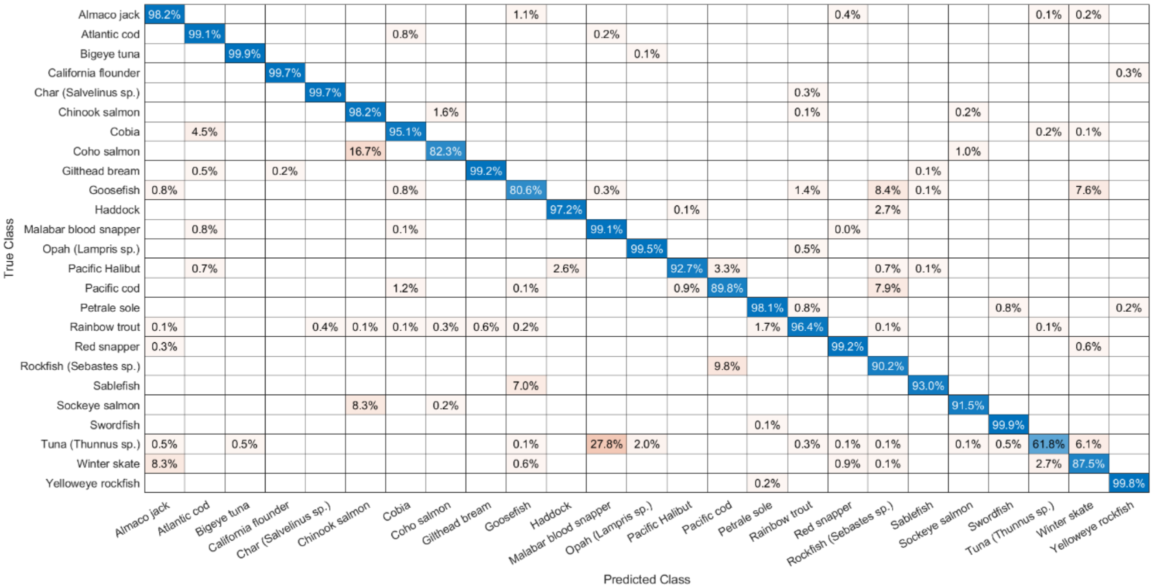

	Almaco jack	Atlantic cod	Bigeye tuna	California flounder	Char (Salvelinus sp.)	Chinook salmon	Cobia	Coho salmon	Gilthead bream	Goosefish	Haddock	Malabar blood snapper	Opah (Lampris sp.)	Pacific Halibut	Pacific cod	Petrale sole	Rainbow trout	Red snapper	Rockfish (Sebastes sp.)	Sablefish	Sockeye salmon	Swordfish	Tuna (Thunnus sp.)	Winter skate	Yelloweye rockfish
Almaco jack	98.2%									1.1%								0.4%					0.1%	0.2%	
Atlantic cod		99.1%					0.8%					0.2%													
Bigeye tuna			99.9%										0.1%												
California flounder				99.7%																					0.3%
Char (Salvelinus sp.)					99.7%												0.3%								
Chinook salmon						98.2%		1.6%									0.1%				0.2%				
Cobia		4.5%					95.1%																0.2%	0.1%	
Coho salmon						16.7%		82.3%													1.0%				
Gilthead bream		0.5%		0.2%					99.2%											0.1%					
Goosefish	0.8%						0.8%			80.6%		0.3%					1.4%		8.4%	0.1%				7.6%	
Haddock											97.2%			0.1%					2.7%						
Malabar blood snapper		0.8%					0.1%					99.1%						0.0%							
Opah (Lampris sp.)													99.5%				0.5%								
Pacific Halibut		0.7%									2.6%			92.7%	3.3%				0.7%	0.1%					
Pacific cod							1.2%			0.1%				0.9%	89.8%				7.9%						
Petrale sole																98.1%	0.8%					0.8%			0.2%
Rainbow trout	0.1%				0.4%	0.1%	0.1%	0.3%	0.6%	0.2%						1.7%	96.4%		0.1%				0.1%		
Red snapper	0.3%																	99.2%						0.6%	
Rockfish (Sebastes sp.)															9.8%				90.2%						
Sablefish										7.0%										93.0%					
Sockeye salmon						8.3%		0.2%													91.5%				
Swordfish																0.1%						99.9%			
Tuna (Thunnus sp.)	0.5%		0.5%							0.1%		27.8%	2.0%				0.3%	0.1%	0.1%		0.1%	0.5%	61.8%	6.1%	
Winter skate	8.3%									0.6%								0.9%	0.1%				2.7%	87.5%	
Yelloweye rockfish																0.2%									99.8%

Figure 22. Confusion matrix for the fusion of all three spectral modes with k = 7 selected wavelengths (overall classification accuracy = 94.5%).

These results support the hypothesis that individual strengths of different spectroscopic modes can be combined to form a classifier with superior accuracy. Stated another way, the failure modes of each spectroscopic mode can be mitigated by the other two modes to significantly reduce all misclassification rates. Furthermore, Table 12 and Figure 22 reveal that significant improvements in accuracy are possible even with just three selected wavelengths from each mode.

4.7 CONCLUSIONS

This effort was designed to evaluate the potential of a new methodology for selecting narrowband wavelengths from multiple spectroscopic modes and combining the spectral values at these wavelengths to enable the accurate classification of materials under investigation. The simulated annealing algorithm was found to robustly produce optimal sets of k wavelengths for k = 3, 4, 5, 6, 7. The results of the two classification studies confirm proof of concept for the proposed methodology to support the design of inexpensive hyperspectral imaging devices to classify fish species featuring homogenous spectral data.

CHAPTER 5. SIMULATED ANNEALING-BASED WAVELENGTH SELECTION FOR ROBUST TISSUE OXYGENATION ESTIMATION POWERED BY THE EXTENDED MOD-IFIED LAMBERT-BEER LAW

5.1 INTRODUCTION

In this chapter, we shift to a different application for hyperspectral wavelength selection: SO_2 estimation for wound monitoring. A slightly modified version of the simulated annealing algorithm from Chapter 4 is used, but it is paired with a different cost function built around the Extended Modified Lambert-Beer law (EMLB), an SO_2 estimation method introduced by Huong et al. [68] which has been proven effective in diabetic wound monitoring [69] and robust to differences in melanin concentration. We re-introduce the EMLB and provide additional details on its implementation. The EMLB is applied with different numbers of selected wavelengths and SO_2 estimation accuracy is evaluated with validation datasets consisting of visible band Monte Carlo simulation spectra representing light to dark skin types and *in vivo* spectra collected during an occlusion study from 13 Asian volunteers. To simulate the properties of a collection device designed with inexpensive LEDs and/or filters, these evaluations are repeated with the same data convolved with a 15 nm full-width half maximum (FWHM) Gaussian filter. Furthermore, a stability test is performed to determine the variation in prediction accuracy that might be experienced should the peak wavelengths of the LEDs/filters not match the selected wavelengths, either due to manufacturing tolerances, temperature fluctuations, or other phenomena.

5.2 MATERIALS AND METHODS

5.2.1. Extended Modified Lambert-Beer Law

The Extended Modified Lambert-Beer law (EMLB) was introduced by Huong et al. in [20] to address deficiencies in the ability of regression models such as the standard Lambert-Beer law and the Modified Lambert-Beer law, introduced by Twersky [70], to accurately estimate vital parameters including tissue oxygenation (SO_2) and percent blood carboxyhemoglobin (COHb). The EMLB has previously been expressed (e.g., [68], [71], [72]) as:

$$A(\lambda) = G_0 + \mu_a(\lambda)d_0 + G_1\lambda + \lambda e^{-\mu_a(\lambda)d_1} \tag{5.1}$$

In this equation, the second term represents the standard Lambert-Beer law where $\mu_a(\lambda)$ is the wavelength-dependent absorption coefficient of blood and d_0 is the optical path length through the skin. The remaining terms then model artifacts in the absorption spectrum caused by extraneous phenomena. The first term, G_0, provides a constant offset value for the absorbance fit. The combination of these first two terms forms the Modified Lambert Beer law. The third term is used to model both scattering effects and absorbance due to melanin in the epidermis, assuming both remain approximately linear over the spectral region of interest. Finally, the last term is used to model the nonlinear effects that arise from complex light scattering and absorption in the dermis.

To better describe how the EMLB is solved to estimate SO_2 for a given absorbance spectrum, we rewrite the EMLB as:

$$A(\lambda) = \beta_0 G_0 + \beta_1 \mu_a(\lambda)d_0 + \beta_2 G_1\lambda + \beta_3 \lambda e^{-\mu_a(\lambda)d_1} \tag{5.2}$$

Note that the form of the EMLB is modified slightly from its expression in Equation 1 through the inclusion of the β_3 parameter which adds an extra degree of freedom. The solution is then conducted in an iterative two-step manner. In the first step, the Matlab function *fminsearch* is invoked to generate candidate values for the parameters G_0, SO_2, d_0, G_1, and d_1. These values are then passed to the function that *fminsearch* has been tasked to minimize. Within this function, the values for the five parameters are set as constants and a linear regression is performed to estimate the vales for the regression coefficients $\beta_0, \beta_1, \beta_2, \beta_3$. Finally, these regression coefficient values are inserted into Equation 2 and the Euclidian distance between the original spectrum and the EMLB reconstruction is computed and returned to *fminsearch*. This two-step process continues until either the number of *fminsearch* iterations exceeds 10,000 or the return value changes by no more than 1×10^{-20}. Bounds for the SO_2 estimates were set at 0.0 and 1.0 to prevent physically unrealistic estimates.

5.2.2 Monte Carlo Simulation

5.2.2.1 Tools and Datasets

Monte Carlo simulation is a common method for modeling light-skin interactions. Simulated photons are absorbed and/or scattered probabilistically depending on coefficients determined from the skin model provided by the user. Each simulation run typically accounts for a single wavelength, and the results of multiple runs can be combined to generate a full reflectance spectrum.

One of the most popular Monte Carlo simulation tools is the Monte Carlo for multi-layered tissues (MCML) tool developed by Wang and Jacques [73]. MCML has been used extensively in published studies relating to optical measurement of skin parameters. Tsumura et al. [74] provide a good description of how the MCML simulation works. Unfortunately, MCML processing is relatively slow given the large number of computations that occur for each simulation. Addressing this key weakness, CUDAMCML was developed by Alerstam et al. [75] to take advantage of computational acceleration enabled by parallel processing on a graphics processing unit (GPU).

Two separate simulation datasets were developed for this project. The first was used exclusively by the simulated annealing algorithm for wavelength selection (see Section 2.4). It consisted of 36 simulated spectra from 450-800 nm at 1 nm resolution with parameters as given in Table 13. Parameter values were selected to represent typical values for human skin and melanin concentrations light-skinned adults, moderately pigmented adults, and darkly pigmented adults [76]. These parameters are discussed further in Section 2.3.

Table 13. Parameters for simulated dataset used in wavelength selection.

Parameter	Value
SO2	0.40 – 1.0 (steps of 0.05)
Epidermis Thickness (μm)	60.0
Dermis Thickness (cm)	2.0
f_{mel}	0.015, 0.15, 0.40
f_{blood}	0.05

The second simulation dataset was used for validation of the wavelength selection and SO_2 estimation algorithms and consisted of 1,000 spectra, again from 450-800 nm at 1 nm resolution. These spectra were generated using the same parameters as given in Table 1, except the values for SO_2 and f_{mel}were selected at random from a uniform distribution bounded by the maximum and minimum values in Table 13.

5.2.2.2 Simulation of Inexpensive HSI Device

The data simulation approach of CUDAMCML effectively assumes a perfect sensor capable of collecting spectral information at precisely known wavelengths with infinitely narrow bandwidth. This assumption is a poor one for real devices and is particularly poor for a device which relies on inexpensive LEDs and/or filters for spectral data collection. Table 14 gives peak tolerance and spectral widths for example narrowband LEDs in the 520-600 nm range. Thus, to model a more realistic device, the analysis was repeated with a copy of the simulation dataset where the spectra were convolved with a 15 nm FWHM Gaussian filter. Importantly, the absorption coefficients for oxygenated and deoxygenated blood were also convolved with the same filter for this analysis.

Table 14. Example visible band LEDs in the 520–600 nm range of interest. Spectral widths are provided as FWHM.

LED	Peak Wavelength	Peak Tolerance	FWHM
Lumiled LUXEON Z (green) [77]	520-540 nm	± 0.5 nm	30 nm
Thorlabs LED 560L [78]	562 nm	(not given)	11 nm
Thorlabs LED 590L [78]	590 nm	± 10 nm	15 nm
Ocean Insight Visible LED [79]	533 nm	± 5 nm	18 nm
Osram LP-T655-Q1R2-25 [80]	562 nm	± 4 nm	19 nm

Figure 23(a) shows the smoothing effect of the Gaussian convolution on an example spectrum. The convolution tends to flatten and broaden the two peaks which result from oxyhemoglobin absorption. This effect is not modeled in the EMLB, so to compensate, we convolve the extinction coefficients for oxy- and deoxyhemoglobin with the same 15 nm Gaussian filter. Figure 23(b) and Figure 23(c) show these coefficients before and after the convolution. Analyses were conducted on the data both before and after convolution to evaluate the differences in performance that might be expected between a costly medical or industrial grade instrument and the sort of less expensive device that could benefit patients in poor and rural areas. We refer to analyses with the original data (i.e., before convolution) as the “ideal” case and with the convolved data as the “convolved” case.

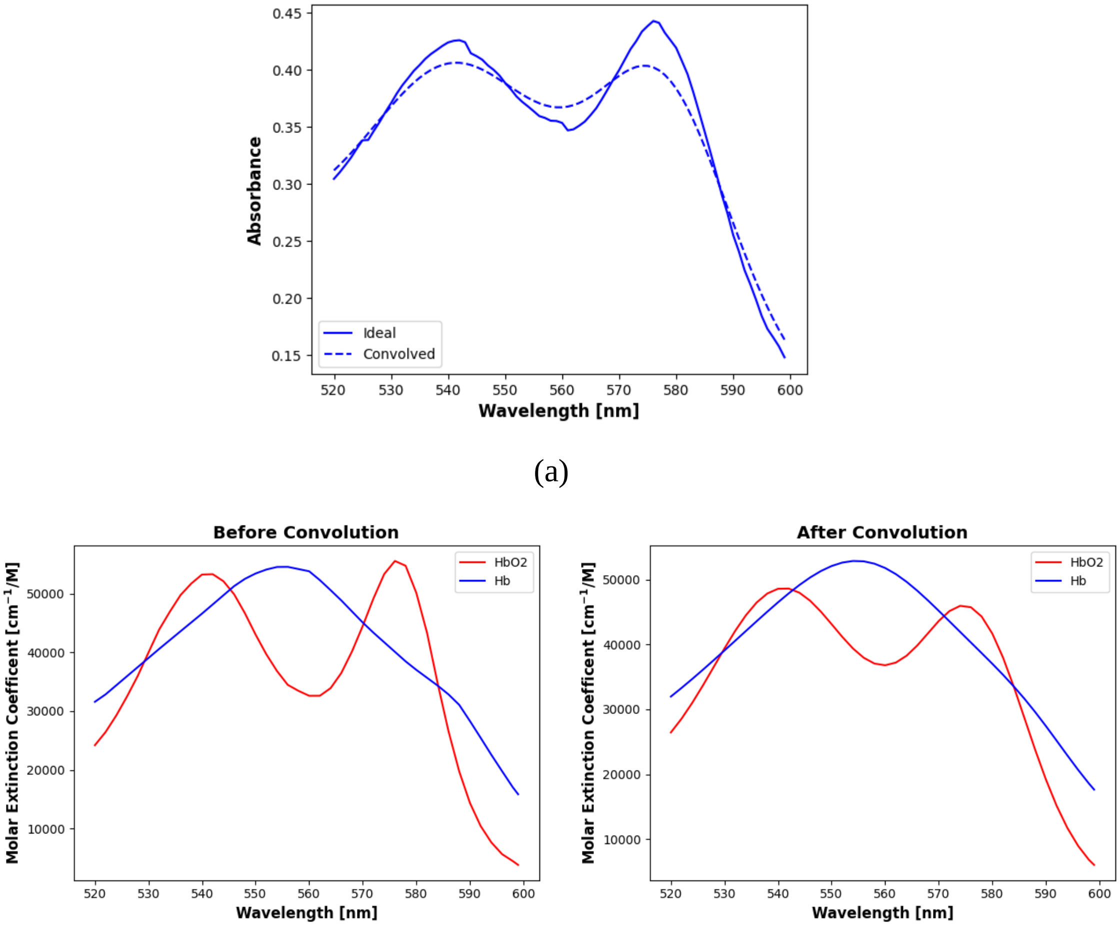

(a)

(b) (c)

Figure 23. Effects of convolution with a 15 nm FWHM Gaussian filter. (a) Example spectrum before and after convolution. The other plots show molar extinction coefficients for oxy- and deoxyhemoglobin (b) before and (c) after convolution. Convolution flattens and broadens the distinctive peaks in the oxyhemoglobin curve, most significantly in the higher wavelength lobe, bringing it closer to the deoxyhemoglobin curve.

5.2.3 Skin Model

Both Monte Carlo datasets were created using a two-layer skin model similar to the one proposed by [23] with an epidermis thickness of 60 μm [76] and a dermis thickness of 2 mm. This model matches the one proposed by Binzoni et al. and is consistent with the approximate maximum penetration depth of visible light in skin [81]. The upper layer is assumed to contain only melanin with volume fraction f_{mel} and the lower layer to contain only blood with volume fraction f_{blood}. Other skin contents (e.g., water and fat) are ignored since their absorption coefficients are orders of magnitude lower than those of melanin and hemoglobin in the 520 – 600 nm range of interest [82].

Absorption coefficients for 100% melanin in the epidermis layer are given by Meglinski and Matcher [83] as:

$$\mu_{a,epi}(\lambda) = 5 \times 10^{10} \lambda^{-3.33}\ (cm^{-1}) \tag{5.3}$$

where the wavelength, λ, is in nanometers. These values are multiplied by f_{mel} to arrive at the actual absorption of light in the epidermis. The value of f_{mel} can range from 1.3 – 6.3% for light-skinned adults, 11 – 16% for moderately pigmented adults, and 18-43% for darkly pigmented adults [76]. Absorption in the dermis is modeled as a combination of absorption by deoxyhemoglobin (Hb) and oxyhemoglobin (HbO2):

$$\mu_{a,dermis}(\lambda) = \varepsilon_{HbO2}(\lambda) C_{HbO2} + \varepsilon_{Hb}(\lambda) C_{Hb} \tag{5.4}$$

where ε_{HbO2} and ε_{Hb} are the absorption coefficients for Hb and HbO2, respectively, given by Prahl [84], and C_{HbO2} and C_{Hb} are the concentrations of these two substances in the blood. This equation can be expressed in a more convenient form that clearly illustrates the role of SO_2 in the absorbance:

$$\mu_{a,dermis}(\lambda) = \Big(\big(\varepsilon_{HbO2}(\lambda) - \varepsilon_{Hb}(\lambda)\big) SO_2 + \varepsilon_{Hb}\Big) T \tag{5.5}$$

where T is the total concentration of hemoglobin in the blood and $SO_2 = C_{HbO2}/T$.

Scattering coefficients, the same used for both the epidermis and the dermis, are provided by Stavaren et al. [85] based on experimentation with intralipid 10%. These values were found to closely match the scattering behavior of biological tissues as found by Bashkatov et al. [86]. Figure 24 shows the absorption and scattering coefficients plotted as functions of wavelength over the visible range. Anisotropy factors, also provided by Staveren et al. [85], are computed as:

$$g(\lambda) = 1.1 - 0.58 \times 10^{-3}\lambda \;\; (cm^{-1}) \tag{5.6}$$

Given the small variation with wavelength over the range of interest, the index of refraction was set to a constant 1.4 for both layers [68], [87].

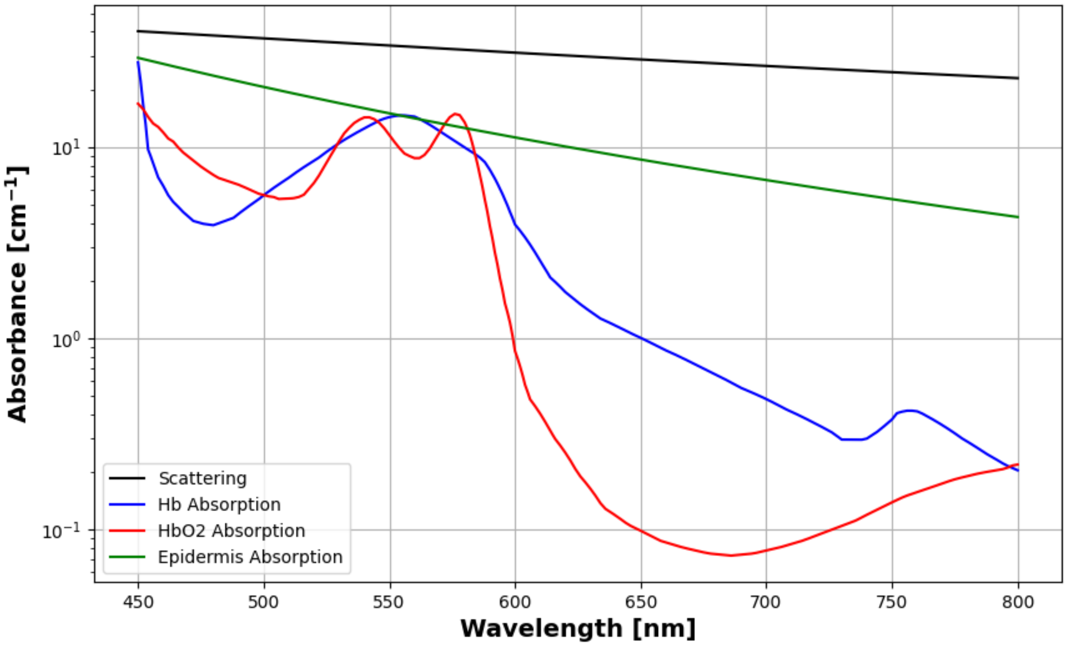

Figure 24. Scattering and absorption coefficients for the skin model used in this study.

5.2.4 Simulated Annealing Wavelength Selection

Instead of sensing the full resolution visible absorbance spectrum at 450 – 800 nm, the proposed method uses just a small number of narrow wavelength bands (referred to simply as “wavelengths” in this paper) that are specifically chosen from the vicinity of the hemoglobin peaks (520-600 nm) to yield accurate SO_2 estimates using the EMLB. Wavelength selection is accomplished via simulated annealing, a heuristic optimization method modeled after the metallurgical annealing process in which the metal undergoes controlled cooling to remove defects and toughen it. The simulated annealing algorithm consists of a discrete-time inhomogeneous Markov chain with current state $s(i)$ and a cooling schedule defined by a starting temperature, T_{max}, a final temperature, $T_{min} < T_{max}$, and a total number of steps, n [63]. The goal of the algorithm is to determine the minimum of a user-defined energy function, $E(i)$.

At each iteration $i \in 1, \cdots, n$, a new trial state is determined by randomly selecting a "neighbor" of the previous state and calculating its energy. If the resulting energy is lower than the energy from the previous iteration, the trial state becomes the new state of the system. If the resulting energy exceeds the energy of the previous energy, the algorithm adopts the trial state with probability given by:

$$P\big(E(i), E(i-1)\big) = e^{-\frac{[E(i)-E(i-1)]}{T(i)}} \tag{5.7}$$

where $T(i)$ is the temperature at iteration i. Note that this equation allows the algorithm to occasionally accept states that result in an increase in energy. This can benefit the optimization by preventing it from becoming stuck in local minima. The probability of accepting such states is high at the beginning of the process when the temperature is high but gradually decreases with decreasing temperature. The output of the algorithm is the state with the lowest energy encountered throughout the annealing schedule. Figure 25 provides a summary of this algorithm.

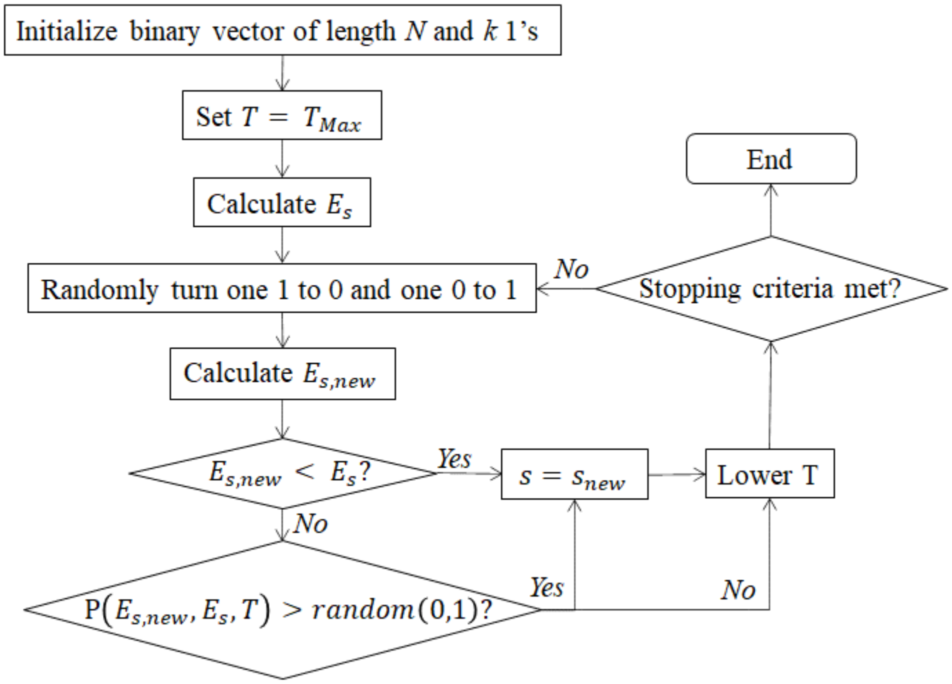

Figure 25. Flowchart for the simulated annealing algorithm used to select the best k wavelengths for SO_2 estimation.

For this wavelength selection problem, the state is defined as an array of binary elements indicating the presence or absence of each wavelength in the full-resolution spectrum. A limit, k, is set on the number of wavelengths selected such that:

$$\sum_{j=m+1}^{N-m-1} I(j) = k \tag{5.8}$$

Under this restriction, the state for each iteration is updated by generating a "neighbor" of the current system state. This is done by randomly de-selecting one wavelength index from the current state and selecting a new one. The energy of the trial state is then calculated as the average absolute prediction error over the Monte Carlo dataset.

The Matlab function *simannealbnd* served as the basis for the implementation of the proposed simulated annealing algorithm. The initial temperature was set to $T_{max} = 5{,}000$ and the maximum number of iterations was set to $n = 1{,}000$. The number of steps was chosen to balance the desire for rapid processing with the need for algorithm convergence. The temperature function was modified to allow for a slower cooling rate than the default and is given by:

$$T = T_{0_{iter}} \cdot 0.985^{(iter-offset)} \tag{5.9}$$

where *iter* is the current number of iterations. With these settings, the probability of acceptance for a 1% increase in the RMSE remained above 66% for the first half the total iterations, allowing for a less restricted random walk through the solution space. In the latter half of the iterations, the acceptance probability was allowed to drop well below 1%, enabling a more targeted search near the optimal point. After 750 iterations, T_0 was increased to 5 and an *offset* was applied to the number of iterations in the exponent of Equation 3 to reset the cooling rate from that point. The acceptance function was modified to implement the exponential function in Equation 1. After every 100 iterations, the state was returned to state with the lowest error found thus far to ensure that the algorithm does a thorough search in the area of the state space which is presumably near the global minimum. The algorithm ended its search upon reaching the maximum number of iterations, or upon reaching 300 consecutive iterations with no change in the average prediction error greater than 1×10^{-10}, whichever came first.

Wavelength selections were conducted for numbers of wavelengths *k* = 3, 5, 7, 11, 15, 20, 40, and 60 (the total number of wavelengths to select from in the 520-600 nm range was 81). To prevent unnecessary selection of adjacent wavelengths for low values of *k*, a validity check was added to the simulated annealing algorithm whereby a candidate selection was declared invalid if the separation between any pair of wavelengths was less than 2 nm and *k* < 20.

5.2.5. Validation Datasets

A two-part validation of the proposed wavelength selection and SO_2 estimation algorithm set was performed. The first part evaluated the algorithms' performance against a Monte Carlo validation dataset that was generated with CUDAMCML using the skin model described in Section 2.3. This simulation dataset, described in Section 2.2, enabled a direct evaluation of SO_2 prediction accuracy since the true SO_2 value was known. Validation was performed both on the full 1 nm resolution simulation data to represent the ideal case described in Section 2.2 and on a version of the same data convolved with a 15 nm FWHM Gaussian filter to represent the convolved case.

The second part of the validation process was performed on the *in vivo* dataset described in [71] which consists of reflectance data collected from 13 Asian volunteers (aged 24.3 ± 2 years). A 9W white light emitting diode (LED) (Lumileds, Philips) illuminated the right index finger of each volunteer from an 80 mm distance at an angle of 20˚ from normal. An optical fiber connected to a spectrometer (Ocean Optics USB4000) was placed 8 mm from the fingertip at 15˚ from normal and collected reflectance data at a spectral resolution of 0.2 nm in the wavelength range of 200-850 nm. These data were then converted from reflectance to absorbance, the 520-600 nm wavelength range was extracted, and the resolution was adjusted to 1 nm via cubic interpolation.

5.2.6 Stability Testing

Additionally, we conducted a series of stability tests where the selected wavelengths were adjusted randomly by ±1 nm to simulate uncertainty in the peak wavelengths. Specifically, for each iteration, a random subset of the *k* selected wavelengths was chosen and each peak wavelength in the subset was moved at random by either +1 nm or -1 nm. The goal of this stability testing was to evaluate the sensitivity of our proposed SO_2 estimation method to uncertainties in the spectral parameters of our hypothesized inexpensive device.

5.3 RESULTS AND DISCUSSION

5.3.1 Wavelength Selection

Wavelength selections for various numbers of selected wavelengths, *k*, for both the ideal case and the convolved case, are shown in Figure 26. Notice that while selections for the ideal case include both lobes of the oxygenated hemoglobin extinction coefficient curve, selections for the convolved case tend to favor the left lobe only. This can be explained by observing the effect that the convolution has on the spectra as shown in Figure 27.

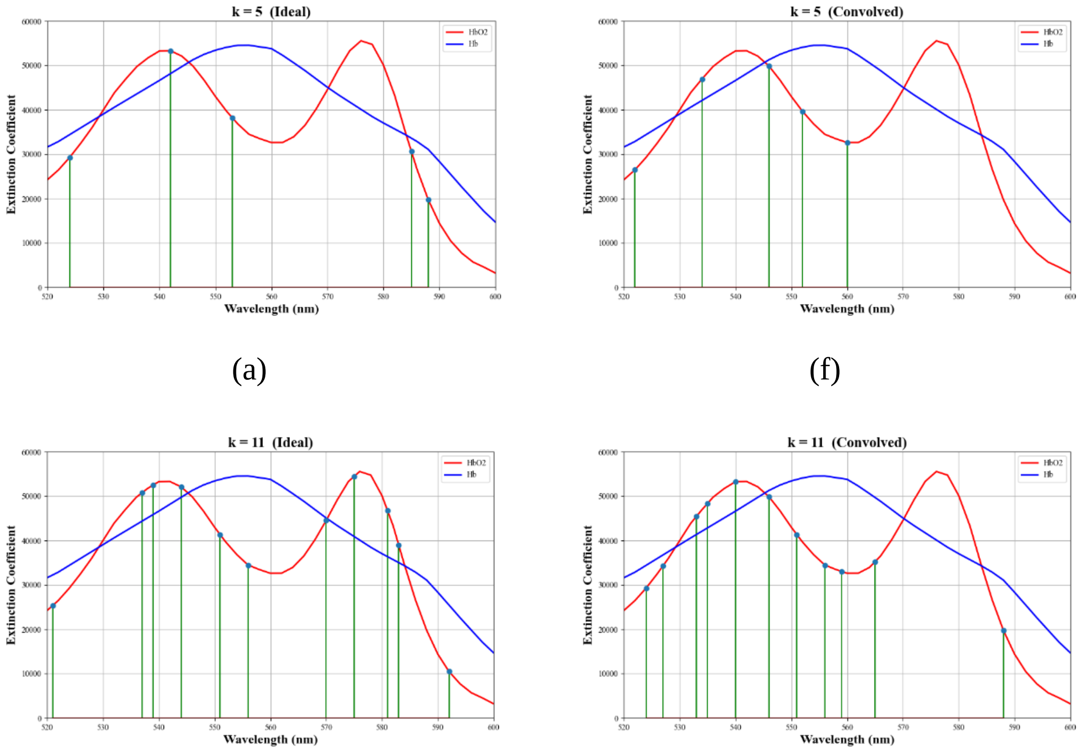

(a)

(f)

(b) (g)

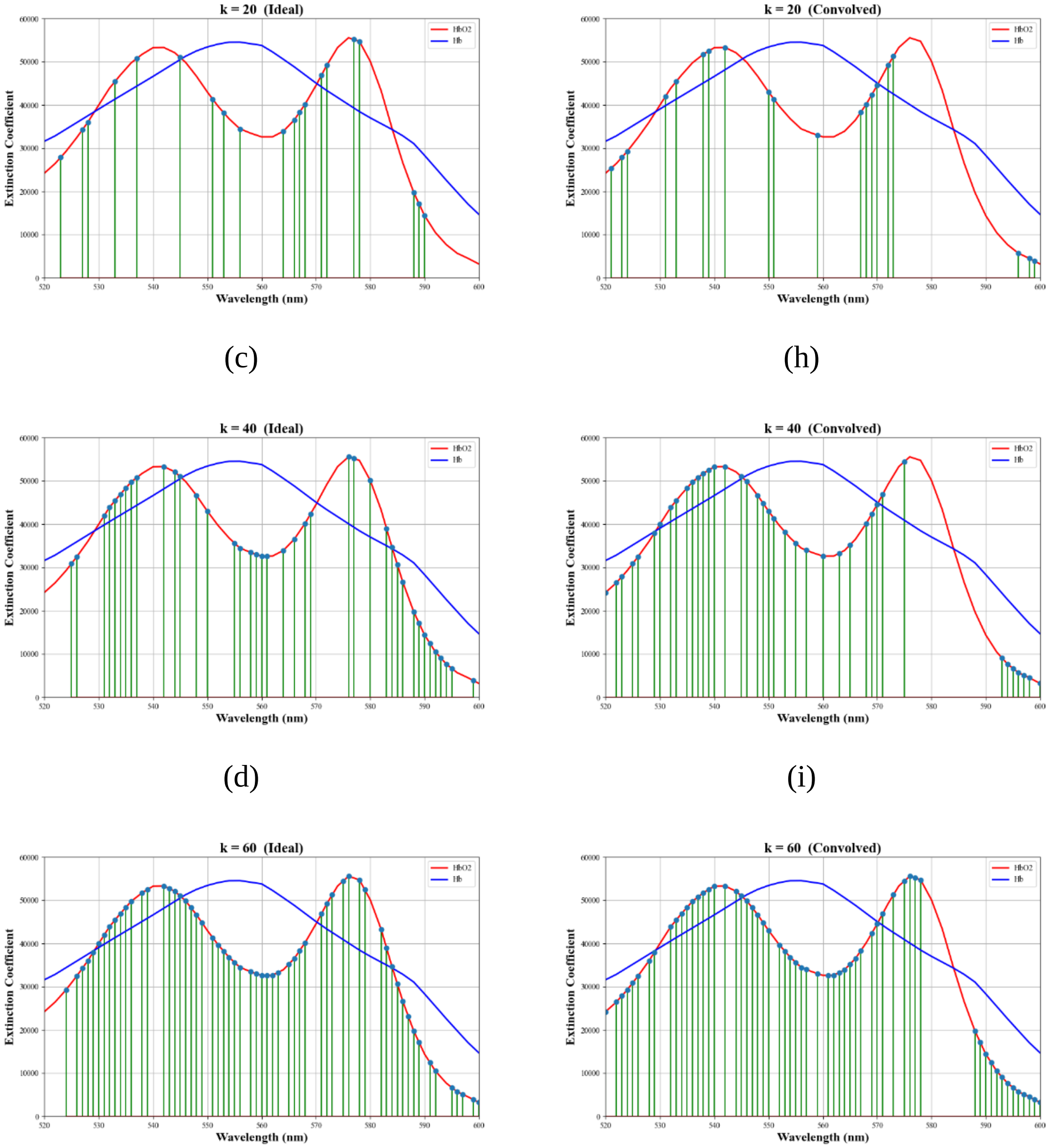

(c) (h)

(d) (i)

(e) (j)

Figure 26. Wavelength selections for various values of k. The left column shows selections for the ideal case and the right column shows selections for the convolved case. (a, f) *k* = 5, (b, g) *k* = 11, (c, h) *k* = 20, (d, i) *k* = 40, (e, j) *k* = 60. The selections are superimposed on plots of the absorption coefficients for oxygenated (red) and deoxygenated (blue) hemoglobin.

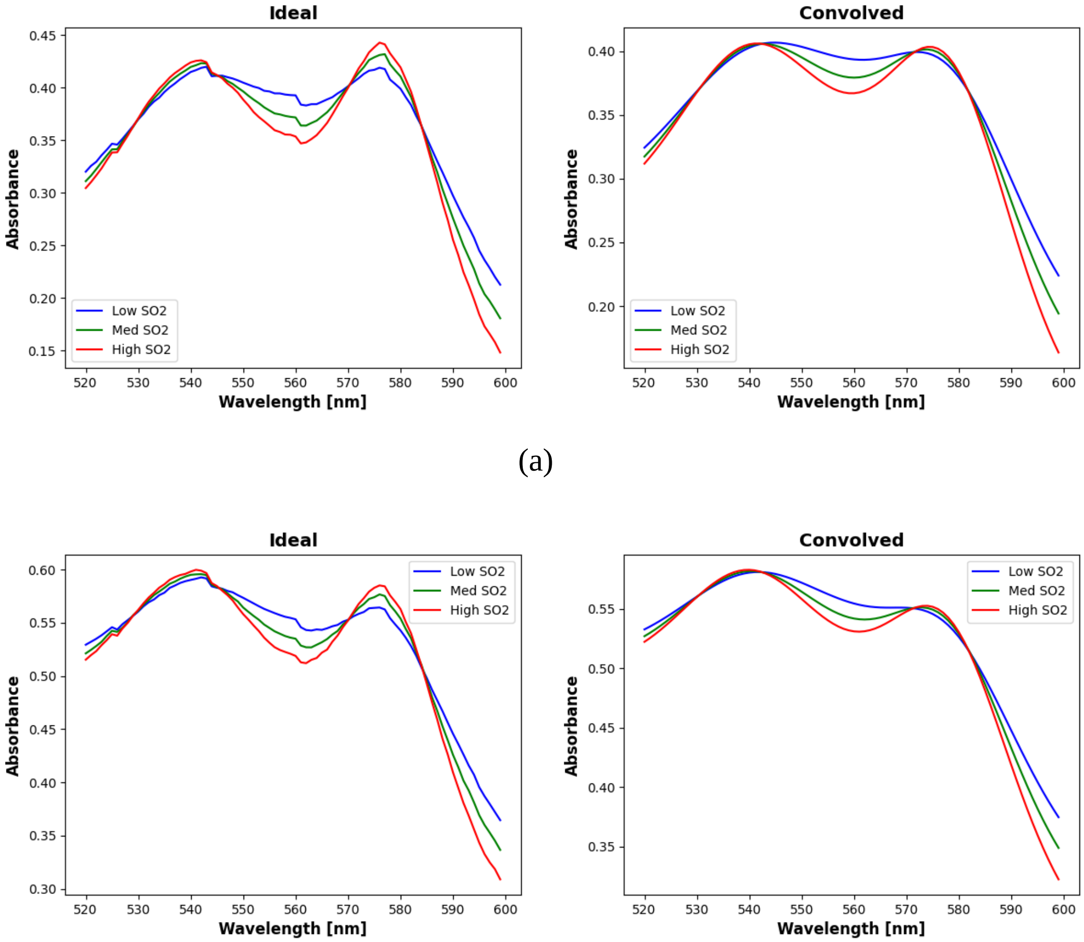

(a)

(b)

Figure 27. Simulated absorption spectra for the ideal (left) and convolved (right) cases for (a, b) low melanin (< 0.10) and (c, d) high melanin (> 0.30) concentrations. Each plot shows example spectra for low (< 0.60, blue), medium (0.60 – 0.80, green), and high (> 0.80, red) SO_2 values. Note that the separations between the curves near the higher wavelength lobe is greatly diminished for the convolved case relative to the ideal case.

Figure 27 shows example simulated spectra for low (< 0.10), medium (0.10 – 0.30), and high (> 0.30) SO_2 values for both the ideal and the convolved cases. The spectra in Figure 27(a) represent skin with low melanin fractions (< 0.10) and those in Figure 27(b) represent skin with high melanin fractions (> 0.30). For both melanin fractions, there is a noticeable separation between the curves near the higher wavelength lobe for the ideal case. However, this separation is greatly diminished for the convolved case. Thus, the ability to distinguish between different SO_2 values using wavelengths in this region is similarly diminished. Interestingly, wavelength selection does favor wavelengths near the lower wavelength lobe even though there is little separation between the curves in any of the plots of Figure 27. Selection of wavelengths in this region is likely needed for slope estimation (third term in Equations 1 and 2) more than for SO_2 estimation (second and fourth terms).

5.3.2 Validation Results

5.3.2.1. Monte Carlo Dataset

Mean prediction errors over the entire Monte Carlo validation dataset for the different numbers of selected wavelengths, k, are plotted in Figure 28 with error bars representing one standard deviation. For both the ideal and the convolved cases, very low errors (< 1%) are evident for all but the $k = 3$ case. Figure 29 shows these results separated by melanin fraction to represent light-skinned, moderately pigmented, and darkly pigmented adults. For all plots in both figures, we note the slight increase in prediction errors for the $k = 81$ case where all possible wavelengths are selected, suggesting that the inclusion of some wavelengths actually hurts the prediction accuracy due to as of yet unmodeled phenomena. This finding is consistent with other studies (e.g., [35]) which achieved higher estimation accuracy with fewer wavelengths than were available. The small highly overlapping error bars for k > 3 indicate that there are no significant differences in prediction errors for the different skin types, thus validating the proposed algorithm’s ability to not only accurately predict SO_2, but to do so for all skin pigmentations.

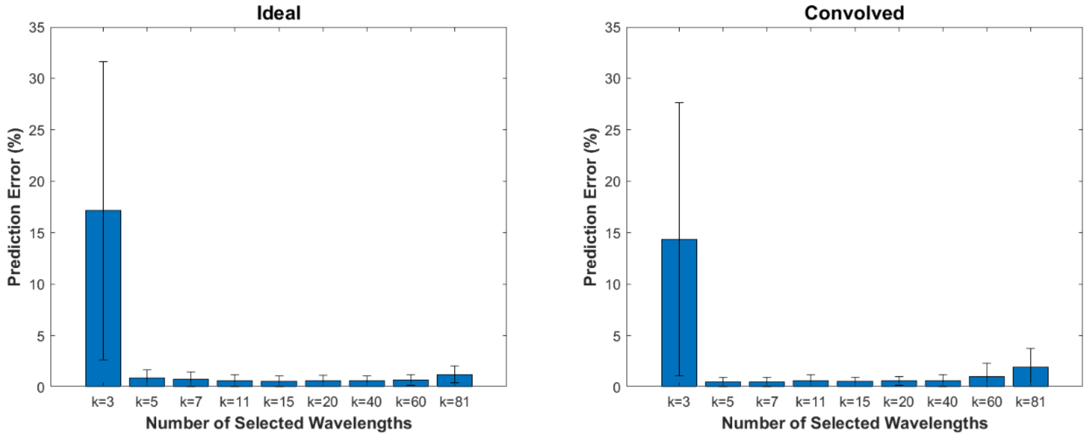

(a) (b)

Figure 28. Mean prediction error values for each number of selected wavelengths along with one standard deviation error bars for the (a) ideal case and the (b) convolved case. Values are computed from the entire Monte Carlo validation dataset.

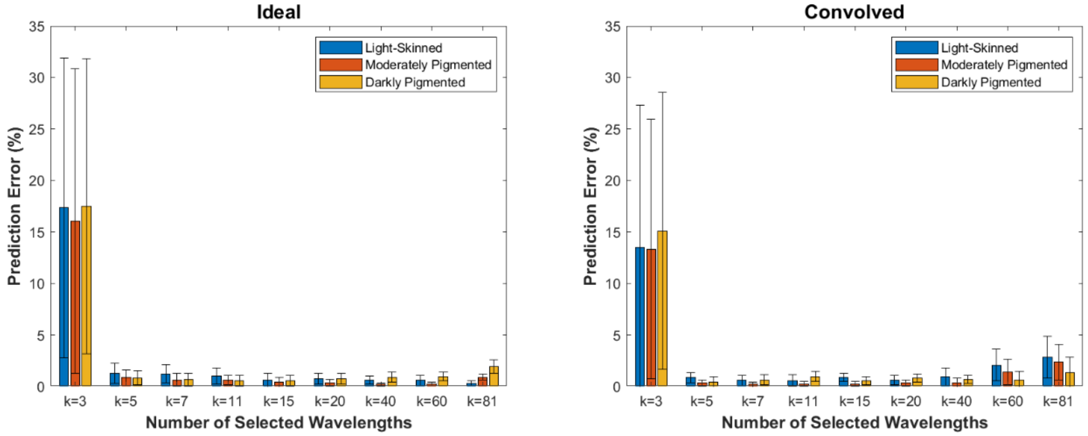

(a) (b)

Figure 29. Prediction errors for the Monte Carlo validation dataset separated by melanin fraction representing light-skinned (< 0.10), moderately pigmented (0.10 – 0.30), and darkly pigmented (> 0.30) adults. Mean values and one standard deviation error bars are given for (a) the ideal case and (b) the convolved case.

5.3.2.2 In Vivo Dataset

Since the true SO_2 values for the *in vivo* dataset are unknown, performance of the proposed algorithm was validated by its ability to yield differences in the SO_2 predictions for the at rest and the occlusion states that are statistically significant. Figure 30 shows the resulting mean predicted SO_2 values and one standard deviation error bars for these two states over all numbers of selected wavelengths. For all but the k = 3 experiment in the ideal case, the separation between mean values for the at rest and occlusion states is statistically significant as determined via a two-tailed independent sample t-test (Matlab's *ttest2* function) with a confidence level of 95%. However, there is noticeable fluctuation in the mean values for $k < 20$.

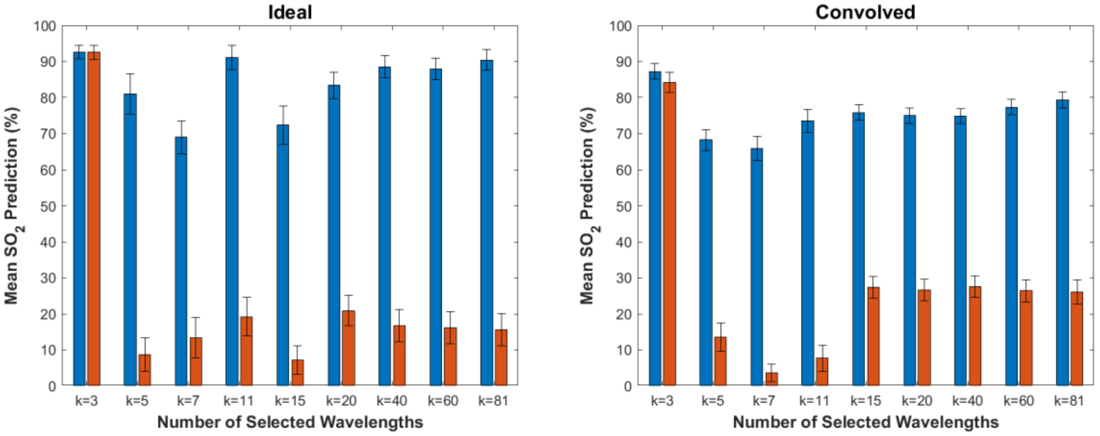

(a) (b)

Figure 30. Mean prediction values and one standard deviation error bars for the in vivo dataset for the different numbers of selected wavelengths. Values for the subjects in the at rest state are shown in blue and for the occlusion state in red. Results are given for the (a) ideal case and for the (b) convolved case.

Table 15 lists the time-averaged and student-averaged SO_2 estimates for the at rest and occlusion states, for both the ideal and the convolved cases, and compares these values with values from the recent literature. The SO_2 estimates from this study are thus consistent with those of other studies for both the at rest and occlusion conditions.

Table 15. Time-averaged and student-averaged mean and standard deviation of SO_2 estimates for the at rest and occlusion conditions in this study (top) compared with values from recent literature (bottom).

	Ideal		**Convolved**	
k	**At Rest**	**Occlusion**	**At Rest**	**Occlusion**
3	92.59 ± 1.94%	92.53 ± 1.96%	87.28 ± 2.17%	84.20 ± 2.82%
5	81.06 ± 5.60%	8.71 ± 4.63%	68.27 ± 2.86%	13.64 ± 3.93%
7	69.03 ± 4.57%	13.37 ± 5.64%	65.86 ± 3.37%	3.64 ± 2.49%
11	91.14 ± 3.34%	19.24 ± 5.36%	73.51 ± 3.15%	7.67 ± 3.66%
15	72.35 ± 5.34%	7.16 ± 3.90%	75.84 ± 2.16%	27.45 ± 3.01%
20	83.41 ± 3.69%	20.90 ± 4.20	74.99 ± 2.16%	26.69 ± 3.01%
40	88.59 ± 3.03%	16.73 ± 4.57%	74.80 ± 2.08%	27.59 ± 2.99%
60	87.98 ± 2.99%	16.17 ± 4.40%	77.37 ± 2.22%	26.36 ± 3.17%
81	90.45 ± 2.83%	15.60 ± 4.44%	79.35 ± 2.30%	26.09 ± 3.29%

	Investigator	Estimated SO_2
At Rest	Caspary et al. [88]	92 ± 2.6%
	Zhang et al. [89]	93 ± 1%
	Kobayashi et al. [90]	68 ± 6%
	Thorn et al. [91]	63 ± 11%
	Huong et al. [71]	91.2 ± 5.4%
	Kyle et al. [92]	73.9 ± 5.8%
	Bezemer et al. [93]	87 ± 3%
Arterial Occlusion	Kobayashi et al. [90]	48%
	Vogel et al. [94]	35%
	Ferrari et al. [95]	20%
	Huong et al. [71]	12.3 ± 8.9%
	Kyle et al. [92]	47.3 ± 7.6%
	Bezemer et al. [93]	3 ± 5%

5.3.3 Stability Test Results

Figure 30 shows the absolute differences in prediction error resulting from the test to determine the stability of the proposed algorithm with respect to small changes in the selected peak wavelengths. The $k > 3$ experiments for ideal case are shown to be very stable to fluctuations in peak wavelengths with most of the error differences much less than 1%. Similar results can be seen for the convolved case, although there is noticeably more variation for the $k = 7$ and $k = 11$ cases with differences in error reaching to ~3%. Furthermore, the mean error differences are shifted away from zero for the $k = 40$ and $k = 60$ cases, reflecting the increases in prediction error from the Monte Carlo validation study results shown in Figure 28. Given the reduction in complexity and expense offered by the hypothetical device enabled by the proposed algorithm, this potential for modest additional error may be an attractive trade off.

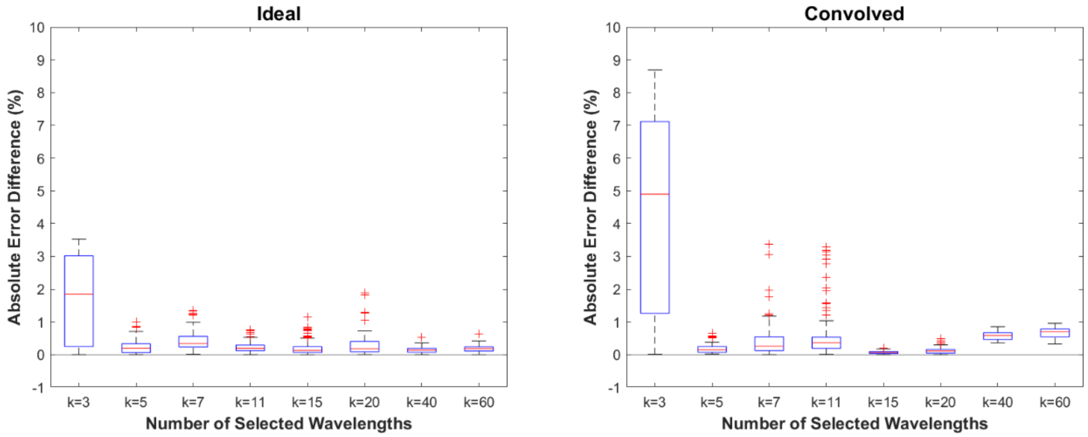

(a) (b)

Figure 31. Results of the stability testing for (a) the ideal case and (b) the convolved case. Boxplots are based on the differences in prediction error between the values for the adjusted wavelength sets and those for the exact wavelengths selected by the simulated annealing algorithm.

5.4 CONCLUSIONS

This study was designed to evaluate the potential for developing an inexpensive device for accurately estimating SO_2, regardless of skin type, via narrowband spectroscopy with a small number of wavelengths. The proposed simulated annealing-based wavelength selection and EMLB-based SO_2 estimation algorithm was found to yield SO_2 estimates with low error (< 1%), using as few as five wavelengths, in both simulated and in vivo validation datasets. Furthermore, these results were consistent across skin types of low, medium, and high melanin fractions. Additional testing proved that the proposed algorithm is robust to slight fluctuations in the peaks of the selected wavelengths as might be experienced in a device constructed with cost-effective LEDs. Similarly, the algorithm proved to be robust to data convolution with a 15 nm FWHM Gaussian filter, another test conducted to model a more realistic device.

CHAPTER 6. RESEARCH SUMMARY AND FUTURE WORK

6.1 SUMMARY AND FINDINGS

The driving goal of this dissertation research was to develop algorithms and methods that could provide the benefits of hyperspectral imaging in a family of inexpensive portable devices, each designed for use in a specific application. This research resulted in the development of multiple algorithms for wavelength selection and classification/regression. Each were designed for the specific application of interest, although common approaches were identified which could be applied across domains. Simulated annealing arose as the preferred wavelength selection method due to its ease of use, its ready adaptability to integer selection problems, and the convenience of transferring to different applications by simply swapping out the cost function. For the fish species classification application, the MLP was identified as the classifier with the best performance.

The key finding of this fish species classification study was that accurate classification could be achieved with just a handful (i.e., ~5-7) of properly selected wavelengths. We showed proof of concept that the complexity and cost of typical hyperspectral imaging devices could be reduced by designing them to collect data at only the required wavelengths. As added benefits, collection at only a handful of wavelengths would significantly reduce data storage requirements and preserve battery life in our desired inexpensive portable devices.

The SO_2 estimation study similarly found that high estimation accuracy was achievable with a small number of selected wavelengths. However, this study further investigated the feasibility of our inexpensive portable device concept through spectral convolutions and peak wavelength adjustments to simulate collection with common LEDs and/or filters. We found that our wavelength selection and EMLB-based SO_2 estimation algorithms were robust to bandwidths of 15 nm FWHM and peak wavelength fluctuations of ±1 nm.

6.2 RECOMMENDATIONS FOR FUTURE WORK

6.2.1 Expansion of Wavelength Range for SO_2 Estimation

In our SO_2 estimation study, we limited our wavelength selection to the 520-600 nm range near the peaks of the hemoglobin extinction coefficients. In future studies, this range should be expanded toward the higher wavelengths, possibly including the near infrared. Not only could this potentially improve SO_2 estimation, but it could also simplify device design if the selected wavelengths were further separated, ensuring less overlap.

6.2.2 Expansion of In Vivo Validation of SO_2 Estimation

The validation of our proposed SO_2 estimation approach relied heavily on analysis with Monte Carlo simulation data, with a relatively small set (13 volunteers) of *in vivo* data used only to show that our algorithms could distinguish between at rest and arterial occlusion conditions. This *in vivo* validation dataset should not only be enlarged, but it should also be diversified to include representatives of all six Fitzpatrick skin types.

6.3.3 Enhanced Simulation of Inexpensive Portable Devices

We convolved our Monte Carlo validation data in our SO_2 estimation study with a 15 nm FWHM Gaussian filter to simulate collection using common LEDs and/or filters. However, true LED bandwidths vary with wavelength. This means that to accurately model the sort of inexpensive portable device that we envision, the bandwidth of the Gaussian filter should vary with wavelength accordingly. Additional enhancements to this model could include peak wavelength adjustments that vary with wavelength as well. In short, the model should be consistent the actual LEDs/filters selected for the hardware design.

6.3.4 Improvements to the Extended Modified Lambert-Beer Law

The EMLB was chosen as our SO_2 estimation model due to its proven record for high estimation accuracy regardless of melanin concentration. However, through the course of our experimentation, we identified certain behaviors in the data that we believe is not modeled in the EMLB. For example, we found that the estimation error for the convolved case increased with an increasing number of selected wavelengths. Furthermore, the EMLB assumes that the effects of scattering and melanin absorption remain linear over the collected wavelength range. This assumption will likely not hold as we explore an expansion of our wavelength range of interest. Thus, additional work will be needed to model phenomena that are not currently comprehended by the EMLB.

6.3.5 Addition of a "None" Class for Fish Fillet Species Classification

Our fish fillet species classification studies found that high classification performance could be achieved with just a few selected wavelengths (and even higher accuracy could be achieved via fusion of spectral modes). However, the approaches proposed in these studies made an implicit assumption that the fillet being examined is of a species that is included in the classifier's list of known classes. If this fillet's species is unknown to the classifier, then the classifier will necessarily fail by declaring the wrong species, possibly with a high associated probability score.

This issue could be resolved by implementing a “none” class in the classifier. The purpose of this new class would be to simply allow the classifier to determine that the fillet under test does not look like any of the known species.

6.3.6 Expansion to New Applications

This dissertation research demonstrated that the proposed wavelength selection algorithms could be adapted to different applications. Thus far we have proven the success of these algorithms for food fraud detection and wound monitoring applications, but range of applicability of these algorithms is in no way limited to these two. Future studies should investigate their use in any of the many additional applications for which hyperspectral imaging has proven useful.

REFERENCES

[1] J.-H. Cheng and D.-W. Sun, “Rapid Quantification Analysis and Visualization of Escherichia coli Loads in Grass Carp Fish Flesh by Hyperspectral Imaging Method,” *Food Bioprocess Technol*, vol. 8, no. 5, pp. 951–959, May 2015, doi: 10.1007/s11947-014-1457-9.

[2] M. S. Kim, A. M. Lefcourt, K. Chao, Y. R. Chen, I. Kim, and D. E. Chan, “MULTISPECTRAL DETECTION OF FECAL CONTAMINATION ON APPLES BASED ON HYPERSPECTRAL IMAGERY: PART I. APPLICATION OF VISIBLE AND NEAR–INFRARED REFLECTANCE IMAGING,” *TRANSACTIONS OF THE ASAE*, vol. 45, p. 11.

[3] Y.-Z. Feng, G. Elmasry, D.-W. Sun, A. G. M. Scannell, D. Walsh, and N. Morcy, “Near-infrared hyperspectral imaging and partial least squares regression for rapid and reagentless determination of Enterobacteriaceae on chicken fillets,” *Food Chem*, vol. 138, no. 2–3, pp. 1829–1836, Jun. 2013, doi: 10.1016/j.foodchem.2012.11.040.

[4] F. Vasefi *et al.*, “Multimode optical imaging for identification of fish fillet substitution and mislabeling (Conference Presentation),” in *Sensing for Agriculture and Food Quality and Safety XI*, May 2019, vol. 11016, p. 1101606. doi: 10.1117/12.2523224.

[5] J. Qin *et al.*, “Detection of fish fillet substitution and mislabeling using multimode hyperspectral imaging techniques,” *Food Control*, vol. 114, p. 107234, Aug. 2020, doi: 10.1016/j.foodcont.2020.107234.

[6] A. F. H. Goetz, “Three decades of hyperspectral remote sensing of the Earth: A personal view,” *Remote Sensing of Environment*, vol. 113, pp. S5–S16, Sep. 2009, doi: 10.1016/j.rse.2007.12.014.

[7] M. Teke, H. S. Deveci, O. Haliloğlu, S. Z. Gürbüz, and U. Sakarya, “A short survey of hyperspectral remote sensing applications in agriculture,” in *2013 6th International Conference on Recent Advances in Space Technologies (RAST)*, Jun. 2013, pp. 171–176. doi: 10.1109/RAST.2013.6581194.

[8] T. Adão *et al.*, “Hyperspectral Imaging: A Review on UAV-Based Sensors, Data Processing and Applications for Agriculture and Forestry,” *Remote Sensing*, vol. 9, no. 11, Art. no. 11, Nov. 2017, doi: 10.3390/rs9111110.

[9] P. Saeedi *et al.*, “Global and regional diabetes prevalence estimates for 2019 and projections for 2030 and 2045: Results from the International Diabetes Federation Diabetes Atlas, 9th edition,” *Diabetes Research and Clinical Practice*, vol. 157, Nov. 2019, doi: 10.1016/j.diabres.2019.107843.

[10] Home *et al.*, “IDF Diabetes Atlas | Tenth Edition.” https://diabetesatlas.org/ (accessed Jun. 18, 2022).

[11] T. I. Oliver and M. Mutluoglu, “Diabetic Foot Ulcer,” in *StatPearls*, Treasure Island (FL): StatPearls Publishing, 2022. Accessed: Jun. 18, 2022. [Online]. Available: http://www.ncbi.nlm.nih.gov/books/NBK537328/

[12] D. G. Armstrong, A. J. M. Boulton, and S. A. Bus, “Diabetic Foot Ulcers and Their Recurrence,” *N Engl J Med*, vol. 376, no. 24, pp. 2367–2375, Jun. 2017, doi: 10.1056/NEJMra1615439.

[13] A. Raghav, Z. A. Khan, R. K. Labala, J. Ahmad, S. Noor, and B. K. Mishra, “Financial burden of diabetic foot ulcers to world: a progressive topic to discuss

always," *Ther Adv Endocrinol Metab*, vol. 9, no. 1, pp. 29–31, Jan. 2018, doi: 10.1177/2042018817744513.

[14] A. Jodheea-Jutton, S. Hindocha, and A. Bhaw-Luximon, "Health economics of diabetic foot ulcer and recent trends to accelerate treatment," *The Foot*, p. 101909, Feb. 2022, doi: 10.1016/j.foot.2022.101909.

[15] "Diabetes and African Americans - The Office of Minority Health," Jul. 18, 2021. https://minorityhealth.hhs.gov/omh/browse.aspx?lvl=4&lvlid=18 (accessed Jul. 18, 2021).

[16] "Prevalence of Diagnosed Diabetes | Diabetes | CDC," Jan. 18, 2022. https://www.cdc.gov/diabetes/data/statistics-report/diagnosed-diabetes.html (accessed Jun. 18, 2022).

[17] P. Tran, L. Tran, and L. Tran, "Impact of rurality on diabetes screening in the US," *BMC Public Health*, vol. 19, no. 1, p. 1190, Sep. 2019, doi: 10.1186/s12889-019-7491-9.

[18] "The Burden of Diabetes in Rural America: Rural Health Research Project." https://www.ruralhealthresearch.org/projects/100002380 (accessed Jun. 18, 2022).

[19] R. Sharma, S. K. Sharma, S. K. Mudgal, P. Jelly, and K. Thakur, "Efficacy of hyperbaric oxygen therapy for diabetic foot ulcer, a systematic review and meta-analysis of controlled clinical trials," *Sci Rep*, vol. 11, no. 1, Art. no. 1, Jan. 2021, doi: 10.1038/s41598-021-81886-1.

[20] M. Dietrich *et al.*, "Hyperspectral imaging for perioperative monitoring of microcirculatory tissue oxygenation and tissue water content in pancreatic surgery — an observational clinical pilot study," *Perioperative Medicine*, vol. 10, no. 1, p. 42, Dec. 2021, doi: 10.1186/s13741-021-00211-6.

[21] I. Oshina and J. Spigulis, "Beer-Lambert law for optical tissue diagnostics: current state of the art and the main limitations," *J Biomed Opt*, vol. 26, no. 10, Oct. 2021, doi: 10.1117/1.JBO.26.10.100901.

[22] S. Vyas, A. Banerjee, and P. Burlina, "Estimating physiological skin parameters from hyperspectral signatures," *J Biomed Opt*, vol. 18, no. 5, p. 57008, May 2013, doi: 10.1117/1.JBO.18.5.057008.

[23] D. Yudovsky and L. Pilon, "Retrieving skin properties from in vivo spectral reflectance measurements," *J Biophotonics*, vol. 4, no. 5, pp. 305–314, May 2011, doi: 10.1002/jbio.201000069.

[24] G. Saiko, P. Lombardi, Y. Au, D. Queen, D. Armstrong, and K. Harding, "Hyperspectral imaging in wound care: A systematic review," *International Wound Journal*, vol. 17, no. 6, pp. 1840–1856, 2020, doi: 10.1111/iwj.13474.

[25] C. J. Lee *et al.*, "Quantitative Results of Perfusion Utilising Hyperspectral Imaging on Non-diabetics and Diabetics: A Pilot Study," *Int Wound J*, vol. 17, no. 6, pp. 1809–1816, Aug. 2020, doi: 10.1111/iwj.13469.

[26] F. Vasefi *et al.*, "Polarization-Sensitive Hyperspectral Imaging in vivo: A Multimode Dermoscope for Skin Analysis," *Sci Rep*, vol. 4, no. 1, p. 4924, May 2014, doi: 10.1038/srep04924.

[27] R. B. Saager, A. Sharif, K. M. Kelly, and A. J. Durkin, "In vivo isolation of the effects of melanin from underlying hemodynamics across skin types using spatial frequency domain spectroscopy," *J Biomed Opt*, vol. 21, no. 5, p. 057001, May 2016, doi: 10.1117/1.JBO.21.5.057001.

[28] N. Gat, “Imaging spectroscopy using tunable filters: a review,” in *Wavelet Applications VII*, Apr. 2000, vol. 4056, pp. 50–64. doi: 10.1117/12.381686.

[29] N. A. Hagen and M. W. Kudenov, “Review of snapshot spectral imaging technologies,” *OE*, vol. 52, no. 9, p. 090901, Sep. 2013, doi: 10.1117/1.OE.52.9.090901.

[30] D. J. Lee and E. A. Shields, “Compressive hyperspectral imaging using total variation minimization,” in *Imaging Spectrometry XXII: Applications, Sensors, and Processing*, Sep. 2018, vol. 10768, p. 1076804. doi: 10.1117/12.2322145.

[31] J. V. Thompson, J. N. Bixler, B. H. Hokr, G. D. Noojin, M. O. Scully, and V. V. Yakovlev, “Single-shot chemical detection and identification with compressed hyperspectral Raman imaging,” *Opt. Lett., OL*, vol. 42, no. 11, pp. 2169–2172, Jun. 2017, doi: 10.1364/OL.42.002169.

[32] Y. Wang, L. Lin, Q. Zhao, T. Yue, D. Meng, and Y. Leung, “Compressive Sensing of Hyperspectral Images via Joint Tensor Tucker Decomposition and Weighted Total Variation Regularization,” *IEEE Geoscience and Remote Sensing Letters*, vol. 14, no. 12, Art. no. 12, Dec. 2017, doi: 10.1109/LGRS.2017.2771212.

[33] D. J. Lee, “Deep neural networks for compressive hyperspectral imaging,” in *Imaging Spectrometry XXIII: Applications, Sensors, and Processing*, Sep. 2019, vol. 11130, p. 1113006. doi: 10.1117/12.2528048.

[34] C. Ferrari, G. Foca, and A. Ulrici, “Handling large datasets of hyperspectral images: Reducing data size without loss of useful information,” *Analytica chimica acta*, vol. 802, pp. 29–39, Nov. 2013, doi: 10.1016/j.aca.2013.10.009.

[35] L. Ayala *et al.*, “Band selection for oxygenation estimation with multispectral/hyperspectral imaging,” *Biomed. Opt. Express, BOE*, vol. 13, no. 3, pp. 1224–1242, Mar. 2022, doi: 10.1364/BOE.441214.

[36] M. Marois, S. L. Jacques, and K. D. Paulsen, “Optimal wavelength selection for optical spectroscopy of hemoglobin and water within a simulated light-scattering tissue,” *JBO*, vol. 23, no. 7, p. 071202, Jan. 2018, doi: 10.1117/1.JBO.23.7.071202.

[37] M. Kim *et al.*, “Line-Scan Hyperspectral Imaging Platform for Agro-Food Safety and Quality Evaluation: System Enhancement and Characterization,” *Transactions of the ASABE*, vol. 54, Mar. 2011, doi: 10.13031/2013.36473.

[38] K. Deep, K. P. Singh, M. L. Kansal, and C. Mohan, “A real coded genetic algorithm for solving integer and mixed integer optimization problems,” *Applied Mathematics and Computation*, vol. 212, no. 2, pp. 505–518, Jun. 2009, doi: 10.1016/j.amc.2009.02.044.

[39] “Mixed Integer ga Optimization - MATLAB & Simulink.” https://www.mathworks.com/help/gads/mixed-integer-optimization.html (accessed Jun. 13, 2020).

[40] M. A. Abramson, “Pattern Search Algorithms for Mixed Variable General Constrained Optimization Problems,” p. 193.

[41] H. Hotelling, “Analysis of a complex of statistical variables into principal components,” *Journal of Educational Psychology*, vol. 24, no. 6, pp. 417–441, 1933, doi: 10.1037/h0071325.

[42] Jing Wang and Chein-I Chang, “Independent component analysis-based dimensionality reduction with applications in hyperspectral image analysis,” *IEEE*

Transactions on Geoscience and Remote Sensing, vol. 44, no. 6, pp. 1586–1600, Jun. 2006, doi: 10.1109/TGRS.2005.863297.

[43] W. Zhang, X. Li, and L. Zhao, “A Fast Hyperspectral Feature Selection Method Based on Band Correlation Analysis,” *IEEE Geoscience and Remote Sensing Letters*, vol. 15, no. 11, pp. 1750–1754, Nov. 2018, doi: 10.1109/LGRS.2018.2853805.

[44] Chein-I Chang and Su Wang, “Constrained band selection for hyperspectral imagery,” *IEEE Transactions on Geoscience and Remote Sensing*, vol. 44, no. 6, pp. 1575–1585, Jun. 2006, doi: 10.1109/TGRS.2006.864389.

[45] B. Guo, S. R. Gunn, R. I. Damper, and J. D. B. Nelson, “Band Selection for Hyperspectral Image Classification Using Mutual Information,” *IEEE Geoscience and Remote Sensing Letters*, vol. 3, no. 4, pp. 522–526, Oct. 2006, doi: 10.1109/LGRS.2006.878240.

[46] Y. Yuan, X. Zheng, and X. Lu, “Discovering Diverse Subset for Unsupervised Hyperspectral Band Selection,” *IEEE Transactions on Image Processing*, vol. 26, no. 1, pp. 51–64, Jan. 2017, doi: 10.1109/TIP.2016.2617462.

[47] M. Zhang, J. Ma, and M. Gong, “Unsupervised Hyperspectral Band Selection by Fuzzy Clustering With Particle Swarm Optimization,” *IEEE Geoscience and Remote Sensing Letters*, vol. 14, no. 5, pp. 773–777, May 2017, doi: 10.1109/LGRS.2017.2681118.

[48] Q. Wang, F. Zhang, and X. Li, “Optimal Clustering Framework for Hyperspectral Band Selection,” *IEEE Transactions on Geoscience and Remote Sensing*, vol. 56, no. 10, pp. 5910–5922, Oct. 2018, doi: 10.1109/TGRS.2018.2828161.

[49] W. Sun, L. Tian, Y. Xu, D. Zhang, and Q. Du, “Fast and Robust Self-Representation Method for Hyperspectral Band Selection,” *IEEE Journal of Selected Topics in Applied Earth Observations and Remote Sensing*, vol. 10, no. 11, pp. 5087–5098, Nov. 2017, doi: 10.1109/JSTARS.2017.2737400.

[50] G. Zhu, Y. Huang, S. Li, J. Tang, and D. Liang, “Hyperspectral Band Selection via Rank Minimization,” *IEEE Geoscience and Remote Sensing Letters*, vol. 14, no. 12, pp. 2320–2324, Dec. 2017, doi: 10.1109/LGRS.2017.2763183.

[51] S. Feng, Y. Itoh, M. Parente, and M. F. Duarte, “Hyperspectral Band Selection From Statistical Wavelet Models,” *IEEE Transactions on Geoscience and Remote Sensing*, vol. 55, no. 4, pp. 2111–2123, Apr. 2017, doi: 10.1109/TGRS.2016.2636850.

[52] Huilin Ye and Hanchang Liu, “A SOM-based method for feature selection,” in *Proceedings of the 9th International Conference on Neural Information Processing, 2002. ICONIP ’02.*, Nov. 2002, vol. 3, pp. 1295–1299 vol.3. doi: 10.1109/ICONIP.2002.1202830.

[53] J. Tian and M. Gu, “Subspace Clustering Based on Self-organizing Map,” in *Proceeding of the 24th International Conference on Industrial Engineering and Engineering Management 2018*, Singapore, 2019, pp. 151–159. doi: 10.1007/978-981-13-3402-3_17.

[54] K. Benabdeslem and M. Lebbah, “Feature Selection for Self-Organizing Map,” in *2007 29th International Conference on Information Technology Interfaces*, Jun. 2007, pp. 45–50. doi: 10.1109/ITI.2007.4283742.

[55] D. K. Jain *et al.*, “An approach for hyperspectral image classification by optimizing SVM using self organizing map,” *Journal of Computational Science*, vol. 25, pp. 252–259, Mar. 2018, doi: 10.1016/j.jocs.2017.07.016.

[56] A. Mohamed, M. S. Hamdi, and S. Tahar, “Self-Organizing Map-Based Feature Visualization and Selection for Defect Depth Estimation in Oil and Gas Pipelines,” in *2015 19th International Conference on Information Visualisation*, Jul. 2015, pp. 235–240. doi: 10.1109/iV.2015.50.

[57] “Cluster with Self-Organizing Map Neural Network - MATLAB & Simulink.” https://www.mathworks.com/help/deeplearning/ug/cluster-with-self-organizing-map-neural-network.html (accessed Jun. 14, 2020).

[58] J. Chauvin *et al.*, “Reconstruction of hyperspectral spectra of fish fillets using multi-wavelength imaging and point spectroscopy,” in *Sensing for Agriculture and Food Quality and Safety XII*, May 2020, vol. 11421, p. 114210I. doi: 10.1117/12.2559230.

[59] T. Kohonen, “Self-organized formation of topologically correct feature maps,” *Biol. Cybern.*, vol. 43, no. 1, pp. 59–69, Jan. 1982, doi: 10.1007/BF00337288.

[60] T. Kohonen, “Essentials of the self-organizing map,” *Neural Networks*, vol. 37, pp. 52–65, Jan. 2013, doi: 10.1016/j.neunet.2012.09.018.

[61] R. A. Fisher, “The Use of Multiple Measurements in Taxonomic Problems,” *Annals of Eugenics*, vol. 7, no. 2, pp. 179–188, 1936, doi: 10.1111/j.1469-1809.1936.tb02137.x.

[62] “Self-Organizing Map - an overview | ScienceDirect Topics.” https://www.sciencedirect.com/topics/veterinary-science-and-veterinary-medicine/self-organizing-map (accessed Jun. 15, 2020).

[63] D. Bertsimas and J. Tsitsiklis, “Simulated Annealing,” *Statistical Science*, vol. 8, no. 1, pp. 10–15, Feb. 1993, doi: 10.1214/ss/1177011077.

[64] M. Perry, *simanneal: Simulated Annealing in Python*. Accessed: May 29, 2021. [Online]. Available: https://github.com/perrygeo/simanneal

[65] N. Srivastava, G. Hinton, A. Krizhevsky, I. Sutskever, and R. Salakhutdinov, “Dropout: A Simple Way to Prevent Neural Networks from Overfitting,” *Journal of Machine Learning Research*, vol. 15, pp. 1929–1958, Jun. 2014.

[66] T. Hastie, R. Tibshirani, and J. Friedman, *The Elements of Statistical Learning: Data Mining, Inference, and Prediction, Second Edition*, 2nd ed. New York: Springer-Verlag, 2009. doi: 10.1007/978-0-387-84858-7.

[67] M. S. Kim, Y. R. Chen, and P. M. Mehl, “Hyperspectral reflectance and fluorescence imaging system for food quality and safety,” 2001, Accessed: Jun. 14, 2020. [Online]. Available: https://pubag.nal.usda.gov/catalog/26654

[68] A. Huong and X. Ngu, “The application of extended Modified Lambert Beer model for measurement of blood carboxyhemoglobin and oxyhemoglobin saturation,” *Journal of Innovative Optical Health Sciences*, vol. 07, May 2014, doi: 10.1142/S1793545814500266.

[69] S. P. Philimon, A. K. C. Huong, and X. T. I. Ngu, “TISSUE OXYGEN LEVEL IN ACUTE AND CHRONIC WOUND: A COMPARISON STUDY,” *Jurnal Teknologi*, vol. 82, no. 4, Art. no. 4, Jun. 2020, doi: 10.11113/jt.v82.14418.

[70] V. Twersky, "Absorption and Multiple Scattering by Biological Suspensions*," *J. Opt. Soc. Am., JOSA*, vol. 60, no. 8, pp. 1084–1093, Aug. 1970, doi: 10.1364/JOSA.60.001084.

[71] A. Huong, S. Philimon, and X. Ngu, "Noninvasive Monitoring of Temporal Variation in Transcutaneous Oxygen Saturation for Clinical Assessment of Skin Microcirculatory Activity," Dec. 2016, pp. 248–251. doi: 10.1007/978-981-10-0266-3_51.

[72] A. Huong, K. G. Tay, and X. Ngu, "Towards Skin Tissue Oxygen Monitoring: An Investigation of Optimal Visible Spectral Range and Minimal Spectral Resolution," *Universal Journal of Electrical and Electronic Engineering*, vol. 6, no. 5B, pp. 49–54, Dec. 2019, doi: 10.13189/ujeee.2019.061607.

[73] L. Wang, S. L. Jacques, and L. Zheng, "MCML—Monte Carlo modeling of light transport in multi-layered tissues," *Computer Methods and Programs in Biomedicine*, vol. 47, no. 2, pp. 131–146, Jul. 1995, doi: 10.1016/0169-2607(95)01640-F.

[74] N. Tsumura, M. Kawabuchi, H. Haneishi, and Y. Miyake, "Mapping Pigmentation in Human Skin by Multi-Visible-Spectral Imaging by Inverse Optical Scattering Technique," *Color and Imaging Conference*, vol. 2000, no. 1, pp. 81–84, Jan. 2000.

[75] E. Alerstam, T. Svensson, and S. Andersson-Engels, "Parallel computing with graphics processing units for high-speed Monte Carlo simulation of photon migration," *JBO*, vol. 13, no. 6, p. 060504, Nov. 2008, doi: 10.1117/1.3041496.

[76] S. L. Jacques, "Skin Optics Summary," Jan. 1998. https://omlc.org/news/jan98/skinoptics.html (accessed Jan. 01, 2022).

[77] "LUXEON Z Color Line," *Lumileds*. https://lumileds.com/products/color-leds/luxeon-z-colors/ (accessed Jun. 23, 2022).

[78] "Unmounted LEDs." https://www.thorlabs.com/newgrouppage9.cfm?objectgroup_id=2814#4475 (accessed Jun. 23, 2022).

[79] "Visible LEDs | Ocean Insight." https://www.oceaninsight.com/products/light-sources/leds/vis-leds/ (accessed Jun. 23, 2022).

[80] "LP T655-Q1R2-25 ams OSRAM | Mouser," *Mouser Electronics*. https://www.mouser.com/ProductDetail/N-A (accessed Jun. 23, 2022).

[81] T. Binzoni, A. Vogel, A. H. Gandjbakhche, and R. Marchesini, "Detection limits of multi-spectral optical imaging under the skin surface," *Phys Med Biol*, vol. 53, no. 3, pp. 617–636, Feb. 2008, doi: 10.1088/0031-9155/53/3/008.

[82] I. V. Meglinski and S. J. Matcher, "Computer simulation of the skin reflectance spectra," *Computer Methods and Programs in Biomedicine*, vol. 70, no. 2, pp. 179–186, Feb. 2003, doi: 10.1016/S0169-2607(02)00099-8.

[83] I. V. Meglinski and S. J. Matcher, "Quantitative assessment of skin layers absorption and skin reflectance spectra simulation in the visible and near-infrared spectral regions," *Physiol Meas*, vol. 23, no. 4, pp. 741–753, Nov. 2002, doi: 10.1088/0967-3334/23/4/312.

[84] S. A. Prahl, "Optical Absorption of Hemoglobin." https://omlc.org/spectra/hemoglobin/ (accessed Jun. 11, 2022).

[85] H. J. van Staveren, C. J. M. Moes, J. van Marie, S. A. Prahl, and M. J. C. van Gemert, "Light scattering in lntralipid-10% in the wavelength range of 400–1100

nm," *Appl. Opt., AO*, vol. 30, no. 31, pp. 4507–4514, Nov. 1991, doi: 10.1364/AO.30.004507.

[86] A. N. Bashkatov, E. A. Genina, V. I. Kochubey, and V. V. Tuchin, "Optical properties of human skin, subcutaneous and mucous tissues in the wavelength range from 400 to 2000\hspace0.167emnm," *J. Phys. D: Appl. Phys.*, vol. 38, no. 15, pp. 2543–2555, Jul. 2005, doi: 10.1088/0022-3727/38/15/004.

[87] I. Nishidate, Y. Aizu, and H. Mishina, "Estimation of melanin and hemoglobin in skin tissue using multiple regression analysis aided by Monte Carlo simulation," *JBO*, vol. 9, no. 4, pp. 700–710, Jul. 2004, doi: 10.1117/1.1756918.

[88] L. Caspary, J. Thum, A. Creutzig, D. W. Lubbers, and K. Alexander, "Quantitative Reflection Spectrophotometry: Spatial and Temporal Variation of Hb Oxygenation in Human Skin," *IJC*, vol. 15, no. 3, pp. 131–136, 1995, doi: 10.1159/000178965.

[89] R. Zhang *et al.*, "Determination of human skin optical properties from spectrophotometric measurements based on optimization by genetic algorithms," *J Biomed Opt*, vol. 10, no. 2, p. 024030, Apr. 2005, doi: 10.1117/1.1891147.

[90] M. Kobayashi, Y. Ito, N. Sakauchi, I. Oda, I. Konishi, and Y. Tsunazawa, "Analysis of nonlinear relation for skin hemoglobin imaging," *Opt. Express, OE*, vol. 9, no. 13, pp. 802–812, Dec. 2001, doi: 10.1364/OE.9.000802.

[91] C. E. Thorn, S. J. Matcher, I. V. Meglinski, and A. C. Shore, "Is mean blood saturation a useful marker of tissue oxygenation?," *Am J Physiol Heart Circ Physiol*, vol. 296, no. 5, pp. H1289-1295, May 2009, doi: 10.1152/ajpheart.01192.2008.

[92] B. Kyle, E. Litton, and K. M. Ho, "Effect of hyperoxia and vascular occlusion on tissue oxygenation measured by near infra-red spectroscopy (InSpectra^{TM}): a volunteer study," *Anaesthesia*, vol. 67, no. 11, pp. 1237–1241, 2012, doi: 10.1111/j.1365-2044.2012.07265.x.

[93] R. Bezemer *et al.*, "Assessment of tissue oxygen saturation during a vascular occlusion test using near-infrared spectroscopy: the role of probe spacing and measurement site studied in healthy volunteers," *Critical Care*, vol. 13, no. 5, p. S4, Nov. 2009, doi: 10.1186/cc8002.

[94] A. Vogel *et al.*, "Using noninvasive multispectral imaging to quantitatively assess tissue vasculature," *J Biomed Opt*, vol. 12, no. 5, p. 051604, 2007, doi: 10.1117/1.2801718.

[95] M. Ferrari, T. Binzoni, and V. Quaresima, "Oxidative metabolism in muscle.," *Philos Trans R Soc Lond B Biol Sci*, vol. 352, no. 1354, pp. 677–683, Jun. 1997.